Scuola Normale Superiore Pisa

Classe di Scienze

Ph.D. Thesis

Incomplete violent relaxation of collisionless stellar systems

Candidate

Michele Trenti

Supervisor

Prof. Giuseppe Bertin

Pisa, Italy - June 2005

Acknowledgments

I am especially grateful to my supervisor Prof. Giuseppe Bertin. I began under his guide my adventure in the field of astrophysics with the study of the gravothermal collapse in globular clusters in Autumn 1999. I kindly remember all the fruitful discussions on the black board in his office. He has always given me valuable comments and suggestions. Many Chapters of this Thesis are also based on scientific papers written together.

A significant portion of this Thesis is related to numerical simulations performed with a code that I developed in collaboration with Prof. Tjeerd van Albada. Without his help and the source codes that he kindly shared with me, the Collisionless Galactic Simulator *would not have seen the light.*

I would also like to thank Prof. Luca Ciotti for a number of discussions and suggestions. We have a project to write a paper together on dynamical friction, which has been most unfortunately always delayed. I hope that we will be able to complete it soon!

My learning curve on numerical simulations of gravitational systems has sharply steepened after the first Modest N-Body School*, that I attended in Strasbourg in Spring 2004. I am very happy to thank the organizers and the teachers at the School, in particular Prof. Douglas Heggie, Prof. Piet Hut and Dr. Peter Teuben.*

A constant, illuminating presence during the preparation of the Thesis has been Daiana. She has lived with me this experience, always being very supportive and open to hearing my doubts and giving words of encouragement.

These years of study for the Ph.D. have been also cheered up by the friends with common passions and interests. In particular I would like to thank Roberta and Edoardo, with the newly born Angelica, Alessandra, Alberto, Ivan, Manuel, Roberto and my fellow adventurers of the D&D group. Thank you also to Guido, Riccardo, Stefano, Federico, Marco and Iacopo.

Finally I would like to thank my family for the continuing love and support during these years.

Contents

Abstract

In this Thesis we study the formation and the evolution of self-gravitating stellar systems by running N-body simulations with a newly developed particle-mesh code and interpreting the results in terms of a family of self-consistent collisionless models, whose dynamical properties are investigated in detail.

We start (Chapter 1) by reviewing the astrophysical framework in which the study of the properties of elliptical galaxies and, more in general, spheroidal collisionless stellar systems is currently approached. We focus on the possibility of a statistical mechanic approach and within this context we introduce (Chapter 2) the family of the $f^{(\nu)}$ models (based on the one-star distribution function $f^{(\nu)} = A \exp\{-aE - dJ^{\nu}/|E|^{3\nu/4}\}$), which play a central role in this Thesis and whose distribution function naturally derives from statistical mechanics considerations. We also show that the $f^{(\nu)}$ family conforms to the paradigm of the gravothermal catastrophe, which is expected to occur (in the presence of adequate energy transport) when the models attain sufficiently high values of central concentration.

In the second part of the Thesis (Chapter 3) we briefly discuss the numerical methods used to simulate self-gravitating N-body systems and we present the structure and performance of a newly developed particle-grid N-body code based on the solution of the Poisson equation with a spherical harmonics expansion. The new code is based on the original code introduced by van Albada (1982) in his pioneering studies of collisionless collapse. We then present (Chapter 4) a first application of the code to revisit the radial orbit instability in collisionless stellar systems, which we argue that could be linked to a negative thermodynamic temperature of the system.

In the third part (Chapter 5) we present in detail the dynamical properties of the $f^{(\nu)}$ models. We compute a number of intrinsic and projected quantities for the models needed to compare them with simulations and observations.

In the fourth part (Chapter 6) we discuss the results from a wide set of numerical simulations of collisionless collapse. The collapse of a stellar system starting from cold initial conditions leads, after a few dynamical times (i.e. $\approx 10^8$ years for a typical elliptical galaxy), to an equilibrium state with a concentrated isotropic core and a low density anisotropic halo that we show to be represented in quantitative detail by the $f^{(\nu)}$ models. The density profile from the simulations is matched over nine orders of magnitude with a relative error of 10%; in addition, the fit to the pressure anisotropy profile is excellent (mean error of 5%) and the models correctly reproduce the phase space distributions in energy and angular momentum ($N(E)$ and $N(E, J^2)$).

This study highlights that the $f^{(\nu)}$ models with $\nu = 1/2$ are a one param-

eter (the density contrast between center and half mass radius) equilibrium sequence, which for stellar systems that have undergone incomplete relaxation by violent collapse plays a role similar to that played by the King models for stellar systems relaxed by collisional effects. To our knowledge, this is the first time that an analytically simple model constructed from first principles under physical arguments is matched in detail, with success, to the results of experiments of galaxy formation performed by N-body simulations.

Chapter 1

Introduction

In spite of the great progress made, many open problems remain in relation to the structure, the formation, and the evolution of elliptical galaxies. Current cosmological scenarios (ΛCDM models) propose a coherent explanation for the formation of structures in the universe, but recent observations of a significant number of old elliptical galaxies in the young universe suggest that a full comprehension of the formation and evolution of elliptical galaxies is still elusive. From this complex cosmological context we thus isolate in this Thesis one important evolutionary mechanism, incomplete violent relaxation, which is known to be the key to explain the quasi universality of the observed surface brightness profiles of elliptical galaxies. We focus on the processes that are associated with collisionless collapse. Our primary objective is to compare the results of simulations of collisionless collapse with a family of theoretical models, justified by a heuristic derivation, based on statistical mechanics. For a proper comparison with cosmological simulations, the framework of analysis presented in this Thesis represent one important step, but should be extended to include two-components models, so as to describe the evolution of a dynamical system in which dark and luminous matter are decoupled from each other.

1.1 Dynamics of elliptical galaxies

Before we address the specific properties of collisionless models and simulations, we briefly recall some basic phenomenology of elliptical galaxies in order to motivate the study of the processes of their formation and evolution.

1.1.1 Universality of the surface brightness profile for elliptical galaxies

Galaxies are complex systems, where many different components, dark matter, stars, gas, globular clusters, and black holes interact with one another, so that, of course, each galaxy when looked at in sufficiently fine detail presents its own individual characteristics. The large scale structure is however remarkably similar for all elliptical galaxies.

Almost a century ago, Hubble (1926) proposed a simple morphological classification for galaxies in terms of their appearance at optical wavelengths. Investigations carried over the period of several decades have then strengthened the conclusion that Hubble's classification *describes a true order among the galaxies* (Sandage & Bedke 1994). In the Hubble morphological classification scheme elliptical galaxies are denoted by the symbol En, with n running from 0 to 7, based on the flattening of the observed image (0 corresponds to a round object while 7 to an aspect ratio 3 : 1 in the plane of sky).

For elliptical galaxies the classification refers to their projected image. Their luminosity profile is generally well represented by the $R^{1/4}$ law (de Vaucouleurs 1948, 1953):

$$I(R) = I_0 \exp\left[-7.67(R/R_e)^{1/4}\right], \tag{1.1}$$

where the factor 7.67 guarantees that half of the total luminosity associated with R_e is contained in the disk of radius R_e, called the *effective radius* of the galaxy. For galaxies characterized by non-circular isophotes R represents the circularized radius R_c, with $R_c = \sqrt{ab}$, where a and b are the major and minor semi-axis of the isophotal ellipse. Probably the best example where such empirical law has been tested is $NGC3379$, an $E1$ galaxy approximately 11 Mpc away from us, where the $R^{1/4}$ law is found to be valid over a range of more than 11 magnitudes, from $R \approx 0.01R_e$ to $R \approx 7R_e$ (de Vaucouleurs & Capaccioli 1979; Capaccioli et al. 1990).

To be sure small systematic deviations from the $R^{1/4}$ are observed, so that a generalization of this empirical law has been proposed (Sersic 1968):

$$I(R) = I_0 \exp\left[-b(m)(R/R_e)^{1/m}\right], \tag{1.2}$$

with m being a free parameter and $b(m) = 2m - 1/3 + 4/(405m) + O(m^{-2})$ (Ciotti & Bertin 1999). Typically the Sersic index m ranges in the interval $2 \lesssim m \lesssim 8$.

Associated with this photometric (weak) homology of elliptical galaxies (e.g., see Bertin et al. 2002), it is natural to expect also a structural homology that goes beyond the mass and light distribution to encompass also

kinematic properties. To address this point a dynamical model should be constructed in terms of a distribution function in the six dimensional phase space. Discussing the properties of a family of self-consistent models suited to describe the photometric and kinematic properties of elliptical galaxies is one of the main objectives of this Thesis.

The apparent *universality* of the observed luminosity profile is a key ingredient to be explained by models of formation and evolution of elliptical galaxies. In particular the model should account for this universality as a result of an evolutionary process, since it appears highly unlikely that the $R^{1/4}$ is just a consequence of fine-tuned initial conditions.

One important physical mechanism acting when collisionless collapse takes place, so that a system quickly reaches a quasi-equilibrium state starting from cold initial conditions, is that of violent relaxation (Lynden-Bell 1967). This mechanism, which will be discussed in Section 1.2.2, can be considered at the basis of the universality of the $R^{1/4}$ law, since it has been shown to be a viable scenario that does not rely on the choice of fine-tuned initial conditions. Simulations of collisionless collapse usually start from initial conditions for which the total kinetic energy is much less than the magnitude of the gravitational energy.

The models that we consider in this Thesis were designed several years ago (Stiavelli & Bertin 1987) so as to keep into account the physics of violent relaxation. In this work we show that these models have projected density profiles consistent with the $R^{1/m}$ that may be used to interpret the weak homology of elliptical galaxies. In addition, the phase space structure is very similar to the one measured in the end products of numerical simulations of collisionless collapse.

1.1.2 Empirical scaling laws

In scenarios where the formation and evolution of galaxies is purely due to gravitational interactions there would be no preferred values for length or mass scales. Therefore other physical processes must act during the formation and the evolution of stellar systems, since we know that specific scaling relations do exist. With respect to this important point the purely dynamical arguments presented in this Thesis have little to say.

For spiral galaxies an important scaling law correlates the total luminosity L with the rotation velocity V:

$$L \propto V^p, \tag{1.3}$$

where p assumes values around 4 and is wave-band dependent (Tully & Fisher 1977).

A similar relation has been proposed for elliptical galaxies (Faber & Jackson 1976):

$$L \propto \sigma^4, \tag{1.4}$$

where σ is the central velocity dispersion measured along the line of sight. At variance with spiral galaxies, where the correlation is tightly established (5% scatter in velocity at a given luminosity), ellipticals exhibit larger scatter from the proposed empirical trend. In fact a better relation, known as the *fundamental plane of elliptical galaxies*, is available, but includes the role of a third scale. This is:

$$R_e \propto \sigma^{1.35} I_e^{-0.84}, \tag{1.5}$$

where R_e is the effective radius in kiloparsec and I_e is the mean surface brightness at the effective radius. The precise values of the exponents in Equation (1.5) depend on the data set and on the details of the fitting method, and are usually quoted with a scatter, associated to the intrinsic thickness of the fundamental plane, of the order of 10% (see Dressler et al. 1987; Djorgovski & Davis 1987).

Interestingly, the discovered scaling laws correlate quantities such as the total luminosity, which depend only on visible matter, with dynamical tracers that are affected by the presence of dark matter. This places strong constraints on the joint formation and evolution of these two galactic components and is often referred to as *the conspiracy problem* (Bertin 2000, Chapter 4).

1.1.3 Dark matter and cosmology

The standard cosmological model represents in a satisfactory way the evolution of the Universe starting from the inflation epoch and is able to predict several properties of the observed microwave background radiation, which contains information on the conditions at the epoch of the decoupling between radiation and matter. Starting from this epoch the matter hierarchically aggregates to form the structures observed as galaxies and stellar clusters at later times, and whose distribution at large scale is successfully explained by the standard cosmological model (for a review of the framework see, e.g. Kolb & Turner 1990; Dodelson 2003).

Within this paradigm several efforts are being made to constrain the set of free parameters on which the model is based. Combined data from Big Bang Nucleosynthesis, large-scale structure surveys, high redshift Supernovae and anisotropy of the cosmic microwave background radiation (CMB) give us a rather consistent convergence toward a model of the Universe which is flat, $\Omega_{tot} \equiv \Omega_M + \Omega_\Lambda = 1$ ($\Omega_{tot} = 1.02 \pm 0.02$) with a matter density

$\Omega_M h^2 = 0.135 \pm 0.01$, where h is the Hubble constant value in units of $100(km/s)/Mpc$, at the 68% confidence level (Spergel et al. 2003; Ruhl et al. 2003); $h \approx 0.71 \pm 0.06$ (Mould et al. 2000; see also Koopmans et al. 2003).

In this picture the baryonic mass, i.e. the luminous matter observed in galaxies and the x-ray emitting gas of the intra-cluster medium, represents only a few percent of the total mass of the Universe. The models presented in this Thesis may thus seem to be aimed at describing only a minority component. Indeed, even without a generalization to two-components, we have proved that they may be effective, in spite of all the limitations, for the interpretation of observations of elliptical galaxies (see Sect. 5.5). In addition, the statistical mechanics arguments from which the models derive may be applied, with little modification, also to an approximate description of the formation of dark halos in the standard cosmological model. Thus our dynamical models could be considered under a different point of view and be used to describe some properties of the dark matter halos (more comments on this point in the concluding discussion, Chapter 7). The origin of the success of one-component models may well be due to a strong link between the properties of dark and luminous matter, as highlighted by the existence of scaling laws such as the Fundamental Plane for elliptical galaxies (see above).

The dynamics of galaxies, and in particular the rotation curves of spiral galaxies, present the most convincing evidence for the presence of halos of dark material. But these dark halos are not significant from the cosmological point of view, unless they extended out to $r_{halo} \approx 2.5h^{-1}Mpc$, a factor 30 greater than what can be estimated with the presently available data. Furthermore, some elliptical galaxies present a velocity dispersion along the line of sight steady declining with the radius, suggesting that dark halos are not always massive (Bertin et al. 1994; Romanowsky et al. 2003).

The bulk of dark matter is argued to be non-baryonic (White et al. 1993) and two major categories of elementary particles have been proposed as candidates to fill this role: *HDM* (Hot Dark Matter) and *CDM* (Cold Dark Matter). The classification depends on whether at the decoupling the matter is still relativistic (*HDM*), or has already cooled down to a non relativistic regime (*CDM*). The term ΛCDM models refers to models relying on the existence of large amounts of Cold Dark Matter with a cosmological constant $\Lambda \neq 0$. Currently the *HDM* scenario seems to be ruled out (Lopez et al. 1999) and the *CDM* scenario is the preferred choice. Candidates for CDM matter are $WIMPs$ (Weakly Interacting Massive Particles), such as the neutralino (Griest 1988). Several efforts are being made to detect experimentally *WIMP* candidates, but at the moment with no success.

Finally, we would also like to mention that a radically new and non-

standard solution to the problem of dark matter on the scales of galaxies has been proposed by arguing that the law of gravity changes at low accelerations, the so called *Modified Newtonian Dynamics* or *MOND* (Milgrom 1983; Sanders & McGaugh 2002; Milgrom & Sanders 2003). So far, this approach proves to be successful in explaining phenomena on the scales of galaxies, although it exhibits some non trivial conceptual difficulties (e.g. in relation to the problem of relaxation, see Ciotti & Binney 2004). Recently a relativistic formulation of *MOND* has been developed (Bekenstein 2004) and applications to cosmological models are being considered (Hao & Akhoury 2005).

1.2 Structure formation in the cosmological scenario

1.2.1 Violent Relaxation

One important mechanism relevant to the formation of elliptical galaxies is that of *violent relaxation* (Lynden-Bell 1967). For large stellar systems (such as galaxies) the star-star relaxation time is many orders of magnitude greater than the actual age of the Universe. Nevertheless, if the potential of a stellar system varies rapidly with time, as is expected during collisionless collapse, the system can experience, over a dynamical time scale, a form of relaxation toward an equilibrium state by means of phenomena that may be related to phase mixing (Lynden-Bell 1967). Such relaxation operates at the level of the coarse-grained distribution function even though the system is collisionless (and thus the evolution of the system in the six dimensional position-velocity phase space $(\vec{x}, \vec{w})$ can be described in terms of the Boltzmann-Liouville equation $Df/Dt = 0$).

Lynden-Bell (1967) notes that, in general, violent relaxation should be incomplete, because the outer parts of stellar systems formed via collisionless collapse have longer dynamical times than those characteristic of the core; the efficiency of mixing becomes insignificant as soon as the central part reaches a quasi-equilibrium state. Indeed, the numerical experiments of van Albada (1982) confirmed the picture that the outer parts of a violently collapsed system is far from thermodynamical equilibrium. In this Thesis we study in quantitative detail the properties of the end products of numerical experiments similar to those carried out by van Albada (1982) (see Chapter 6). Here we recall that qualitatively these properties and concepts are also applicable to dark matter halos in cosmological simulations of structure formation (see below).

1.2.2 Collisionless collapse simulations of galaxy formation

Let us, for a moment, consider a simple framework and suppose that elliptical galaxies are the end product of a short, violent collapse of a cloud of stars initially grouped in cold clumps (i.e. with an initial kinetic energy negligible with respect to the potential energy of the system; see van Albada 1982). The collapse leads to the formation of an isotropic, well relaxed core, embedded in a radially anisotropic, partially relaxed envelope. The process of violent relaxation is indeed found, in numerical simulations, to lead to end-products in which the details of the adopted initial conditions are basically wiped out. Surprisingly, the simulations of van Albada (1982) have shown that the process produces objects that are well fitted by the $R^{1/4}$ law; these results have been confirmed by later studies performed with higher numerical resolution (e.g., Londrillo et al. 1991).

On the other hand, observations tell us that: (1) elliptical galaxies are generally found in clusters rather than in the field, and (2) they are characterized by significant metallicity gradients. The idealized isolated collapse framework explored by the above mentioned simulations of collisionless collapse should thus be put in a more realistic framework. In particular, it is clear that dissipative processes should also contribute, to some extent, to the formation and evolution of elliptical galaxies.

The study of an isolated collapsing system, although lacking important aspects that are relevant to the cosmological scenario, has the advantage of allowing us to clarify some important physical mechanisms involved in the formation process, which would otherwise be confused with a number of other factors and effects present in the cosmological simulations briefly described below.

1.2.3 Ab initio cosmological simulations

Typically a cosmological simulation starts from a primordial spectrum of perturbations in the density of dark matter. The simulation then follows the evolution of the dark matter distribution in a fully relativistic treatment from the redshift of decoupling between radiation and matter ($z \approx 1100$) to $z = 0$. The free parameters in the simulation can be tuned on the basis of the available empirical constraints (such as those provided by measurements of the anisotropy of CMB; see the results of Boomerang, Ruhl et al. 2003, and WMAP, Spergel et al. 2003). The key parameters are Ω_{tot}, the cosmological and Hubble constants and the matter content of the Universe (for a detailed discussion see Jungman et al. 1996, and references therein); but there are

many other parameters that are to be specified.

Smaller portions of some simulations can then be re-simulated at higher resolution. This is obtained by re-sampling the initial perturbations in a desired volume of the simulation and by imposing the boundary conditions at the edges of the re-simulated box according to the results already obtained at lower resolution. In this way, the simulations can probe the scale of clusters of galaxies and even of individual galaxies. However, the structures obtained are those of dark matter halos, and thus are not directly comparable with the observations. In order to compare the results with the observations, the cosmological simulations are often supplemented with some kind of empirical or semi-analytical recipe to include important factors such as the star formation history.

An important result of cosmological simulations is the fact that the obtained dark matter density profiles appear to be consistent with a universal profile (Navarro et al. 1996). The dark matter density profiles in ΛCDM simulations peaks as a power law ($\rho(r) \approx r^n$) in the centre of the halos (the precise value of the exponent is still controversial, with quoted values around $n = -1$; see Ghigna et al. 2000), while in the outer parts the density profile is quoted to decline as approximatively r^{-3}. Navarro et al. (1996) proposed the following simple law to describe this density profile:

$$\rho(r) = \frac{\rho_s}{r/r_s(1 + r/r_s)^2}, \tag{1.6}$$

where ρ_s and r_s are scales for density and radius, respectively.

A simple universal description seems thus to be viable both for the surface brightness profile of elliptical galaxies (the $R^{1/4}$ law) as well as for the dark matter halos density (the *NFW* profile, Eq. 1.6). However, these descriptions do not carry information on why universal profiles exist and on why they assume these particular expressions. In the Thesis we try to answer these questions for the case of elliptical galaxies. In addition, we note that our models (derived from first principles) also present a universal density profile which is not too different from the *NFW* formula (see Sect. 5.3.1 and Chapter 7). This similarity is indeed very promising and further investigations are planned.

1.2.4 Cosmological simulations and the large scale structure of the Universe

ΛCDM cosmological simulations, starting from the concordance cosmology framework with the parameters discussed in Section 1.1.3, reproduce the statistical properties of the large scale structure of the Universe as observed in

a number of important galaxy redshift surveys (e.g., the *2dF Galaxy Redshift Survey*, Percival et al. 2001, and the *SDSS, Sloan Digital Sky Survey*, Schneider et al. 2003). In these surveys the positions and the distances of hundred thousands (*2dF*) or millions of galaxies (*SDSS*) are measured in order to construct a three dimensional map of portions of the nearby universe. From these maps the power spectrum of the observed density perturbations can be calculated and compared with the theoretical expectations from numerical simulations of structure formation. The level of agreement is excellent (Percival et al. 2001), although we recall that in general a survey measures the distribution of baryonic luminous matter, while the numerical simulations are dominated by dark matter particles. The explicit assumption that the luminous particles can be used to trace the underlying distribution of mass is thus required.

To be sure, the comparison of ΛCDM simulations with the observations still presents some puzzling points. A better fit to the rotation curves of dwarf spiral galaxies is given by dark matter profiles shallower than those predicted by ΛCDM (e.g., see Simon et al. 2003). In addition Binney & Evans (2001) show that microlensing and rotation curve data for our galaxy also rule out a cuspy dark matter profile. The solution may lie in the existence of an effective evolutionary mechanism that disrupts cuspy profiles. From the dynamical point of view one very interesting possibility is associated with the dynamical friction effects that small satellites induce on the central density profile of a galaxy or dark matter halo (Bertin & Trenti 2003; Ma & Boylan-Kolchin 2004). The topic of small satellites brings us naturally to one other fundamental problem of cosmological simulations, i.e., the *missing satellites* problem. For the local group ΛCDM predicts a number of subhalos that is approximately two orders of magnitude greater than the total number of satellite galaxies observed (Klypin et al. 1999). No convincing solutions to this problem have been presented so far (for an overview of the solutions proposed see e.g., Kazantzidis et al. 2004).

This gives us additional reasons to concentrate the efforts of the Thesis on understanding first the simplified one-component framework of galaxy formation via collisionless collapse, where the physical process that are in act can be kept under better control.

1.2.5 Evolution with redshift of elliptical galaxies

Massive spheroidal galaxies ($M \gtrsim 10^{11} M_{\odot}$) hosts more than half of the stars in the local universe. In the ΛCDM framework these galaxies are formed as the final products of the hierarchical merging processes and thus should have appeared in significant numbers only recently. However recent high redshift

observations (Treu et al. 1998, 2005; Cimatti et al. 2004) have highlighted the discovery of a significant number of massive spheroids at redshift $z \gtrsim 1.5$, where the universe had only one quarter of its present age. From the sample of galaxies observed in the K20 survey (Fontana et al. 2004) this would imply that old galaxies at redshift $z > 1.5$ account for approximately 20% of the whole galaxy population, a ratio that constitutes a challenge to the current cosmological framework (Cimatti et al. 2004). In addition, the data from Treu et al. (2005) show evidence that less massive spheroidal galaxies have also younger stellar ages in contradiction with the expectations from the hierarchical assembly models for galaxies. The recent availability of data at even higher redshift, such as those from the Hubble Ultra Deep Field project, will allow us to probe the formation of structures out to $z \approx 6$ (Bunker et al. 2004; Stiavelli et al. 2004). The data probe in fact the tail of the re-ionization epoch and the star formation history of the Universe by detecting the faint end of the galaxy luminosity function, and tracking the origin, structure, and merger history of galaxies.

Treu et al. (2005) suggest that the observations could be reconciled with the paradigm of hierarchical merging by introducing a more detailed treatment of the physics that regulates the star formation in a collapsing system. In the simplified model for collisionless collapse that we consider in our Thesis star formation is assumed to happen mainly before the collapse and the process of formation of spheroids is imagined to take a few hundreds million years, independently of the redshift.

1.3 Statistical mechanics of self-gravitating systems

1.3.1 Statistical mechanics of violent relaxation

Predicting the final equilibrium state of a system undergoing collisionless collapse is a basic problem still open. Progress in this direction will help us to understand the origin of the universality of the surface brightness of elliptical galaxies; hopefully, it may also give us clues to the origin of the cusps of dark matter halos found in cosmological simulations and the reasons behind their universal shape.

To select physically motivated distribution functions among the infinite variety, which is in principle available for the description of collisionless stellar systems, one may try to resort to statistical mechanics arguments. A first attempt in this direction was carried out by Lynden-Bell (1967), who proposed a statistical theory to construct the distribution function of a collisionless

system that experiences violent fluctuations of the gravitational potential before reaching equilibrium. The system relaxes in a collisionless way and settles down in a quasi-equilibrium configuration on a dynamical time-scale. No mass segregation should result from the process of violent collapse, since the chaotic changes of the collective gravitational fields involve masses that are much greater than any individual stellar mass. Thus the properties of the equilibrium distribution function are expected to be independent of the stellar masses.

Lynden-Bell's theory is based on the continuum limit (i.e. $N \to \infty$) for a system of N stars and leads to curious findings, in particular the existence of an exclusion principle of dynamical origin, so that the distribution function for a violent relaxed system formally resembles the Fermi-Dirac distribution, even though the particles are distinguishable. In the limit relevant to realistic stellar systems, the distribution becomes a Maxwell-Boltzmann distribution, but with stars of different masses sharing a common velocity dispersion ($f \propto \exp\{-\beta E\}$, with $E = w^2/2 + \Phi(r)$ being the single particle energy per unit mass). At a fundamental level the theory encounters theoretical obstacles, one of them being related to mass segragation (the "velocity dispersion problem", see Lynden-Bell 1967 Appendix I; see also Nakamura 2000).

A different approach to the problem is to recognize that for a better description of galaxies the finite number of stars that populate the phase space plays an important role, so that the theoretical problems in the Lynden-Bell formulation may be related to the continuum limit (Shu 1978, 1987). The analysis based on such discrete approach highlights that the degeneration resulting from the dynamical exclusion principle may be of little physical interest, since it would be important only when two-body encounters becomes no longer negligible, breaking the collisionless assumption. Shu (1978) argued that mass segregation can be avoided if initial conditions are well mixed, since the collisionless evolution of the system conserves the mass composition of the macrocells in which the system can be divided.

An alternative formulation of violent relaxation has been derived in the framework of information theory (Nakamura 2000). In this context, a common velocity dispersion distribution function is naturally obtained, so that no mass segregation is expected. This is done by assuming a discretization of the phase space in terms of equal mass elements rather than in terms of equal volume hypercubes, as considered by Lynden-Bell.

Different numerical experiments have been proposed to test the theory of violent relaxation, starting from the one dimensional simulations by Cuperman et al. (1971) until the recent simulations by Merrall & Henriksen (2003) and by Arad & Johansson (2005). In the latter study the authors try, in

particular, to measure the phase space density reached in the central regions of a clumpy system (made of four cold clumps arranged in a symmetric tetrahedron) that has undergone violent relaxation. The equilibrium phase-space density is compared with the expectations both from the Lynden-Bell (1967) and Nakamura (2000) theory and it is claimed that both formulations do not provide a good description for the measured phase space structure, so that it seems that both theories are "fundamentally wrong" (Arad & Johansson 2005).

This may reflect that effectively violent relaxation is still lacking important theoretical arguments. This would not be surprising, since it is known that the application of statistical mechanics to self-gravitating systems presents subtle points. In fact, at the fundamental level of the definition of the entropy it is not clear whether the concept is compatible with gravity due to the fact that the long range nature of gravitational interaction leads to a lack of additivity for self-gravitating systems (e.g., see Tremaine et al. 1986; Stiavelli & Bertin 1987). Thus recent investigations have explored the possibility of setting the discussion in the context of non-standard non-extensive entropies (e.g., the Tsallis entropies; see the study of the gravothermal properties of polytropic spheres by Chavanis 2002 and Taruya & Sakagami 2002).

The solution to the discrepancy between theory and experiments may however lie also in the well known incompleteness of the relaxation process (e.g., see Lynden-Bell 1967). Since the fluctuations in the gravitational potential are rapidly damped as the system proceeds to the new equilibrium state, this will not necessarily be the most probable state. A strong evidence to support this argument is given by the well known result that violent relaxation is in reality complete only at the centre of the system, where the dynamical time-scale is shorter, while the outer parts, that are "still collapsing" when the potential stops fluctuating, are frozen in a quasi equilibrium configuration characterised by the predominance of radial orbits. This important point will be discussed below. The introduction of empirical constraints to describe the incompleteness of violent relaxation will lead to the construction of the $f^{(\nu)}$ models (Stiavelli & Bertin 1987).

In this Thesis we do not address the fundamental issues on the statistical mechanics of self-gravitating systems mentioned above. We rather take a more empirical approach and demonstrate that, in the context of incomplete violent relaxation, the $f^{(\nu)}$ models, constructed on the basis of statistical mechanics arguments, *a posteriori* describe accurately the properties of both observed elliptical galaxies and N-body experiments of violent collapse. The success of the $f^{(\nu)}$ models thus makes questions on the precise validity of the arguments assumed during their construction less relevant.

1.3.2 Self-consistent models for incomplete violent relaxation

The arguments given above highlight the need for an effective statistical mechanics theory that takes into account the incompleteness of violent relaxation. In this respect, the idea of applying empirical additional constraints during the entropy extremization leads to interesting results for the construction of distribution functions suited to describe the end products of violently relaxed systems (Stiavelli & Bertin 1987). The authors pursued two different routes: one is based on the assumption that a third quantity Q is conserved during incomplete violent relaxation in addition to the total mass and energy of the system. This route leads to the $f^{(\nu)}$ models, that at the time of the discovery were left aside and not studied in detail until the present Thesis work. The ideas behind the conservation of this third quantity are discussed in the next Chapter. Here we briefly focus instead on the alternative route proposed by Stiavelli & Bertin (1987), which leads to the f_∞ family (Bertin & Stiavelli 1984).

Stiavelli & Bertin (1987) started with the idea that the partition of phase space to be used is the one specified by the single particle energy E and angular momentum J^2, which they show to be equivalent to the use of a non uniform a priori probability in the ordinary position-velocity $(\vec{x}, \vec{w})$ phase space partition. This probability distribution is shown to be proportional to the frequency $1/T_r$ of radial orbits with given energy and angular momentum. In addition, the authors impose the detailed conservation of the angular momentum distribution $N(J^2)$ for those particles that are in regions where violent relaxation is expected to be less effective because the collapse time is shorter than the local dynamical time. With this assumption, and considering $T_r(E, J^2) \approx |E|^{-3/2}$ at large radii (where the potential is almost Keplerian), the f_∞ distribution function is recovered:

$$f_\infty(E, J^2) = A(-E)^{3/2} \exp\{-aE - cJ^2/2\}. \tag{1.7}$$

Interestingly, the factor $\exp\{-cJ^2/2\}$, obtained by Stiavelli & Bertin (1987) as a consequence of the detailed conservation of the angular momentum at large radii, was introduced by Lynden-Bell (1967) as an attempt to model the incompleteness of violent relaxation. The factor $|E|^{3/2}$ derives instead from the assumed uniform partition in the (E, J^2) phase space.

The f_∞ models have been successfully applied to the description of observed elliptical galaxies, also extended to a two component formulation (Bertin et al. 1992) to allow for the presence of a dark matter halo. Yet, when compared in detail to the end-products of typical simulations of violent collapse, these models are not fully satisfactory because they are too

isotropic. Thus the idea of comparing in quantitative detail the end-products of numerical simulations of collisionless collapse with a family of theoretical models was left aside.

In this Thesis, noting that the $f^{(\nu)}$ models appear more promising as a tool to interpret the results of collisionless collapse, we thus explore a detailed comparison up to the phase space level between the $f^{(\nu)}$ models and numerical simulations of collisionless collapse that we have run with a newly developed particle-grid code. We show that the $f^{(\nu)}$ models with $\nu = 1/2$ are able to provide a realistic description of the properties of observed elliptical galaxies (see Chapter 5) as well as of the end-products of collisionless collapse (see Chapter 6). The $f^{(1/2)}$ models can thus be considered *the* distribution function that describes the final equilibrium state of incomplete violent relaxation, much like the King models describe the end-products of collisionally relaxed truncated stellar systems.

Chapter 2

Thermodynamic description of partially relaxed stellar systems

In this Chapter we introduce the distribution function of the $f^{(\nu)}$ models, derived earlier (Stiavelli & Bertin 1987) from statistical mechanics considerations and well suited to describe partially relaxed stellar systems. Here we focus on the thermodynamic properties of these models, while the detailed study of their dynamical properties and the comparison with the products of numerical simulations of collisionless collapse will be discussed in Chapters 5 and 6. This Chapter is mainly based on the results published in Bertin & Trenti (2003) Ap.J. 584, 729.

2.1 The gravothermal catastrophe framework

The possibility of providing a thermodynamical description of self-gravitating stellar systems[1] has motivated a number of investigations in galactic dynamics, starting with the pioneering work of Antonov and Lynden-Bell in the 60s. After the realization that violent relaxation is likely to lead to partially relaxed configurations in dynamical equilibrium (Lynden-Bell 1967), a re-examination of the problem of the isothermal sphere, studied earlier by Bonnor (1956) for a self-gravitating gas, led to the interesting possibility that stellar systems may undergo the process of gravothermal catastrophe (Lynden-Bell & Wood 1968; see also Antonov 1962).

A self gravitating system may develop an instability due to its negative heat capacity. In fact, if a gravitational system loses energy, the net effect is that, due to the virial theorem, the kinetic energy grows, while the system

[1] In this Thesis the words "stellar system" are meant to indicate a group of N point particles interacting gravitationally.

shrinks to find a new equilibrium state with a more negative potential energy. This is reminiscent of the behavior of a satellite orbit slowly decaying due to friction into the Earth atmosphere: the satellite dissipates energy but gains speed as the orbit becomes lower. Thus, if we define the temperature of the stellar system as proportional to the kinetic energy, we end up, after losing heat, in a more compact configuration with a higher temperature.

If we now imagine a self-gravitating system embedded in a colder thermal bath and we assume the existence of an adequate heat transport mechanism between the bath and the system, the latter will lose energy and become progressively hotter and more compact.

Within a single N-body system, this picture is still valid if the central region is so concentrated that its dynamical equilibrium is close to that of an isolated system. In this case the external region serves as a heat sink for the core. The core can thus be in the condition of losing energy, heating the halo, as well as itself, and contracting during the process. This picture plays an important role for the evolution of globular clusters, where the heat diffusion is provided by two-body encounters (e.g. see Spitzer 1987, see also our discussion in Sect. 2.2 for possible applications to elliptical galaxies, where two-body relaxation is ineffective in providing heat diffusion).

2.1.1 Gravothermal collapse for truncated isothermal spheres

To quantify this peculiar property of gravitational systems, Lynden-Bell & Wood (1968) proposed a simple model based on a self-gravitating gas embedded in a perfectly reflecting and non-conducting sphere. The equilibrium distribution function $f(E)$ of the gas was obtained extremizing the Boltzmann entropy $S = -\int f \log f$ and imposing the conservation of the total mass and total energy. The result is a one parameter family of truncated isothermal spheres (with $f(E) = A \exp\{-\beta E\}$) with different degrees of central concentration.

By construction, all these configurations are characterized by the fact that a first order adiabadic displacement of the gas elements induces no changes on the value of the entropy S. To evaluate the stability of a specific configuration it is in principle necessary to compute the variation of S up to second order. However, the stability of equilibrium configurations can be often studied without resorting to a full computation of the variation of entropy up to second order, but rather by studying the properties of the series of equilibrium. This has been done by Lynden-Bell & Wood (1968) with the method of the linear series of equilibria (see next Section). If the ratio between the

central density and the density at the edge of the reflecting sphere is above a critical level ($\rho_0/\rho_{edge} \approx 709$) the system undergoes a gravothermal collapse, experiencing a run-away from the equilibrium sequence over a time scale set by the rate of the heat flow.

2.1.2 The study of the stability: the gravothermal spiral

Following Katz (1978), let us consider a system described by n state variables x_i and let S be a function of the x_i variables and of one real parameter ξ. The system is in equilibrium for configurations that extremize S, i.e. must hold:

$$\partial_i S = 0, \tag{2.1}$$

for every i.

An equilibrium configuration is stable if the value of S is a local maximum, i.e. if for every small displacements δx_i and δx_j we have:

$$\partial_{ij} S \delta x_i \delta x_j < 0. \tag{2.2}$$

With respect to the parameter ξ, the state variables at equilibrium can be written as:

$$x_i = X_i^{(a)}(\xi), \tag{2.3}$$

with a ranging over the multiplicity of solutions of Equation (2.1). With this parametrization we define N series of equilibrium in the $n+2$ dimensional space (S, ξ, x_i), with N equal to the number of solutions of Equation (2.1). The points of intersections (bifurcations) of these series are the only points where a change of stability can happen. It may be also shown that a change of stability corresponds to a change of sign of an eigenvalue of $\partial_{ij} S$.

The conditions for the onset of the instability can often be obtained from the topological properties of the series of equilibrium close to these bifurcations points in the (S, ξ) plane. Let ξ_0 be a bifurcation point. In the plane (S, ξ) we can consider S along a series of equilibrium as a function of the parameter ξ only, so that:

$$S^{(a)}(\xi) = S(X_i^{(a)}(\xi), \xi). \tag{2.4}$$

The ξ-derivative of $S^{(a)}(\xi)$ is called the *conjugate parameter* of ξ and, under sufficient regularity of S and $X_i^{(a)}$, we can write the ξ-derivative of the conjugate parameter, i.e. the second derivative of S as:

$$\frac{d^2}{d\xi^2} S^{(a)}(\xi) = (\partial_{\xi\xi} S)^{(a)} + (\partial_{\xi i} S)^{(a)} \frac{d}{d\xi} X_i^{(a)}, \tag{2.5}$$

for $\xi \neq \xi_0$. If we assume that the form $(\partial_{ij} S)^{(a)}$ is diagonal with eigenvalues $k_i^{(a)}$, we can rearrange the expression above (remembering that we are on the equilibrium sequence) to obtain, for $\xi \neq \xi_0$:

$$\frac{d^2}{d\xi^2} S^{(a)}(\xi) = (\partial_{\xi\xi} S)^{(a)} + \sum_{i=1}^{n} \frac{((\partial_{\xi i} S)^{(a)})^2}{k_i^{(a)}(\xi)}. \tag{2.6}$$

The derivative of the parameter conjugate will be in general discontinuous at a bifurcation point; if this derivative is infinite, then the second term dominates the equation above, and thus a change of sign in the derivative is associated with a change of sign of one of the eigenvalues $k_i^{(a)}(\xi)$. The onset of an instability can thus be inferred by the topological properties of the series of equilibrium near the bifurcation points, if the plot of the conjugate parameter with respect to ξ shows a vertical tangent at those points.

Katz (1978) classifies all the possible topological configurations. The spiral-like form for the graph $(\xi, dS(\xi)/d\xi)$ is typical of the gravothermal instability (e.g. see our plot in Fig. 2.2) and implies the onset of a new unstable mode at every point with vertical tangent.

In the case of the gravothermal collapse for a self-gravitating system embedded in a confining shell, the underlying set of variables x_i is infinite (Katz 1978), and the equilibrium configurations can be parametrized in terms of the total energy E_{tot}. Thus the parameter conjugate to the energy (at fixed mass and volume) is the inverse of the temperature $1/T = (\partial S/\partial E_{tot})_{M,V}$. After some algebra (Lynden-Bell & Wood 1968) it can be shown that $1/T = \beta$ (with the distribution function written as $f = A \exp\{-\beta E\}$). The gravothermal instability sets in at the first point with vertical tangent in the graph (β, E_{Tot}) (see Fig. 3 in Katz 1978; see also Fig. 2.2), corresponding to a ratio of the central to edge density of ≈ 709 (e.g., see Lynden-Bell & Wood 1968 and Padmanabhan 1989).

2.1.3 Gravothermal collapse for more realistic models

The symple framework of analysis presented above cannot in general be easily extended to include realistic models for stellar systems. In fact, a rigorous derivation of the onset of the gravothermal catastrophe from a study of the Boltzmann entropy appeared to be available only for the case of ideal systems confined by a spherical reflecting wall. A number of convincing qualitative arguments made it clear that also unbound stellar systems with finite mass, such as those described by the King sequence (King 1966; these spherical models have a finite radius, but do not require an external wall), should probably fall into the same physical framework and indeed the paradigm received

a lot of attention, especially in the context of the dynamics of globular clusters (see Spitzer 1987), which are known to possess, at least to some extent, the desired internal collisionality (see also Lynden-Bell & Eggleton 1980). [An indirect indication that the general physical picture of the gravothermal catastrophe is likely to be robust comes also from the proof that the behaviour of the classical gas case is basically independent of the assumption of spherical geometry (Lombardi & Bertin 2001).]

Several investigations have aimed at producing a rigorous derivation of the gravothermal catastrophe for unbound stellar systems, focusing on the underlying argument that refers to the Poincaré stability of linear series of equilibria (Katz 1978, 1979; Padmanabhan 1989), but the proof has always been centered on an unjustified *Ansatz* in order to connect the underlying entropy S with the global temperature $T = 1/(\partial S/\partial E_{tot})$ (see Appendix V in the article by Lynden-Bell & Wood 1968; Katz 1980; Magliocchetti et al. 1998). Other investigations have explored the possibility of setting the discussion in the context of non-standard entropies (e.g., the Tsallis entropies; see the study of the polytropic spheres by Chavanis 2002 and Taruya & Sakagami 2002). Note that the concept of entropy for collisionless systems is quite subtle (e.g., see Stiavelli & Bertin 1987 and references therein). One might even argue whether it is actually compatible with the long-range nature of gravity, given the fact that self-gravitating systems lack additivity, a key ingredient in thermodynamics.

In the meantime, inspired by N-body simulations of collisionless collapse (van Albada 1982), which confirmed the general picture of incomplete violent relaxation and showed that it can lead to systems with realistic density profiles without ad hoc tuning of the initial conditions, some families of models were constructed able to reproduce, for quasi-spherical configurations, the characteristic feature of the anisotropy profile with an inner isotropic core and an outer radially biased envelope (Bertin & Stiavelli 1984; see Bertin & Stiavelli 1993 and references therein): these families turned out to exhibit the characteristic $R^{1/4}$ projected density profile and indeed were shown to match nicely the observed photometric and kinematic characteristics of bright ellipticals. In an attempt at providing a justification of these models (in particular, of the so-called f_∞ models, constructed initially only from dynamical arguments) from statistical mechanics, two routes were pursued (Stiavelli & Bertin 1987).

The first combines an explicit statement of partial relaxation, i.e. of a relaxation process that is expected to be inefficient in the outer regions, and the existence of a suitable weight, related to the orbital period, for the cells that make the relevant partition of phase space; it follows qualitative arguments proposed by Lynden-Bell (1967) and is physically appealing (see also

Tremaine 1986). It was indeed shown to lead naturally to the f_∞ models. However, this route is not fully satisfactory from the mathematical point of view, especially since it involves an explicit approximation for the orbital period that is applicable only to the low binding energy limit of quasi-Keplerian orbits. The second route is straightforward from the mathematical point of view, being based on the classical Boltzmann entropy and on the assumed explicit conservation of a third quantity Q, in addition to the total mass M and to the total energy E_{tot}. It was shown to lead to an analytically different family of models (the $f^{(\nu)}$ models; see definition in Sect. 2.4 below), with qualitative properties similar to those of the f_∞ models. Those models were not studied much further and did not receive great attention, not only because the relevant distribution function is not as simple as that of the f_∞ models, but especially because the conservation of Q could only be justified approximately by inspection of a number of N-body simulations, without a clear-cut physical justification (see Stiavelli & Bertin 1987; in contrast, the conservation of the additional $\mathbf{A} \cdot \mathbf{B}$ invariant sometimes invoked in plasma physics is rather transparent; see Chandrasekhar & Woltjer 1958).

In this Chapter we introduce the $f^{(\nu)}$ models and we take advantage of their simple statistical mechanics foundation to explore the possibility of a thermodynamical description of stellar-dynamical models that are endowed with realistic properties.

A detailed description of the $f^{(\nu)}$ models is deferred to Chapter 5, where we discuss extensively their dynamical properties and we present a first comparison with observations.

2.2 Should galaxies be modeled as pure collisionless stellar systems?

Apparently the framework of the gravothermal catastrophe does not appear to be relevant for the $f^{(\nu)}$ models, that have been derived with the goal of descripting collisionless objects such as elliptical galaxies. We thus make a short digression in order to bring out the connections between the present analysis and the evolution of elliptical galaxies.

We start by recalling that, formally, the sequence of King (1966) models is one special family of solutions of the collisionless Boltzmann equation. Yet, it is recognized to provide a reasonable description of the current properties of globular clusters (see Djorgovski & Meylan 1994), within a framework where these stellar systems continually evolve as a result of a variety of mechanisms (among which star evaporation and disk shocking; see Vesperini

1997 and references therein) and where the paradigm of the gravothermal catastrophe can be applied (see Spitzer 1987). Of course, it is well known that the level of internal collisionality in globular clusters is relatively high, so that the above approach is quite natural.

In contrast, one might at first think of dismissing the possibility that the paradigm of the gravothermal catastrophe should be of interest for the study of elliptical galaxies, because these large stellar systems lack the desired level of collisionality, judging from the estimate of the relevant star-star relaxation times. Here, following the spirit of earlier investigations (starting with Lynden-Bell & Wood 1968), we note that real elliptical galaxies are actually complex systems the evolution of which goes well beyond the idealized framework of the collisionless Boltzmann equation. In other words, splitting their description into past (formation) processes and present (mostly collisionless equilibrium) conditions should be considered only as an idealization introduced in order to assess the properties that define their current basic state (Bertin & Trenti 2003).

In practice, elliptical galaxies are expected to be in a state of continuous evolution, for which we can list several specific dynamical causes: (1) Leftover granularity of the stellar system itself from initial collapse. Clumps of stars are likely to continue to form and dissolve in phase space even after the system has reached an approximate steady state. This acts as internal collisionality thus making some relaxation proceed even at current epochs. Indeed, numerical simulations of violent (partial) relaxation show that some evolution continues well after the initial collapse has taken place. (2) Drag of a system of globular clusters or other heavier objects towards the galaxy center. A globular cluster system or the frequent capture of small satellites (mini-mergers) may provide an internal heating mechanism associated with the process of dynamical friction by the stars on the heavier objects (Bertin et al. 2003). (3) Long-term action of tidal interactions of the galaxy with external objects. (4) Presence of gas in various phases (cold, warm, and hot). Significant cooling flows have been observed in bright ellipticals. Traditionally, studies of processes of this kind focus on the dynamics of the cooling gas and keep the background stellar system as 'frozen'. In reality, energy and mass exchanges take place between the stellar system and the interstellar medium. (5) Interaction between the galactic nucleus and the galaxy. A number of interesting correlations have been found between the properties of galaxy nuclei and global properties of the hosting galaxies (e.g., see Pellegrini 1999). These correlations suggest that significant energy exchanges are taking place between the galaxy and its nucleus. Eventually, if a sufficiently concentrated nucleus is generated, then star-star relaxation in the central regions may also become a significant cause of dynamical evolution.

All of the above are specific mechanisms that are expected to make elliptical galaxies evolve in spite of their very long typical star-star relaxation time. Most of these processes are hard to model and to calculate in detail. As for the evolution of other complex many-body systems, it is hoped that thermodynamical arguments may help us identify general trends characterizing such evolution. This is the basic physical scenario in which the calculations presented in this Chapter are expected to be of interest for real elliptical galaxies.

2.3 Physical approach to the construction of self-consistent models

We introduce here a short digression and briefly recall that there are different approaches to the construction of models (i.e. distribution functions) for collisionless stellar systems that are meant to represent observed astronomical objects.

One straightforward approach to the problem is to start directly from a specific distribution function, expressed in terms of the integral of motions for single particle orbits in a mean potential Φ with given symmetry; such a function automatically satisfies the Collisionless Boltzmann Equation (Jeans theorem). The self-consistent potential is then determined by integrating the Poisson equation, which is reduced to a non linear equation for Φ. The related self-consistent models are then studied in terms of quantities such as the intrinsic and projected density profiles and the velocity dispersion profiles to try to identify interesting models for astrophysical applications. Unfortunately, the variety of possible choices for the form of the distribution function is in principle infinite and thus the probability to pinpoint meaningful models in a blind search is extremely low.

Another possible approach would be to start from a given density profile $\rho(r)$ and from a mean potential $\Phi(r)$ and to try to infer from them a self-consistent distribution function f (i.e., such that $\rho = \int f d^3r$) expressed in terms of given integrals of motions for single particle in the mean field Φ (usually E or E and J). This fundamental problem of stellar dynamics is however not guaranteed to have a solution, since the techniques employed, such as the Abel inversion (Gorenflo & Vessella 1991; Bendinelli et al. 1993), can lead to a distribution function that is not positive definite and thus has to be rejected as unphysical[2].

[2]The reason for this potential failure in the inversion process is related to the fact that only a finite number of constraints on the infinite set of moments of the distribution

Even neglecting the complications associated to the inversion from ρ to f, one has to specify a given density and potential profile to start with. If we are interested in constructing a distribution function to represent the properties of simulated N-Body systems, this step is straightforward, since we can measure directly these quantities from the simulations. On the other side, if the main interest is focused on the comparison with real stellar systems, such as elliptical galaxies, one has to rely on the constraints imposed by the observations. However, at variance with some laboratory or space plasmas, in which it is possible to diagnose interesting phase space properties of the system under investigation, observations of external galaxies offer very little inspiration for the construction of a reliable self-consistent kinetic model. In fact we face two intrinsic limitations: (1) photometric and spectroscopic data points sample only limited spatial regions with finite accuracy; (2) when observed as astronomical objects galaxies appear projected on the plane of the sky, so that deprojection techniques are needed to reconstruct the intrinsic (i.e. three dimensional) dynamical properties of the observed objects. The deprojection of the data requires specific assumptions on the geometry of the system and usually is carried out under the assumption of spherical symmetry.

The two previous paths are consequently unsatisfactory. One may thus try to combine them and use the observations and the numerical simulations in order to derive a set of constraints on the dynamical properties of the models that we would like to build. These constraints are thus taken into account for chosing a reliable candidate distribution function f, whose properties can then studied in detail and compared *a posteriori* with the end products of numerical simulations or with the observations. The problems associated to the inversion from ρ to f are thus bypassed. One interesting way to constraint the form of the distribution function is by means of statistical mechanics arguments, that, e.g., inspired the construction as truncated Maxwellians of the King models (King 1966) with the goal of describing globular clusters. The statistical mechanics approach has also been applied (Stiavelli & Bertin 1987, see also next Section) to derive the distribution function of the $f^{(\nu)}$ models, by imposing the conservation of an additional quantity that is approximately conserved in collisionless collapse simulations.

To furter explore new interesting models, one may also try to investigate the properties of distribution functions that generalize some known and popular models. Along this line one successful example is the introduction of radial anisotropy (which is expected to be present in elliptical galaxies) starting from an isotropic $f(E)$. A distribution function $f(E)$ can in fact be

function is applied.

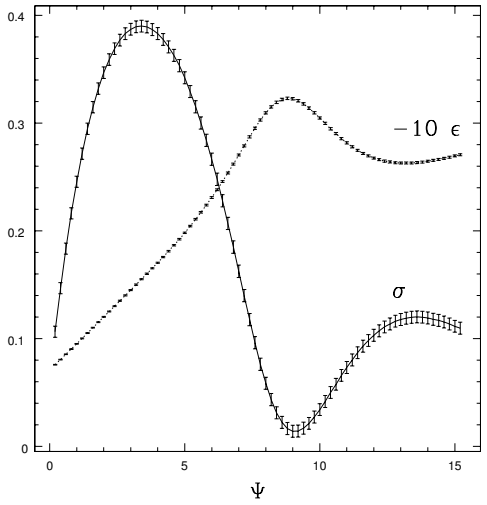

Figure 2.1: Specific entropy and total energy along the equilibrium sequence of $f^{(\nu)}$ models with $\nu = 1$ (as a function of the concentration parameter Ψ, at constant M and Q, and thus expressed by means of the functions $\sigma(\Psi)$ and $\epsilon(\Psi)$ defined in the text).

remapped into $f(E + J^2/r_a^2)$, with r_a being a free parameter that controls the degree of anisotropy introduced into the system (Osipkov 1979; Merritt 1985).

2.4 The $f^{(\nu)}$ family of models

Following the idea of building a collisionless model for partially relaxed stellar systems starting from statistical mechanics, let us consider the standard Boltzmann entropy

$$S = -\int f \ln f d^3x d^3w \tag{2.7}$$

and look for functions that extremize its value under the constraint that the total energy

$$E_{tot} = \frac{1}{3}\int E f d^3x d^3w, \tag{2.8}$$

the total mass

$$M = \int f d^3x d^3w, \tag{2.9}$$

and the additional quantity

$$Q = \int J^{\nu} |E|^{-3\nu/4} f d^3x d^3w \tag{2.10}$$

are taken to be constant. Here the functions E and J^2 represent specific energy and specific angular momentum square of a single star subject to a spherically symmetric mean potential $\Phi(r)$. (We have decided to use the symbol w, instead of v, for the velocity variable so as to avoid confusion with the symbol ν.) Some arguments have been provided as to why a quantity such as Q should be, at least approximately, conserved (Stiavelli & Bertin 1987) and those will not be repeated here. In any case, the conservation of Q should be taken for the moment as a conjecture. In Chapter 6 we will discuss this problem further by examining a set of collapse simulations, for which the conservation of Q will be tested directly.

If only E_{tot} and M were kept fixed, the extremization process would lead to a Maxwellian, that is to an isothermal and isotropic distribution function, appropriate for a fully relaxed system. Here the extremization process leads, because of the assumed conservation of Q, to the following family of distribution functions:

$$f^{(\nu)} = A \exp\left[-aE - d\left(\frac{J^2}{|E|^{3/2}}\right)^{\nu/2}\right], \tag{2.11}$$

where ν, a, A, and d are positive real constants. This set of constants provides two dimensional scales (for example a mass scale $M_{scale} = Aa^{-9/4}d^{-3/\nu}$ and a reference radius $R_{scale} = a^{-1/4}d^{-1/\nu}$) and two dimensionless parameters. For the latter two quantities, we may refer to ν and $\gamma = ad^{2/\nu}/(4\pi GA)$. The distribution function is taken to vanish for unbound orbits, that is for $E > 0$.

The two-parameter family of models is then constructed by solving the Poisson equation:

$$\nabla^2 \Phi(r) = 4\pi G \int f^{(\nu)}(r, \vec{w}) d^3\vec{w}, \tag{2.12}$$

for the potential $\Phi(r)$ under the condition that the potential be regular at the origin and behaves like $-GM/r$ at large radii. This integration leads to an eigenvalue problem (see Sect 5.2) for which a value of γ is determined by the choice of the central dimensionless potential, $\gamma = \gamma(\Psi)$, with $\Psi = -a\Phi(r = 0)$. A given model will be denoted by the values of the two parameters $(\nu; \Psi)$ in parentheses. For the moment we restrict our discussion to the case $\nu = 1$, thus identifying a one parameter (Ψ) sequence, while in Chapter 5 we present

a systematic survey of the properties of the models over a wide range of the parameter space $(\nu; \Psi)$.

The main point of the following analysis is the determination of the Boltzmann entropy $S(M, Q, \Psi)$ and of the total energy $E_{tot}(M, Q, \Psi)$ along the sequence of models, i.e. as a function of the "concentration"[3] parameter Ψ defined above. These functions, at constant M and Q, are illustrated in Fig. 2.1. They have been obtained by noting that, from the definitions of S and $f^{(\nu)}$,

$$S = -M \ln A + 3aE_{tot} + dQ. \tag{2.13}$$

From the definitions $Q = Aa^{-9/4}d^{-1-3/\nu}\hat{Q}(\Psi)$ and $M = Aa^{-9/4}d^{-3/\nu}\hat{M}(\Psi)$ and the definition of γ, we can express the variables (A, a, d) in terms of the variables (M, Q, Ψ) and thus find that the entropy per unit mass can be written as $S/M = S_0(M, Q) + \sigma(\Psi)$, where S_0 is constant when the values of M and Q are fixed, with

$$\sigma = -\ln\left(\hat{M}^{\frac{4\nu-6}{5\nu}}\hat{Q}^{\frac{6}{5\nu}}\gamma^{-\frac{9}{5}}\right) + \frac{3\hat{E}}{\hat{M}} + \frac{\hat{Q}}{\hat{M}}\ . \tag{2.14}$$

Here $\hat{E} = \hat{E}(\Psi)$ is the dimensionless total energy defined from $E_{tot} = Aa^{-13/4}d^{-3/\nu}\hat{E}$. From the identity $aE_{tot}/M = \hat{E}/\hat{M}$ and the expression of $a = a(M, Q, \Psi)$ obtained previously, we find $E_{tot}/M = H(M, Q)\epsilon(\Psi)$, with:

$$\epsilon = \gamma^{\frac{4}{5}}\hat{M}^{-\frac{9\nu+4}{5\nu}}\hat{Q}^{\frac{4}{5\nu}}\hat{E}\ . \tag{2.15}$$

The factor $H(M, Q)$ is a constant when M and Q are taken to be constant. At fixed ν, the quantities $\gamma(\Psi)$, $\hat{M}(\Psi)$, $\hat{Q}(\Psi)$, and $\hat{E}(\Psi)$ that enter the expression of σ and ϵ depend only on Ψ and are evaluated numerically on the equilibrium sequence.

This completes the derivation that allows us to draw the analogy with the classical paper of Lynden-Bell & Wood (1968). This step, straightforward for the $f^{(\nu)}$ models, is by itself interesting and new. In fact, other attempts at applying the paradigm of the gravothermal catastrophe to stellar dynamical equilibrium sequences were either based on an unjustified *Ansatz* for the identification of the relevant temperature (e.g., see Appendix V in the article by Lynden-Bell & Wood 1968; Katz 1980; Magliocchetti et al. 1998) or on the use of non-standard entropies (for less realistic models; Chavanis 2002).

[3]For a precise definition of the concentration and for its relationship with Ψ see Sect. 5.2.1.

2.5 The onset of the gravothermal catastrophe for concentrated models

When the $f^{(\nu)}$ models were constructed (Stiavelli & Bertin 1987), it was immediately realized that they have general properties similar to those of the f_∞ models (Bertin & Stiavelli 1984); in particular, for values of $\nu \approx 1$, sufficiently concentrated models along the sequence tend to settle into a well defined overall structure, except for the development of a more and more compact nucleus, as the value of Ψ increases, and are characterized by a projected density profile very well fitted by the $R^{1/4}$ law characteristic of the surface brightness profile of bright elliptical galaxies. This property is illustrated in Fig. 2.3.

Now, by inspection of Fig. 2.1 and by analogy with the study of the isothermal sphere (Lynden-Bell & Wood 1968), we can identify the location at $\Psi \approx 9$ as the location for the *onset of the gravothermal catastrophe*. This sequence of models thus has the surprising result that the value of Ψ that defines the onset of the gravothermal catastrophe is that around which the models appear to become realistic representations of bright elliptical galaxies (see also the comparison with *NGC3379* presented in Sect. 5.5).

We note that in this regime of high concentration the general properties of the gravothermal catastrophe are reasonably well recovered by the use of the *Ansatz* that the temperature parameter conjugate to the total energy is a, a quantity directly related to the velocity dispersion in the central regions. Basically, this was the *Ansatz* made in the discussion of the possible occurrence of the gravothermal catastrophe for the King models or for other sequences of models (e.g., see Lynden-Bell & Wood 1968, Katz 1980, Magliocchetti et al. 1998). Here we have proved that the application of a rigorous derivation, which is available in our case, gives rise to relatively modest quantitative changes in the $(E_{tot}, 1/T)$ diagram for values of Ψ close to and beyond the onset of the catastrophe (see Fig. 2.2). However, in Sect.2.7 we will draw the attention to an interesting, qualitatively new phenomenon missed in the previous derivations based on the use of the *a-Ansatz*.

In passing, we note that in this regime of relatively high concentrations, the $f^{(\nu)}$ models possess one intrinsic property that makes them more appealing than the widely studied f_∞ models. This is related to the way the models compare to the phase space properties of the products of collisionless collapse, as observed in N-body simulations (van Albada 1982). In fact, one noted unsatisfactory property of the concentrated f_∞ models was their excessive degree of isotropy with respect to the models produced in the simulations. Here we can easily check that the anisotropy level of the concentrated

$f^{(\nu)}$ models, while still within the desired (radial orbit) stability boundary and still consistent with the modest amount of radial anisotropy revealed by the observations, seems much closer to that resulting from N-body simulations of collisionless collapse; in particular, the anisotropy radius r_α, defined from the relation $\alpha(r_\alpha) = 1$, with $\alpha = 2 - (\langle w_\theta^2 \rangle + \langle w_\phi^2 \rangle)/\langle w_r^2 \rangle$, is close to the half-mass radius r_M (while for the f_∞ models it is about three times as large). This is illustrated in Fig. 2.4.

2.6 The $R^{1/4}$ law and deviations from it

The intermediate Ψ regime (the precise point that marks the low Ψ regime will be identified in the next Section) is a regime where the models appear to be stable, with respect not only to the gravothermal catastrophe (following the arguments provided earlier; but we should recall that the catastrophe is expected to require a sufficiently high level of effective collisionality in order to take off) but also to other instabilities (see our set of simulations in Sect. 4.2). The relatively wide variations, between $\Psi = 3.5$ and $\Psi = 9$, in all the representative quantities that characterize the equilibrium models suggest that this part of the sequence could be used to model the weak homology of bright elliptical galaxies (see Bertin et al. 2002), much like the sequence of King models is able to capture observed systematic variations in the structure of globular clusters (see Djorgovski & Meylan 1994). In this regime the projected surface brightness of the models can in fact be well represented by a Sersic $R^{1/m}$ law (Sersic 1968; $m = 4$ corresponds to the $R^{1/4}$ law proposed by de Vaucouleurs 1948) with $2 \lesssim m \lesssim 8$, as discussed in Sect. 5.3.2.

2.7 Negative global temperature and the radial orbit instability

The low Ψ regime is marked by an unexpected and significant difference with respect to the low concentration limit of the classical isothermal sphere (Bonnor 1956; Lynden-Bell & Wood 1968). In fact, while the classical case reduces to the ideal non-gravitating gas, to which Boyle's law applies, for the $f^{(\nu)}$ models the system remains self-gravitating and with a significant central concentration (see Fig. 5.2). A clear-cut proof of this difference is given by inspecting the behavior of the global temperature T, identified from the thermodynamical definition $T = 1/(\partial S/\partial E_{tot})$. While the temperature defined by the *a-Ansatz* remains obviously positive definite, by definition,

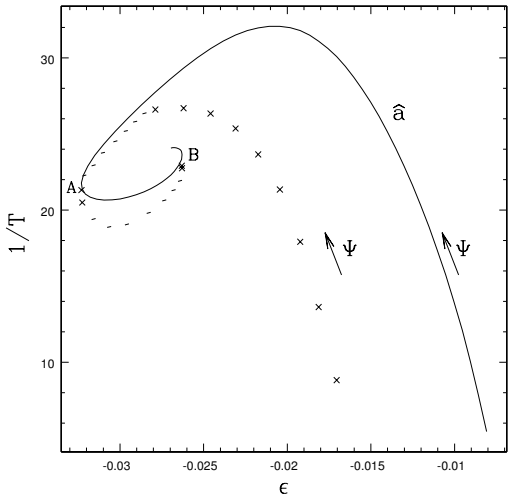

Figure 2.2: Instability spiral of $f^{(\nu)}$ models with $\nu = 1$. The solid line refers to the results obtained with the *a-Ansatz* (with $\hat{a} = \gamma^{-4/5}\hat{M}^{(\nu+1)/(5\nu)}\hat{Q}^{-4/(5\nu)}$ identified as inverse effective temperature). Crosses represent the global temperature from the definition $\partial S/\partial E_{tot}$; other symbols indicate estimated points for which the adopted numerical differentiation is less reliable. The values of Ψ and ϵ for points A and B with a vertical tangent, where unstable modes set in if the system is isolated, remain unchanged.

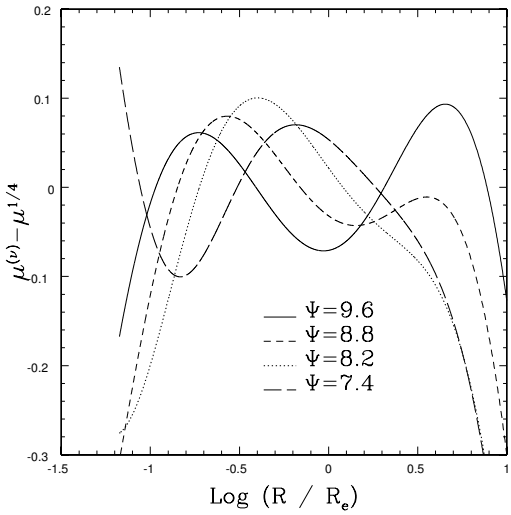

Figure 2.3: Residuals $\mu^{(\nu)} - \mu^{1/4}$ obtained by fitting the $R^{1/4}$ law to the projected density profile of $f^{(\nu)}$ models for $\nu = 1$ and some values of Ψ.

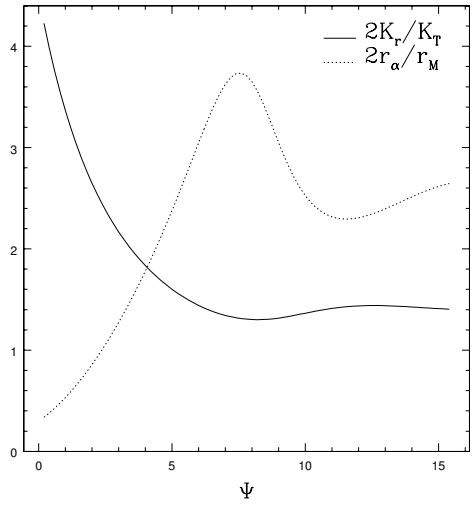

Figure 2.4: Anisotropy along the equilibrium sequence: anisotropy radius in units of the half mass radius $2r_\alpha/r_M$ and the anisotropy parameter $2K_r/K_T$ (ratio of total kinetic energy in the radial direction to that in the tangential directions) of $f^{(\nu)}$ models with $\nu = 1$.

if we look at Fig. 2.1 we see that the global temperature T changes sign at $\Psi \approx 3.5$. This marks a drastic qualitative deviation from the classical studies.

Here we note a curious coincidence of this transition value of Ψ with the value around which the sequence is bound to change its stability properties with respect to the radial orbit instability (Polyachenko & Shukhman 1981). Indeed, the location where the sequence is expected to become unstable in this regard is precisely that defined by $\Psi \approx 3.5$, as can be judged from inspection of Fig. 2.4; around those values of Ψ the level of radial anisotropy, as measured by $2K_r/K_T$ reaches the threshold value of $1.8 - 2$, known to be sufficient for the excitation of the instability (the precise value of $2K_r/K_T$ corresponding to marginal stability is model dependent; for some sequences the reported value is below the range suggested by Polyachenko & Shukhman 1981; see also Chapter 4).

These clues appear to be interesting and important, but more work is required before a final claim can be made that there is indeed a direct relation between the dynamical radial orbit instability and the fact that the system possesses a negative global temperature, as we found based on the simple work presented here.

2.8 Conclusions

A relatively straightforward and simple thermodynamical description of an equilibrium sequence constructed earlier and known to possess realistic characteristics with respect to bright elliptical galaxies shows that, on the one hand, the paradigm of the gravothermal catastrophe may be adequate to explain the occurrence of realistic properties in models of collisionless stellar systems and, on the other hand, a long-known dynamical instability might be interpreted in terms of a thermodynamical argument.

Probably the main open question regarding the models discussed here, partially addressed in previous studies (see Stiavelli & Bertin 1987), is to what extent the quantity Q is actually reasonably well conserved during incomplete violent relaxation. The investigation of this issue, which will be presented in the next Chapters, combined with other dynamical and thermodynamical considerations, will turn out to lead to the identification of the $f^{(\nu)}$ models as a family of equilibrium models with optimal behavior with respect to statistical mechanics, with respect to what we know about collisionless collapse, and with respect to the problem of providing a realistic representation of bright elliptical galaxies.

Chapter 3

Simulating stellar systems

In this Chapter we discuss the different numerical techniques that can be employed to simulate collisionless stellar systems. In particular we describe in detail the structure, the performance and the available diagnostic subroutines of the Collisionless Galactic Simulator (CGS), a particle-grid code that we have developed. This Chapter constitutes also a user manual for the CGS code, where the motivations behind the choices operated while designing the program are critically analyzed.

3.1 Review of numerical methods

Numerical simulations of self-gravitating systems have become an invaluable tool in stellar dynamics and are extensively used to study many problems, often three-dimensional and/or non-linear. In fact, in those cases the study with purely analytical methods is usually restricted to highly idealised treatments, or to "toy models". In recent years computer performance has grown together with the development of new and more powerful simulation codes.

In principle, two approaches to the problem of simulating a self gravitating stellar system are possible.

One may run a simulation using one particle for each body (star) in the system. This approach is extremely demanding from the point of view of computational time, since the complexity of the gravitational interaction scales as the square of the number of particles employed. Thus at present the method is viable only to simulate the dynamics of stellar systems with sizes up to that of a globular cluster (i.e. with a order of 10^5 particles). In this Thesis we are mainly interested in the dynamics of elliptical galaxies, where the number of stars is many orders of magnitude greater than the number of particles that current computers can handle. We will thus just review below

the basic ideas at the base of direct simulations, redirecting the interested reader for further details to the specialized literature on the topic (see, e.g. Heggie & Hut 2003, and references therein).

Thus, if the number of physical constituents of the system is too high for the available hardware, a direct simulation may be computationally too expensive to be performed, and one may instead assume a mean field description using the formalism of distribution functions, i.e. consider that the dynamics be well represented by the Collisionless Boltzmann Equation (CBE):

$$\frac{\partial f}{\partial t} + \vec{w} \cdot \frac{\partial f}{\partial \vec{x}} - \frac{\partial \Phi}{\partial \vec{x}} \cdot \frac{\partial f}{\partial \vec{w}} = 0, \tag{3.1}$$

where $f(\vec{x}, \vec{w}, t)$ is the one-particle phase-space distribution function of the system, and Φ is the gravitational potential generated by the system:

$$\nabla^2 \Phi(\vec{x}, t) = 4\pi G \int d^3\vec{w} f(\vec{x}', \vec{w}, t). \tag{3.2}$$

A direct solution of the CBE (Equation 3.1) on a Eulerian grid, in the six dimensional phase space, encounters severe memory limits (a low resolution grid with 30 elements in each dimension would require several Gigabytes of memory just to be stored[1]). Thus the problem is usually approached by using the method of the characteristics (see, e.g. Ciotti 2000, Chapter 3): since Equation (3.1) states that f is constant along all the trajectories, we can obtain a representative sample of the distribution function f at time t by sampling it at time 0 and evolving the so obtained N-body system. However there is a crucial physical difference between this kind of N-body systems and those related to exact collisional methods. The particles in a collisionless N-body simulation *do not* represent physical entities, but are rather Monte Carlo representations of an underlying continuous distribution function. Thus these particles should interact with one another only via a mean field, i.e. the exchange of energy due to direct encounters must be suppressed in the simulation.

3.1.1 Direct methods

Here we start by reviewing the standard methods used in direct N-body simulations. We recall however that these methods are not appropriate for simulations of collisionless systems.

In principle implementing an exact N-body simulation is straightforward. The evolution of the system is governed by a system of second order ordinary

[1]However codes with a *five* dimensional cartesian grid are used for similar simulations in the area of plasma physics (e.g., see Mangeney et al. 2002).

differential equations (ODE) where the acceleration $\vec{a}_{(i)}$ on a particle i is given by the direct gravitational interaction with each other member j of the system[2]:

$$\vec{a}_{(i)} = -G \sum_{j=1;\ j\neq i}^{N} m_{(j)} \frac{\vec{x}_{(i)} - \vec{x}_{(j)}}{|\vec{x}_{(i)} - \vec{x}_{(j)}|^3}. \tag{3.3}$$

The positions and velocities at a given time that define the initial conditions for the ODE can be advanced by a given time step Δt with one of the standard methods to solve differential equations, such as a Runge-Kutta or Hermite scheme (e.g., see Press et al. 1986, Chapter 8). Unfortunately, a naive approach to direct stellar dynamics has to face several problems. In fact, not only the computational complexity of a direct code scales as N^2, but also large errors can arise when two particles are close together if the time step is not chosen appropriately. In fact, the dynamical time scale for close encounters (where $|\vec{a}|$ can diverge) can be orders of magnitude smaller than the mean dynamical time scale for the system. If the same time step is shared by all the particles, one must choose between accepting unbound errors or reducing the time step to the scale set by the close encounters. The latter choice can also have severe consequences in a simulation, since a huge amount of computing time will be spent by advancing all the particles on a time scale much less than their typical dynamical time, so that the system will appear as "frozen".

To allow accurate and reliable simulations sophisticated techniques have been developed, such as individual time steps and special (exact or asymptotic) treatment of two and three body encounters via the so-called KS transformations (Kustaanheimo & Stiefel 1965). A review of these collisional methods is outside the scope of this Thesis; the interested reader may consult the monography by Heggie & Hut (2003) and references therein.

One intrinsic limitation of exact techniques is that they are intrinsically demanding from the computational point of view, so that only systems with $N \lesssim 3\times10^4$ can be simulated on a standard workstation in a reasonable time (i.e. a week) over a time of the order of the two-body relaxation timescale (i.e. around $10^8 - 10^9 yr$ for typical globular clusters). A series of special purpose hardware designed to obtain high performance in computing the gravitational interaction has been recently developed (Makino et al. 2003): the *Grape-6* cluster in Tokyo is at the moment the fastest computer in the world, with a peak performance above 60 Teraflops. The next generation Grape hardware is expected to break the barrier of 1 Petaflops.

[2]This point is the key difference between collisional and collisionless methods; for the latter the particles interact via a mean field.

3.1.2 Tree codes

In these numerical schemes, the information about the density field is set up in the form of a hierarchical tree. Each level of the tree specifies for a region in the simulation volume the position of the center of mass, the total mass (monopole moment) and higher moments of the mass distribution (usually up to the quadrupole term). The tree can be constructed by recursively subdividing the simulation volume (enclosed in a cube of size L_{box}) into eight equal parts at each level, as in the scheme proposed by Barnes & Hut (1986). This subdivision of cells is continued until there is at most one particle per cell at the smallest level (see Fig. 3.1). The interaction at small scales is softened to suppress direct encounters making these schemes suitable for collisionless N-body simulations. The collective force by particles in distant regions in the simulation box is approximated by the force from the center of mass of the region, computed up to the desired multi-pole expansion. This approximation to compute the force on a particle i from a region of size L_R is used if the distance of the center of mass of the region from the particle i is greater than L_R multiplied by an accuracy parameter. This leads to a reduction in the number of operations required for calculating the force. [For a detailed discussion see, e.g. Barnes & Hut 1986]. To estimate the number of operations for setting up the tree structure and for evaluating the force we note that during the tree building phase each particle is parsed at most once at each level, therefore the upper bound on the total number of operations is proportional to $N \ln(L_{box}/l_{min})$ where l_{min} is the smallest inter-particle separation for the given distribution of particles. We have,

$$l_{min} \propto n_{max}^{-1/3} = \delta_{max}^{-1/3} \langle n \rangle^{-1/3} = N^{-1/3} L_{box} \delta_{max}^{-1/3} \tag{3.4}$$

where $\langle n \rangle$ is the average number density, δ_{max} is the maximum density contrast and n_{max} is the highest number density in the given distribution of particles ($n_{max} = \delta_{max} \langle n \rangle$). This implies that the upper bound on the number of operations is, in the leading term, $O(N \ln N)$. Similarly, it can be shown that also the force calculation scales as $O(N \ln N)$ in the algorithm. Recently a fast tree-like method (*GyrFalcON*), i.e. one that scales linearly with N, has been proposed (Dehnen 2000, 2001). We have used the fast tree code of Dehnen both as a validation tool for our particle-mesh code (see Sect. 3.6) and as an independent code to run some simulations of violent collapse (see Chapter 6).

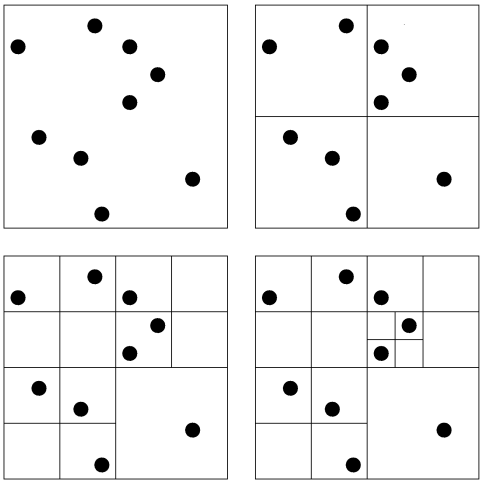

Figure 3.1: Tree building, with a hierarchical partition method from first panel (upper-left) to the bottom-right one.

3.1.3 Particle-Mesh (PM) codes

This class of N-body methods is based on the use of a grid, usually Cartesian, for computing the potential and the force. The Poisson equation is solved in the Fourier domain by computing on the mesh the density field, which is the source for the gravitational potential, starting from the particle positions and using a suitable interpolating function. The force is then interpolated, using the same grid, to the particle positions in order to move them. This "smoothing" of the particles (which effectively assume a finite size, extended over a few grid cells) limits the resolution of the simulation to the scale of the grid size[3], but particles interacts only via the mean field, and thus the evolution is nearly collisionless. This property makes PM codes the natural choice for numerical simulations of N-body systems associated with a discrete representation of a continuous distribution function (as is appropriate for collisionless systems). However, as we discuss in Sect. 3.5, there is a residual numerical collisionality measured as the rate of diffusion for the single-particle binding energies in equilibrium configurations. The complexity of PM codes scales linearly with the number N of particles used, allowing to employ easily more particles than in direct or tree code simulations.

To obtain higher spatial resolution a modification of the standard PM codes has been proposed: a Particle-Particle Particle-Mesh (P^3M) code (Ef-

[3]A cell must be large enough to contain several tens of particles so as to reduce errors induced by fluctuations of the occupation number.

stathiou et al. 1985). Here a correction to the mesh force is added for pairs of particles with separation of the order of, and smaller than, the grid length. While the complexity remains linear in the number of particles, the efficiency decreases when regions of high density are present.

3.1.4 Self Consistent Field (SCF) methods

This method, which broadly derives from PM schemes, solves the Poisson equation by expanding the density and the potential in a set of suitable basis functions. The expansion can be partial (see e.g. van Albada 1982; Villumsen 1982; McGlynn 1984) or complete (*SCFM,* Hernquist & Ostriker 1992). The key for the success of the SCF approach is to choose a basis whose first elements are suited to capture the global structure of the simulated system. If this is the case, the expansion can be truncated at relatively low orders with negligible errors. Usually this method is best suited to model the large-scale structure of systems with approximate symmetry (mostly spherical and with a regular density profile). The complexity of the method is linear in the number of particles N and (sub) linear in the number of members N_b of the basis functions used. This allows, as for the case of PM codes, to use millions of particles on a modern workstation. Furthermore this scheme can be naturally parallelized since at each step N 1-body problems are effectively solved instead of a single N-body problem.

The code constructed and used in this Thesis, developed as a tool for investigations on the formation and the evolution of spheroidal collisionless stellar systems is based on this idea and will be discussed in quantitative detail in Sect. 3.3.1.

3.2 The choice of the code for the goals of this Thesis

Among the variety of available N-body algorithms it is important to choose the most appropriate for the specific astrophysical problem one is interested in. As we have seen in the brief review above, each different method presents a trade-off between accuracy, complexity and introduction of undesired numerical effects.

In this Thesis we are interested in simulating the evolution of nearly spherical systems such as elliptical galaxies, which are thus made of many billions of stars. We are consequently excluding direct methods, since: (1) Each particle in the simulation is representative of many real stars and we want to suppress two-body encounters; (2) We would like to resolve a wide

dynamical range, from the central regions to the outer halo (i.e. we require the use of as many particles as possible at fixed CPU resources), so that we prefer a fast code, such as one based on the particle-mesh/self consistent field approach.

We have thus opted for a self consistent approach (van Albada 1982) based on the expansion in spherical harmonics, which can take advantage of the nearly spherical geometry of the configurations that we are interested in. Since we wish to study not only the stability of certain equilibrium configurations (see Chapter 4) but also the process of violent collapse (see Chapter 6), we have decided to use an adaptive radial grid that can match the different density profiles that arise during the collapse phase from cold initial conditions, before the system settles down in a stationary configuration.

The use of a spherically symmetric radial mesh combined with an expansion in spherical harmonics for the angular variables allow us to capture extremely well, with only relatively few particles (i.e. $\approx 10^6$), the large scale structure of the products of violent collapse over a wide dynamical range (i.e. almost 10 orders of magnitude in the density; see Chapter 6). Our choice is supported by the results of Lemson (1995), who compares the final states of cold collapse simulations performed with the original version of van Albada's code with those obtained by running the same simulations with a tree code. He finds very similar final density and anisotropy profiles. We have also performed a similar test by evolving the same initial conditions with our code and with GyrFalcOn, the fast tree code of Dehnen (2000), showing that the final properties differ by less than 10 %.

To be sure, if the initial conditions are too inhomogeneous, a mean field approach would not perform well. In these cases we use Dehnen's tree code as a preferred tool.

3.2.1 Softening, relaxation

Since the focus of this Thesis is on collisionless stellar dynamics, we would like to briefly discuss here what are the properties of the numerical methods (particle-mesh and tree code) that we use to simulate N-body systems with respect to two-body relaxation.

To define the typical two-body relaxation time scale, let us consider a test star in a N-body system. The orbit of this test particle will be scattered as a result of the direct gravitational interaction with the other stars of the system. On average, the net gain of velocity $\Delta v_\perp$ in the velocity component transverse to the direction of the motion will be zero, but the sum of $(\Delta v_\perp)^2$ will increase after each deflection. We define the relaxation time scale t_{rel} as the time at which the cumulative value of $(\Delta v_\perp)^2$ is of the order of the initial

specific kinetic energy of the test particle.

Assuming that the test particle (of mass m_t) has an initial velocity v_∞ and is incident upon a system of field stars, each of mass m_f, initially at rest and with uniform density, we can write the relaxation time as (Chandrasekhar 1942):

$$t_{rel} = \frac{v_\infty^3}{8\pi n G^2 m_f^2 \ln \Lambda}, \tag{3.5}$$

where n is the number density of the field stars and $\Lambda = b_{max}/b_0$ is the ratio between the maximum impact parameter b_{max} and a typical scale for the impact parameter b_0 (with $b_0 = G(m_f + m_t)/v_\infty^2$). The introduction of the cut-off b_{max} in the impact parameter is motivated by the fact that, due to the long range nature of the gravitational force, the quadratic variation of the deflection $\Delta v_\perp$ is unbound in an infinite homogeneous background.

If we now consider a gravitational N-body system of finite size in dynamical equilibrium, we can use the expression (3.5) and estimate the values assumed by v_∞, n, m_f and Λ. We obtain that the relaxation time t_{rel} is related to the dynamical time scale t_d, i.e. the typical crossing time for the system, by:

$$t_{rel} \approx \frac{N}{8 \ln N} t_d. \tag{3.6}$$

In this Thesis typical simulations have $N \gtrsim 10^5$ and the evolution of the N-body system is followed for $t_{run} \approx 20 t_d$, so that $t_{run} \ll t_{rel}$.

To suppress two-body relaxation we can resort to particle-mesh schemes that are formally truly collisionless. The particles do not "see" each other directly (two-body encounters are suppressed and no binaries can be formed), but rather interact only via the mean field. In reality, numerical effects such as Poisson noise and interpolation errors in the force assignment (usually the force is computed over the grid points and then interpolated to the particle positions) introduce artificial relaxation that mimics two-body relaxation. As discussed by Hernquist & Ostriker (1992), the collisionality present in the system may be quantified by measuring the single particle energy scatter during simulations of stable equilibrium configurations. In Sect. 3.5 we quantify this numerical diffusion for our CGS code compared to the SCFM implementation given by Hernquist & Ostriker (1992) finding that the level of relaxation is very similar in the two codes.

A possible solution for further reducing the collisionality could be the application of the recent results on wavelet filtering to "de-noise" particle-mesh simulations (Romeo et al. 2004). For specific dynamic configurations the authors claim an effective reduction of the noise by a factor ≈ 30, which would make the simulation equivalent, with respect to the relaxation properties, to

a standard realization with 100 times more particles. This result seems to be of great interest, but clearly more tests are needed to evaluate the general applicability.

Quite surprisingly, Hernquist & Ostriker (1992) find also that the level of relaxation, measured as the rate of diffusion in the single-particle energy space E, is rather similar to that of a typical tree-code with a softened interaction at small scales. This result is indeed interesting since here softening would not be expected to reduce much the two body-relaxation (Dehnen 2001; see also Theis 1998). In fact, as shown by Chandrasekhar (1943) and by Spitzer & Hart (1971), two-body relaxation is driven by close as well as by distant encounters: each octave in distance is contributing equally. Softening suppresses only the contributions by close encounters, while most of the relaxation is the result of noise on large scale, that cannot be erased with softening techniques. Hernquist (1987) also shows that a tree code has basically the same relaxation time-scale of an exact simulation with the same number of particles. This would thus imply that in practice the level of numerical relaxation in particle-mesh and self-consistent field codes, formally expected to be collisionless, is indeed not too different from that of exact simulations.

In closing we thus stress that the true benefit of softening, given either by the effective smoothing on the length scale given by the size of the cells (in PM codes) or by the softening length (in tree codes), is to avoid the formation of binaries and to suppress close encounters, which would be completely artificial in N-body simulations of the evolution of collisionless systems. The regularization of the force on small scales also allows to use efficiently the simple leap-frog integrator, which is known otherwise in direct simulations as highly inefficient.

3.3 The Collisionless Galactic Simulator (CGS) code

We first considered as ideal for our investigations the code introduced by van Albada (1982) (see also van Albada & van Gorkom 1977), which was used to run the pioneering *N-body* simulations of collisionless collapse that demonstrated how violent relaxation can act as a driver for the formation of elliptical galaxies. Unfortunately, the code performance was optimized for a typical number of particles smaller than 10^4 by the introduction of a three dimensional grid, logarithmic in radius and equally spaced in $\cos\theta$ and ϕ. The force interpolation from the grid to the particles was performed by

assuming a linear interpolation in θ. This introduces a numerical force along the z axis, which induces an artificial stretching of the simulated system. Due to this force, the energy and the angular momentum conservations were reduced to a level roughtly equivalent to that of a Poisson noise associated with $10^3 - 10^4$ particles.

When we began our work and tried to use the code with a higher number of particles (up to one million), we experienced poor accuracy. We soon realized that its source was the systematic effect of mis-interpolation mentioned above. In collaboration with van Albada we have cured the problem by rewriting the Poisson solver, as described in Sect. 3.3.3.

Although we should not claim yet to have improved the old code so as to make it competitive for general purposes with respect to state of the art implementations of tree codes, the *CGS* code performs very well for the class of applications we are interested in, being in line with the accuracy of the *SCFM* by Hernquist & Ostriker (1992) for all the tests that we have run. The new version of the code is certainly competitive and can be used successfully if its applications are focused on the evolution of quasi-spherical, smooth initial conditions.

Finally, by working on the new version of the code we had the opportunity to examine and to master the key problems that have to be faced in order to design an efficient and reliable code. And this was a great and exciting experience!

3.3.1 Structure

The key feature of the code is the solution, by means of Fourier techniques, of the Poisson equation $\nabla^2\Phi = 4\pi G\rho$, which relates the mean potential Φ of the system to the mass density ρ. Once the potential has been computed by expanding the density in spherical harmonics, the acceleration is obtained by numerical differentiation, and the particles are advanced by a fixed time step using a leap-frog scheme.

At variance with the original code by van Albada , to preserve accuracy and absence of systematic errors, we decided to drop the angular grid and to treat *exactly*, in terms of the single-particle Legendre polynomials, the angular dependence of the force.

This choice moves effectively the code toward the implementation of the self-consistent field code by Hernquist & Ostriker (see also Sect. 3.5 for a discussion of the differences between our and their approach). We still keep the radial grid because of its flexibility with respect to the initial conditions considered (we use a subroutine to generate a grid containing a fixed fraction of the total mass in each shell). During the simulation, the grid is updated,

if needed, at regular intervals, in order to follow properly the evolution of the density profile in non equilibrium conditions, such as those that arise during the collapse experiments starting from cold initial conditions that we have performed (see Chapter 6).

The time step is fixed for all the particles, but can be chosen, if desired, adaptively in order to ensure that the fastest particle is traveling for less than one grid spacing in one step. Introducing individual (or groups) time steps would not significantly impair the performance of the code. In fact, as discussed in Sect. 3.3.4, approximately 40% of the total CPU time is spent to compute the potential, an operation that must be performed at every time step, even if we want to advance only a few particles.

The code is completed by a subroutine to perform several optional diagnostic tests, such as the conservation of energy and angular momentum, the evolution of the Lagrangian radii (i.e. the radii of the spheres containing a fixed fraction of the total mass), the density and pressure anisotropy profiles, the single-particle binding energy and angular momentum distributions.

If desired, a snapshot with the individual masses, positions and velocities of all the particles at fixed times can be saved on the disk.

For the code we use a default system of units tuned on typical galactic scales. In fact, the mass unit is $10^{11} M_{\odot}$, the length unit 10 kpc, and the time unit 10^8 yr. This implies that the gravitational constant G assumes a value of ≈ 4.497, and that the unit for the velocity can be expressed as, approximately, 97.8 km/s. The system of units can, however, be easily changed by the user in the parameters file.

When possible we prefer to avoid the explicit mention of physical units (since in principle pure gravitational models are scale free) and we often report our results in terms of the dynamical time t_d defined as:

$$t_d = \frac{GM^{5/2}}{(-2E_{tot})^{3/2}}. \tag{3.7}$$

In Fig 3.2 we present a scheme of the main driver.

3.3.2 Advancing the particles: leap-frog, time reversibility

Particles are advanced in time using a simple leap-frog scheme (see, e.g. Hut & Makino 2004, Volume 3), written here for simplicity for one particle and in one dimension:

$$v_{t+\Delta t/2} = v_{t-\Delta t/2} + a(x_t)\Delta t + O(\Delta t^3), \tag{3.8}$$

$$x_{t+\Delta t} = x_t + v_{t+\Delta t/2}\Delta t + O(\Delta t^3), \tag{3.9}$$

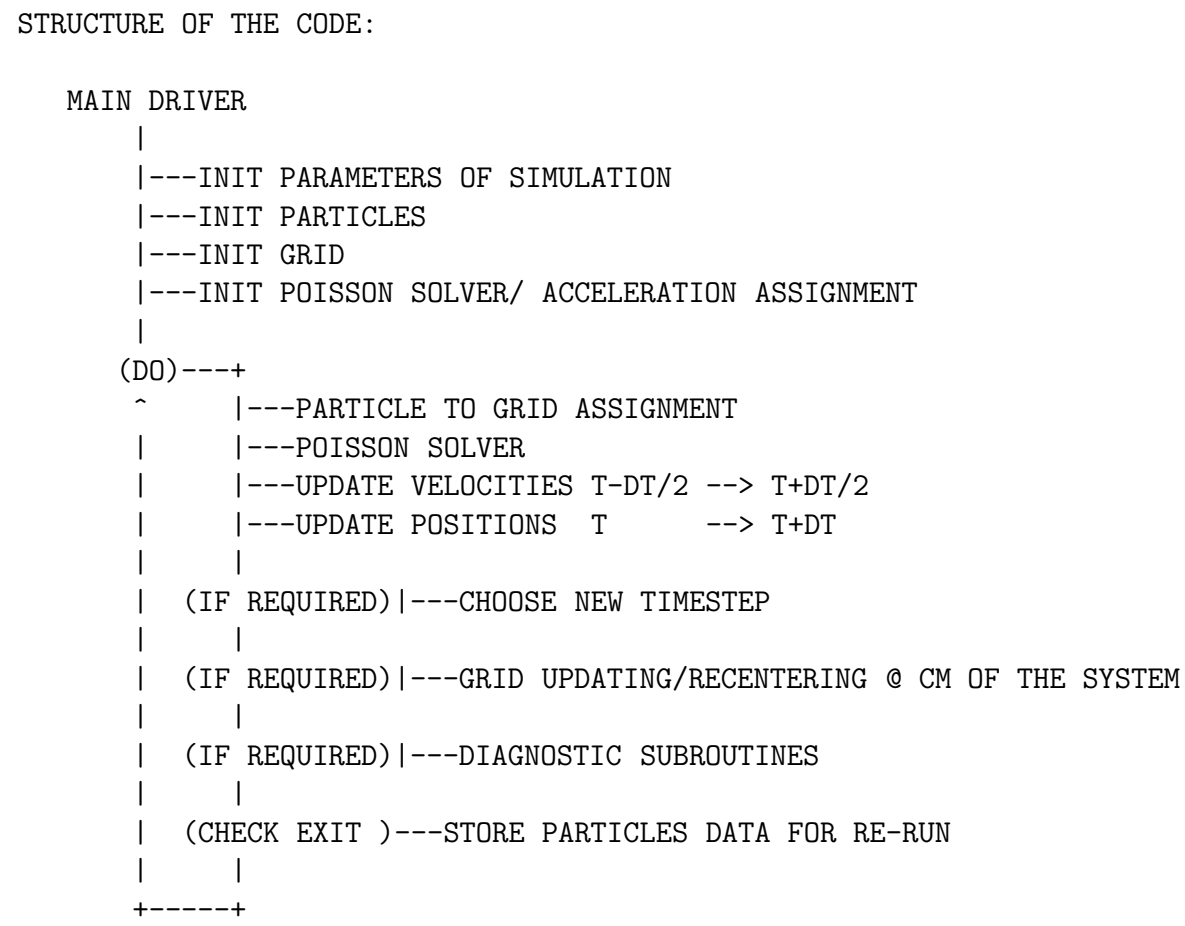

Figure 3.2: Scheme of the main driver of the *CGS* code.

where $a(x)$ is the gravitational acceleration. As can be seen from the above equations, in the leap-frog scheme the positions and the velocities are not defined at the same time, but are displaced by half a time step. In the numerical implementation of the *CGS* code we take into account this property by properly initializing the velocities at $-\Delta t/2$ at the beginning of the simulation and by updating the velocities by half a time step in the diagnostic subroutine.

This off-set of the velocities ensures (1) second order accuracy, although at first sight the scheme would appear to be only accurate to first order; (2) a time reversal symmetry of the two Equations (3.8-3.9), if the time step Δt is fixed. The latter fact can be proved easily by considering the application of one leap-frog time step $-\Delta t$ starting from $(x_{t+\Delta t}; v_{t+\Delta t/2})$ (the end state of Equations 3.8-3.9) and recalling that now, since we look back in time, the velocity is ahead in time with respect to the position and thus the position has to be updated first:

$$x_{(t+\Delta t)-\Delta t} = (x_t + v_{t+\Delta t/2}\Delta t) - v_{t+\Delta t/2}\Delta t, \tag{3.10}$$

$$v_{(t+\Delta t/2)-\Delta t} = (v_{t-\Delta t/2} + a(x_t)\Delta t) - a(x_t)\Delta t, \tag{3.11}$$

which, after simple manipulations of the right sides, give us exactly the original starting point $(x_t; v_{t-\Delta t/2})$.

However during a simulation the time symmetry for "long" runs is hard to preserve. In fact, small errors, such as interpolation approximations or truncations, appear at several points during the execution of the code, and these small errors give rapidly rise to an exponential divergence of the particles trajectories (see, e.g. Kandrup & Sideris 2003, and references therein). In our code we have verified that the typical time scale that ensures time reversibility is (much) greater than the dynamical time t_d. In fact we have evolved a Plummer model with 8×10^4 particles for $5t_d$ forward in time and then backward, ending up in a final state where the particle positions differ very little from the initial values (i.e. $\langle|\Delta\vec{x}_{(i)}|/|\vec{x}_{(i)}|\rangle \lesssim 0.02$). The code performs well also in non stationary conditions: we have tested time reversibility in a simulation where the system is unstable against radial orbit instability (see Chapter 4) and evolves toward a flattened configuration. By simulating backward in time the triaxial configuration obtained by evolving an unstable $(1/2; 3)$ $f^{(\nu)}$ model for 14 t_d we have been able to "rewind" the evolution of the system for more than 6 t_d with very small mean displacements both with respect to global properties, such as the ellipticity of the system, and to the individual orbits; for longer look-back times the chaotic nature of the system is evident and the radial orbit instability triggers again (see Fig. 3.3).

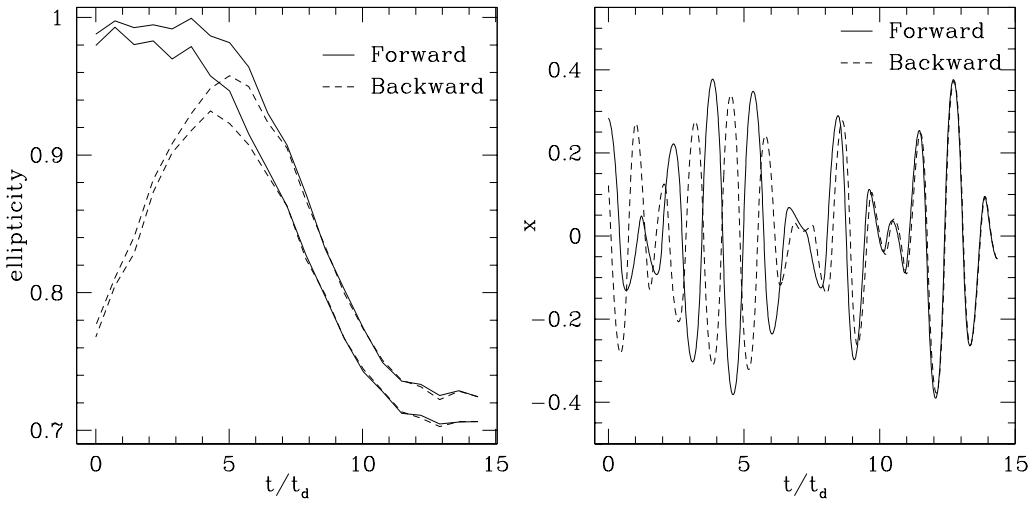

Figure 3.3: Evolution forward and backward in time for a $(1/2; 3)$ $f^{(\nu)}$ model simulated with 8×10^4 particles using the *CGS* code. In the left panel the ellipticity ratio ϵ and η are plotted ($\epsilon = b/a$, $\eta = c/a$, where $a \geqslant b \geqslant c$ are the axes of the system computed from the inertia tensor), while in the right panel we give the evolution of the x position for one random particle in the simulation. Solid lines represent the evolution forward in time, while dashed ones show the backward evolution. From the plots the typical reversibility time scale is of the order of 6 t_d (from ≈ 8 to 14 t_d).

3.3.3 The Poisson solver

The potential Φ and the mass density ρ are related to each other via the Poisson equation $\nabla^2\Phi = 4\pi G\rho$, where G is the constant of gravitation. In spherical coordinates (r, θ, ϕ) this becomes:

$$\frac{1}{r^2}\frac{\partial}{\partial r}\left(r^2\frac{\partial\Phi}{\partial r}\right) + \frac{1}{r^2 sin\theta}\frac{\partial}{\partial\theta}\left(sin\theta\frac{\partial\Phi}{\partial\theta}\right) + \frac{1}{r^2 sin^2\theta}\frac{\partial^2\Phi}{\partial\phi^2} = 4\pi G\rho. \qquad (3.12)$$

Equation (3.12) can be solved by the method of separation of variables and by expressing the results in terms of spherical harmonics. The expression in spherical harmonics, where P_l^m are the associated Legendre functions of degree l and order m, for the density is given by:

$$\rho(r,\theta,\phi) = \sum_{l=0}^{\infty}\sum_{m=0}^{\infty} P_l^m(cos\theta)\left[A_{lm}(r)cos(m\phi) + B_{lm}(r)sin(m\phi)\right], \qquad (3.13)$$

while the potential Φ can be expressed as:

$$\Phi(r,\theta,\phi) = \sum_{l=0}^{\infty}\sum_{m=0}^{\infty} P_l^m(cos\theta)\left[C_{lm}(r)cos(m\phi) + D_{lm}(r)sin(m\phi)\right]. \quad (3.14)$$

The spherical harmonics $P_l^m(cos\theta)cos(m\phi)$ and $P_l^m(cos\theta)sin(m\phi)$ are a complete set separable with respect to the operator ∇^2, so the Poisson equation (3.12) leads to a second order ordinary linear differential equation for each combination of l and m separately:

$$\frac{d^2C_{lm}(r)}{dr^2} + \frac{2}{r}\frac{C_{lm}(r)}{dr} - \frac{l(l+1)}{r^2}C_{lm}(r) = 4\pi G A_{lm}(r). \quad (3.15)$$

A similar equation can be obtained for D_{lm} by replacing A_{lm} with B_{lm}. The linear equation (3.15) can be solved by the method of variation of parameters, which gives:

$$\begin{aligned} C_{lm}(r) &= c_{1lm}r^{-l-1} + c_{2lm}r^l + \quad (3.16)\\ &-\frac{4\pi G}{2l+1}r^{-l-1}\int_{r_{1lm}}^{r} dss^{l+2}A_{lm}(s) + \frac{4\pi G}{2l+1}r^l\int_{r_{2lm}}^{r} dss^{1-l}A_{lm}(s), \end{aligned}$$

where the integration constants c_{1lm} and c_{2lm} are to be chosen so that the potential is everywhere finite. If we choose $\Phi(\infty) = 0$, the coefficients of the terms with r^l must vanish, that is:

$$c_{2lm} = -\frac{4\pi G}{2l+1}\int_{r_{2lm}}^{\infty} dss^{1-l}A_{lm}(s), \quad (3.17)$$

for all positive l, m. At the origin the potential must be finite, thus the coefficients of the terms with r^{-l-1} must be zero:

$$c_{1lm} = -\frac{4\pi G}{2l+1}\int_{0}^{r_{1lm}} dss^{l+2}A_{lm}(s). \quad (3.18)$$

Inserting these expressions back into Equation (3.16) gives the solution of the differential Equation (3.15):

$$C_{lm}(r) = C_{1lm}(r) + C_{2lm}(r), \quad (3.19)$$

with

$$C_{1lm} = -\frac{4\pi G}{2l+1}r^{-l-1}\int_{0}^{r} dss^{l+2}A_{lm}(s). \quad (3.20)$$

and

$$C_{2lm} = -\frac{4\pi G}{2l+1}r^{l}\int_{r}^{\infty} dss^{1-l}A_{lm}(s). \quad (3.21)$$

The two terms can be seen as the contribution from the mass inside (C_{1lm}) and outside (C_{2lm}) the radius r.

The function $A_{lm}(r)$ is determined from the density distribution $\rho(r, \theta, \phi)$:

$$A_{lm}(r) = \frac{(2l+1)(2-\delta(m))}{4\pi}\frac{(l-m)!}{(l+m)!} \times \int_0^{+\pi} d\theta \sin\theta P_l^m(\cos\theta) \int_{-\pi}^{+\pi} d\phi \cos(m\phi)\rho(r,\theta,\phi), \quad (3.22)$$

with $\delta(l)$ is defined as $\delta(0) = 1$ and $\delta(m) = 0$ if $m \neq 0$. Similarly, B_{lm} is found by replacing $\cos(m\phi)$ by $\sin(m\phi)$ in the equation above.

The acceleration is then computed by taking the relevant partial derivatives of the potential (3.14), soas to obtain the following expressions:

$$a_r(r,\theta,\phi) = -\sum_{l=0}^{\infty}\sum_{m=0}^{l} P_l^m(\cos\theta)\left(E_{lm}(r)\cos(m\phi) + F_{lm}(r)\sin(m\phi)\right), \quad (3.23)$$

$$a_\theta(r,\theta,\phi) = -\sum_{l=0}^{\infty}\sum_{m=0}^{l} \frac{dP_l^m(\cos\theta)}{d\theta}\left(G_{lm}(r)\cos(m\phi) + H_{lm}(r)\sin(m\phi)\right), \quad (3.24)$$

$$a_\phi(r,\theta,\phi) = -\sum_{l=0}^{\infty}\sum_{m=0}^{l} \frac{mP_l^m(\sin\theta)}{\sin\theta}\left(H_{lm}(r)\cos(m\phi) - G_{lm}(r)\sin(m\phi)\right), \quad (3.25)$$

where $G_{lm}(r) = C_{lm}(r)/r$, $H_{lm}(r) = D_{lm}(r)/r$, $E_{lm}(r) = dC_{lm}(r)/dr$, and $F_{lm} = dD_{lm}(r)/dr$.

For the code implementation, the double loop over the spherical harmonics terms is truncated at $l \leqslant 6$. The orthogonality of the Legendre functions ensures (1) good convergence properties for the expansion (assuming physically inspired initial boundary conditions, i.e. finite mass and density) and (2) that there is no mixing between different terms in the expansion.

The density is computed by assigning a particle to the two nearest points in the radial grid with a linear mass assignment kernel, while the angular dependence is treated exactly by formally introducing a delta function in θ and ϕ.

In fact, to evaluate $A_{lm}(r_i)$ the two integrals in Equation (3.22) are transformed in a sum over the particles belonging to the two radial cells closest

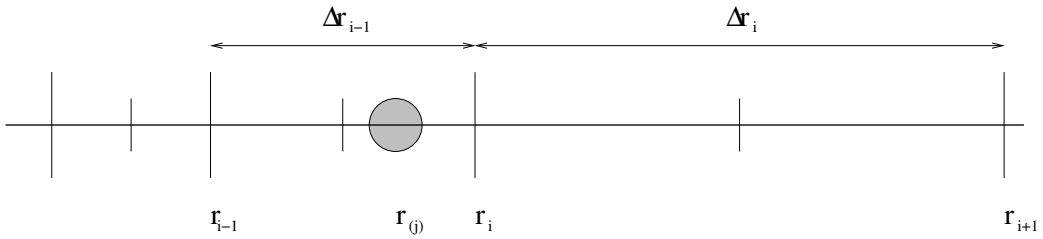

Figure 3.4: Assigning the mass to the grid. The particle at $r_{(j)}$, with mass $m_{(j)}$, contributes to the density at the grid points r_{i-1} and r_i with weight, respectively, $m_{(j)}\ (1-(r_{(j)}-r_{i-1})/\Delta r_{i-1})$, and $m_{(j)}\ (r_{(j)}-r_{i-1})/\Delta r_{i-1}$.

to r_i:

$$A_{lm}(r_i)=\frac{(2l+1)(2-\delta(m))}{4\pi}\frac{(l-m)!}{(l+m)!}\sum_{j\in\{I\}}\sin\theta_{(j)}P_l^m(\cos\theta_{(j)})\cos(m\phi_{(j)})\epsilon(r_{(j)},r_i), \tag{3.26}$$

where the index j runs over the particles, and the set $\{I\}$ is defined by the particles such that $r_i-\Delta r_{i-1}/2<r_{(j)}<r_i+\Delta r_i/2$; $\epsilon(r_{(j)},r_i)$ is a weight function defined by the mass assignment kernel. If $r_{(j)}>r_i$:

$$\epsilon(r_{(j)},r_i)=1-\frac{r_{(j)}-r_i}{\Delta r_i}, \tag{3.27}$$

or else, if $r_{(j)}<r_i$:

$$\epsilon(r_{(j)},r_i)=\frac{r_{(j)}-r_{i-1}}{\Delta r_{i-1}}. \tag{3.28}$$

The force is then assigned from the grid points to the particles using the same kernel $\epsilon(r_{(j)},r_i)$.

We note that the linear kernel to assign the mass to the grid (and the force on the particles) still introduces a very small systematic radial force, because of the linear interpolation on the radial grid. We partially correct for this small error by computing and subtracting the self force of the particle on itself. However the use of the interpolation for the force assignment has an intrinsic limitation since the computed force is not exactly the gradient of the potential. Some consequences on the conservation of energy are discussed in Sect. 3.4.

As shown in Sect. 3.4.2, the numerical scheme does not introduce any unphysical preferred spatial direction for the N-body system.

The expansions require special attention near the z axis, because some factors in Equations (3.23) and (3.25) lead, if evaluated numerically, to indefinite expressions of the form $0/0$. In reality, only the terms with $m=0$ and

$m = 1$ remain. We have studied the numerical behavior near the z axis in the limits $\theta \to 0$ and $\theta \to \pi$. The actual computation of the force is currently done by introducing a cutoff in the θ angle near the axis. The threshold value has been chosen to ensure that the relative error introduced in the force is less than 10^{-5}.

The radial integration required in Equations (3.20-3.21) to obtain $C_{1lm}(r_i)$ and $C_{2lm}(r_i)$ is carried out by assuming $A_{lm}(r)$ to be constant over a cell so that it can be taken out of the integral, which is then computed analytically for each cell.

3.3.4 Performance

From the structure of the CGS code, the computational time per time step is expected to scale linearly with respect to the number of the particles used. Another important parameter is the number of terms in the spherical harmonic expansion, for which the scaling of the computational time is linear for some subroutines, while others require resources that are approximately independent of it. Thus the global dependence from the number of spherical harmonics used is somewhat less than linear, as can be seen from Table 3.1. The number of grid points has little effect on the total CPU time. We have empirically checked the expected dependence by running several simulations summarized in Table 3.1. These offer a benchmark for the performance of the code.

In order to study the work load in the different subroutines we have performed a *profiling* of the code by using the standard Linux package *gprof*. The results are summarized in Table 3.2 for a typical run with spherical harmonics terms up to $l = 4$ that follows for 10^3 steps the evolution of 10^5 particles using a radial grid with 10^2 points and calling the diagnostic subroutines every 10^2 steps. Most of the computational time is spent to compute the potential ($\approx 41\%$) and the acceleration of the particles ($\approx 52\%$). Only 4% of the CPU time is used to advance the particles with the leap-frog scheme, while the diagnostic performed on the flight requires around 2% of the computational resources. The remaining time is spent by initialization subroutines, in particular for the computation of the small self-force and self-potential energy induced by each particle on itself corrected during the run.

Table 3.1: Typical performance of the *CGS* code with different parameters. l is the highest order of spherical harmonics used, N_g is the number of grid points, N_{steps} the number of time steps, N the number of particles, t_{run} is the CPU time in seconds required to complete the simulation as measured with *gprof* on a Pentium4 1.7 GHz workstation. The diagnostic subroutines were called every 10^2 time steps.

l	N_g	N_{step}	N	t_{run}
0	100	10^3	10^5	181
2	100	10^3	10^5	353
4	100	10^3	10^5	607
6	100	10^3	10^5	970
4	100	10^3	5×10^4	311
4	100	10^3	2.5×10^4	158
4	60	10^3	2.5×10^4	147
4	150	10^3	2.5×10^4	190
4	120	10^3	8×10^5	4869

3.4 Tests

The code has been tested extensively in order to verify its accuracy in conserving the global integrals (total energy, total angular and linear momentum) for equilibrium and non-equilibrium initial conditions, and the single-particle energy and angular momentum for runs starting from spherically symmetric equilibrium models (Plummer and some stable $f^{(\nu)}$ models).

3.4.1 Conservation of the global integrals

We studied first the code performance by simulating a Plummer distribution, which is known to be stable analytically. As expected, there is no evolution for the fractional mass radii and the code conserves the central density accurately.

The typical relative energy conservation for a run with 10^5 particles initialised with a Plummer model is of the order of 10^{-5} per dynamical time. The angular momentum is also conserved well, at the same relative level of the energy; to appreciate the accuracy in the relative angular momentum conservation we recall that since we are considering non rotating configurations, the system possesses a very small initial angular momentum $\lambda \approx 10^{-3} - 10^{-4}$ (where $\lambda = J|E|^{1/2}/(GM^{5/2})$).

Table 3.2: Profiling for a simulation that followed the evolution of 10^5 particles for 10^3 steps using $l \leqslant 4$, a radial grid with 10^2 points and calling the diagnostic subroutines every 10^2 steps. The first column gives the fractional time spent in the subroutine identified by its *Name* (last column), the second column the cumulative time t_{cum}, the third the time t spent in that subroutine, and the fourth column the number of calls to that subroutine. Most of the time is used to solve the Poisson equation and to compute the acceleration, including the evaluation of the Legendre polynomials for each particle (plg_acc and plg_pot).

$\%t$	t_{cum}	t	N_{calls}	Name
38.86	235.70	235.70	1000	accel (self)
33.48	438.79	203.09	1002	poisson (self)
13.51	520.74	81.95	1.013×10^8	plg_acc
6.98	563.10	42.36	1.002×10^8	plg_pot
3.87	586.59	23.49	10^8	advpart
1.55	596.01	9.42	12	diagnostic
1.18	603.17	7.16	1	sfer
0.36	605.34	2.17	1003	p2g
0.05	605.63	0.29	1673843	ran2
0.04	605.89	0.26	12	veldis
0.03	606.09	0.20	12	veldisbound
0.03	606.29	0.20	1	init_vel
0.02	606.39	0.10	1	plummer
0.01	606.48	0.09	12	densbound
0.01	606.56	0.08	13	dens
0.00	606.58	0.02	1	rotate

We note that in Fig. 3.5 the relative energy errors (left panel) show a pattern that has variations at a higher frequency than that of the errors of the relative angular momentum (right panel). The frequency of the noise is approximately of the order of the mean cell-crossing frequency, so it may be associated to the Poisson noise of the occupation number of the radial grid (this is in fact the major source of errors in the total energy for stationary configurations). The leading source of errors in the angular momentum conservation seems to be, on the other side, related to errors in the integration of individual orbits, and thus the frequency of the variations in J is of the order of the dynamical frequency (i.e. $\approx 1/t_d$).

The code also conserves the linear momentum well (see Fig. 3.11). In fact, the velocity of the centre of mass presents usually a pattern compatible with random walk. However, in particular configurations, such as in simulations of violent collapse, noise fluctuations or fast travelling particles in the halo can move the centre of mass of the bound system outside the first radial cell. In this case the code may lose accuracy, because the centre of mass of the bound particles and the centre for the spherical harmonic expansion no longer coincide, and only a finite number of spherical harmonics is considered. To avoid this problem, it is sufficient to re-centre the centre of mass of the bound system at the origin of the coordinate system a few times every t_d.

We then checked the general conservation performance for a run initialised with a $(1;5)$ $f^{(\nu)}$ model (see Fig. 3.7). This choice seems to be particularly interesting, not only because it presents a significant global content of kinetic energy in the radial degree of freedom ($2K_r/K_T \approx 1.6$), although still in the stable range of the sequence, but also because such model is more concentrated than the Plummer model.

Extremely concentrated models are harder to simulate. As an example, we report some results obtained in simulating a $f^{(\nu)}$ $(1/2;9.4)$ model, which is $\approx 3\times10^3$ times more concentrated as the $(1;5)$ model. The density contrast is $\rho(0)/\rho(r_M) \approx 1.15\times10^5$. Here the total energy conservation is still around 10^{-5} per dynamical time for 10^6 particles (see Fig. 3.10) and there are no signs of evolution, e.g. the radii containing 50 and 100 particles (in fraction of total mass 5×10^{-5} and 10^{-4}) are only fluctuating within the Poisson noise.

After some tests we concluded that the optimal choice of grid size appears to be the one that ensures approximately at least 10^3 particles in every radial cell, except at the centre, where smaller numbers can be tolerated in order to increase the spatial resolution.

The time step does not play an important role in the conservation of the global integrals, as long as there are at least a few hundreds steps per dynamical time.

The overall results are thus successful, except for a remaining open issue, namely the effects induced by the interpolation over the radial grid, which depends on the radial positions and thus on the properties of the mass distribution. In fact there is no guarantee that the interpolated force be exactly the gradient of the potential. While this has negligible consequences in stationary configurations, it may lead to undesired effects on energy conservation in strongly non-stationary conditions, such as the simulations of violent collapse starting with $2K/|W| \lesssim 0.05$. In fact, under those conditions there can be a relative error in energy conservation up to 10^{-2} between the initial time and the time at which the virial equilibrium has been reached. This error is almost independent from the number of particles used. After reaching equi-

librium the typical relative error in energy returns to be of the order of 10^{-5} over one dynamical time for 10^5 particles.

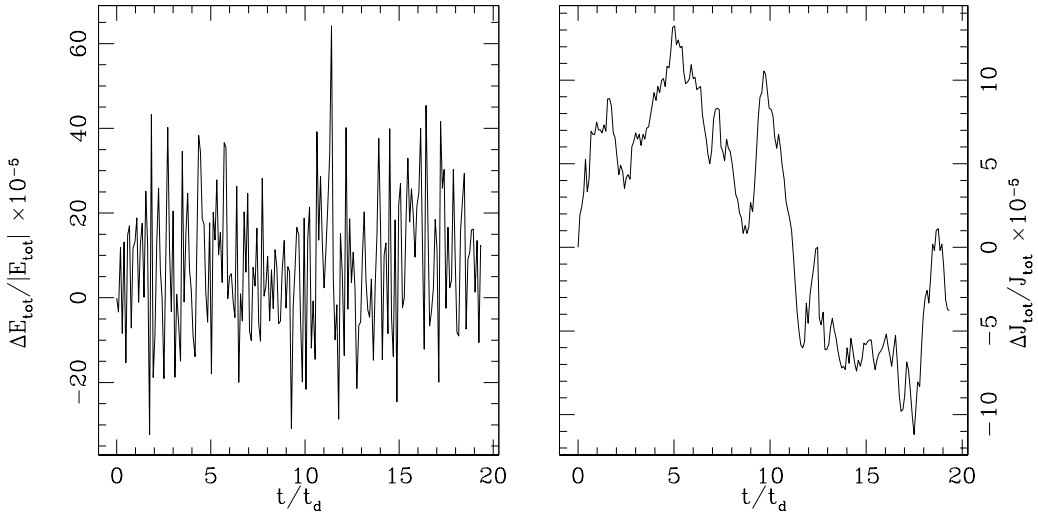

Figure 3.5: Total energy (left panel) and total angular momentum conservation (right panel) for a simulated Plummer model with 2×10^4 particles using the *CGS* code. The time is given in units of dynamical time t_d. Note that the absolute value of the total angular momentum associated with the initial conditions is rather low, the dimensionless rotation parameter λ is $\approx 2 \times 10^{-3}$.

3.4.2 Rotational invariance

We have tested the rotational invariance of the code by performing some simulations, both with non zero and nearly zero angular momentum, which we have then repeated after rotating the initial conditions by an arbitrary angle. The evolution of the system appears to be not influenced by the existence of any spurious preferred spatial direction. The macroscopic properties of the simulation with rotated initial conditions are the same as the original one.

Furthermore, for the inertia tensor $T_{ij} = \sum_{k=1}^{N} m_{(k)} x_{(k)i} x_{(k)j}$, the operations of rotation and time evolution commute. For example, this can be seen in Fig. 3.12 for a simulation where the system loses the initial spherical symmetry as the result of the radial orbit instability.

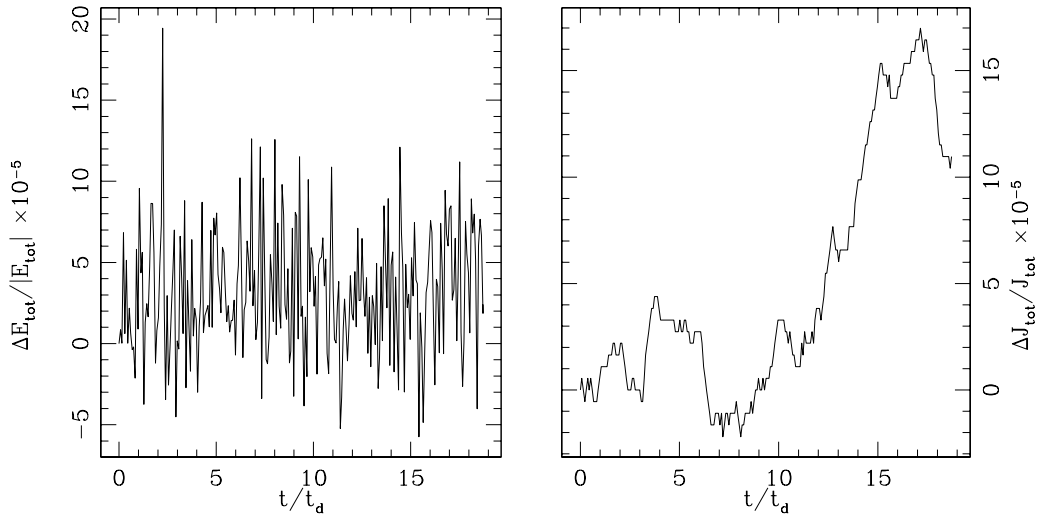

Figure 3.6: Total energy (left panel) and total angular momentum conservation (right panel) for a simulated Plummer model with 2×10^5 particles using the *CGS* code. Higher resolution version of Fig. 3.5; here $\lambda \approx 4 \times 10^{-4}$.

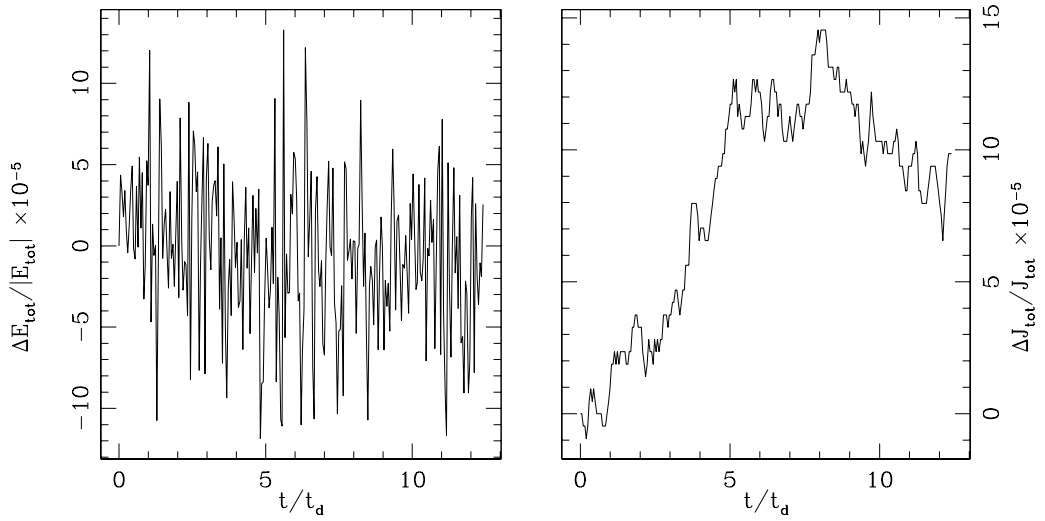

Figure 3.7: Total energy (left panel) and total angular momentum conservation (right panel) for a simulated stable $(1;5)$ $f^{(\nu)}$ model with 2×10^5 particles using the *CGS* code. Here $\lambda \approx 4 \times 10^{-4}$.

3.4.3 Diffusion in the (E, J) phase space

To obtain a picture of the behavior of the code with respect to the phase space, we checked the conservation of single-particle energy and angular mo-

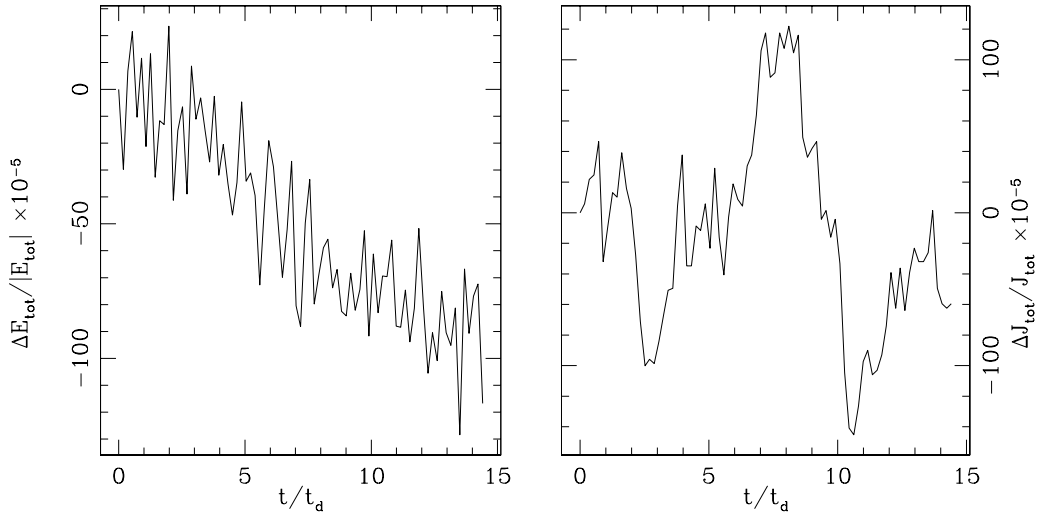

Figure 3.8: Total energy (left panel) and total angular momentum conservation (right panel) for a simulated $(1/2; 3)$ $f^{(\nu)}$ model with 2×10^4 particles using the *CGS* code. The time is given in units of dynamical time t_d. Note that the absolute value of the total angular momentum associated with the initial conditions is very low, as implies a dimensionless rotation parameter $\lambda \approx 10^{-4}$. As discussed in Sect. 4.2 this model is strongly affected by the radial orbit instability and in a short time (of order t_d) the excess of radial kinetic energy is transferred to the tangential degree of freedom with a consequent evolution toward a flattened configuration.

mentum. In fact, for a spherical, time-independent potential, these quantities should be conserved exactly. In reality, finite accuracy and the finite number of particles will generate a diffusion in phase space.

For a Plummer model with 4×10^5 particles after 5 dynamical times the mean square variation of single-particle energy is within 4×10^{-3} times the maximum binding energy of the system; this number increases to 8×10^{-3} after 20 t_d. Similar numbers hold for the angular momentum: the mean square variation for each component is of the order of 3×10^{-3} times the value of the maximum single particle angular momentum after 5 t_d and 10^{-2} after 20 t_d (see also the discussion in Sect. 3.5 and Figs. 3.13-3.14).

Also for a $(1, 5)$ $f^{(\nu)}$ model the conservations at the level of phase space are very good (see Fig. 3.15).

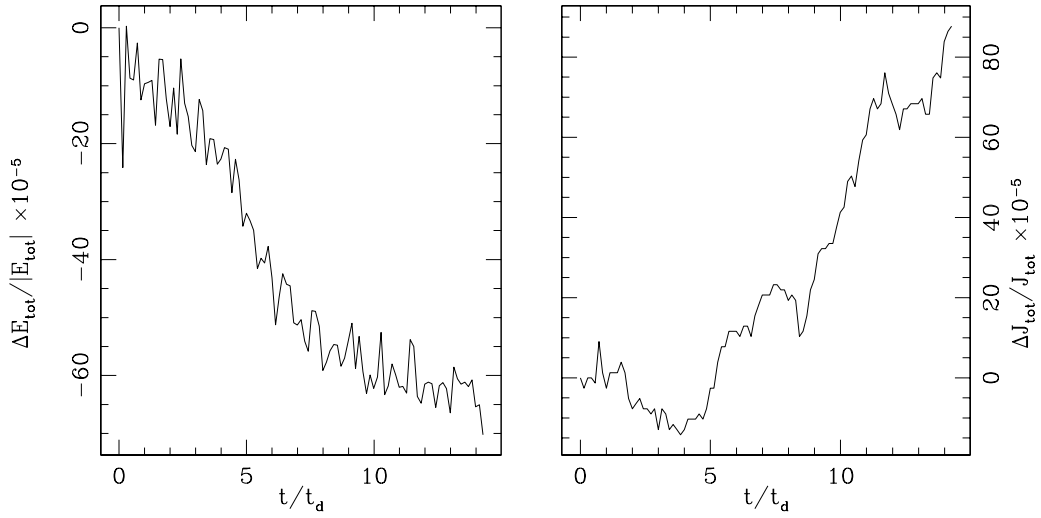

Figure 3.9: Total energy (left panel) and total angular momentum conservation (right panel) for a simulated $(1/2; 3)$ $f^{(\nu)}$ model with 2×10^5 particles using the *CGS* code. Higher resolution version of Fig. 3.5; here $\lambda \approx 1.5 \times 10^{-4}$.

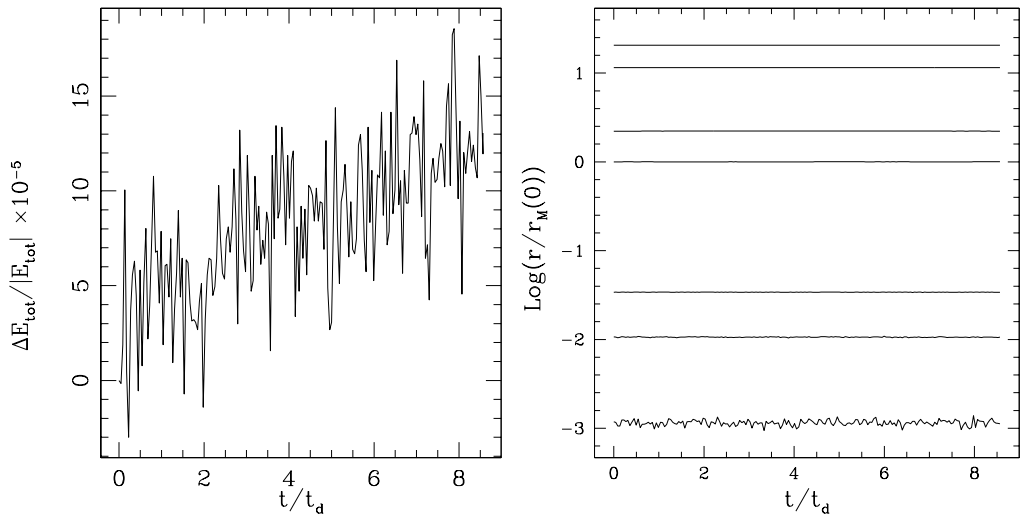

Figure 3.10: Total energy conservation (left panel) and selected Lagrangian radii (right panel; enclosing a fractional mass equal to $10^{-4}; 6.25 \times 10^{-3}; 5 \times 10^{-2}; 0.5; 0.7; 0.95; 0.98$) for a simulated stable $(1/2; 9.4)$ $f^{(\nu)}$ model with 10^6 particles using the *CGS* code.

3.5 Comparison with SCFM (Hernquist & Ostriker 1992)

In the Self Consistent Field Method (Hernquist & Ostriker 1992), the expansion of the density and the potential in a suitable basis is complete, and thus

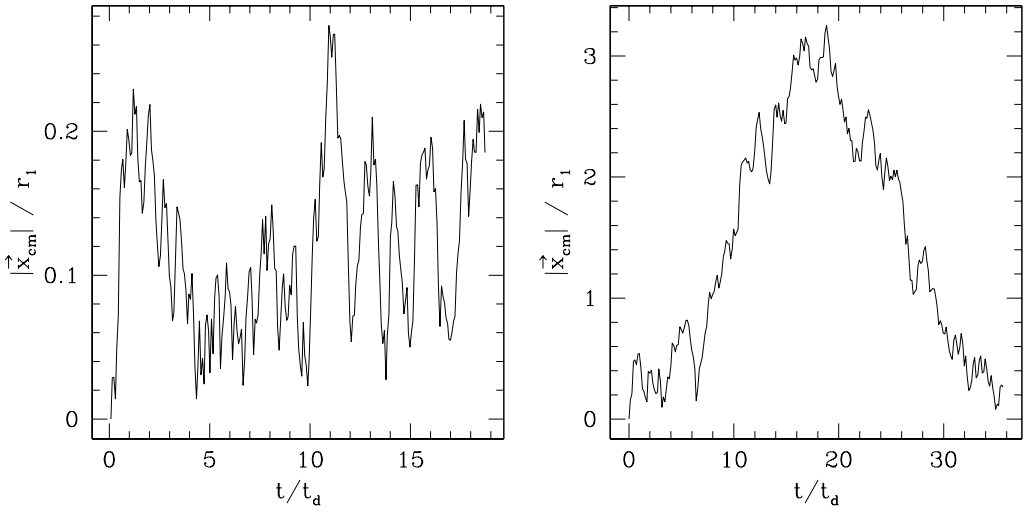

Figure 3.11: Total linear momentum conservation for stationary (left panel) and non stationary (right panel) configurations with with 2×10^5 particles using the *CGS* code: position of the center of mass divided by the size of the first radial grid for a simulated Plummer model (left panel) and for a simulated unstable $(1/2; 3)$ $f^{(\nu)}$ model (right panel). The size of the first radial grid is 0.03 r_M for the Plummer model and 0.01 r_M for the $f^{(\nu)}$ model (more concentrated and thus with a smaller radius for the first cell). The time is given in units of dynamical time t_d.

a radial basis in terms of a set of density-potential functions is chosen to be combined with the spherical harmonics.

In the *SCFM* approach the choice of radial functions able to capture the large scale structure of the system to be simulated is of fundamental importance. In fact, even if in principle the expansion converges for every density profile provided that the basis for the expansion is complete, from the numerical point of view it is important to be able to truncate the expansion at the lowest possible order. To construct a suitable complete set of radial functions Hernquist & Ostriker (1992) resort to a density potential pair that has the form:

$$\rho(r) = \frac{M}{2\pi}\frac{a}{r}\frac{1}{(r+a)^3}, \tag{3.29}$$

$$\Phi(r) = -G\frac{M}{r+a}, \tag{3.30}$$

as zero order member. The density profile in Equation (3.29) gives a good fit to the $R^{1/4}$ law if projected, and thus is a good choice for simulations aimed

```
------------------------------------------------------------
              Tij                      Ry^{-1} TimeEv Ry (Tij)

Time = 0

 0.199056  0.000592  0.000093     0.199056  0.000592  0.000093
 0.000592  0.199844  0.000591     0.000592  0.199844  0.000591
 0.000093  0.000591  0.199073     0.000093  0.000591  0.199073

Time = 15 td

 0.168254  0.025679 -0.029320     0.168383  0.025798 -0.029316
 0.025679  0.214134  0.013725     0.025798  0.214202  0.013792
-0.029320  0.013725  0.209690    -0.029316  0.013792  0.209763

Time = 30 td

 0.174024  0.026087 -0.025396     0.174830  0.025598 -0.025499
 0.026087  0.215086  0.012943     0.025598  0.213986  0.013301
-0.025396  0.012943  0.215150    -0.025499  0.013301  0.212986

------------------------------------------------------------
```

Figure 3.12: Evolution of the inertia tensor T_{ij} for a simulation starting from unstable initial conditions (the $f^{(\nu)}$ model $(3/4; 3)$) with 8×10^4 particles (left set of three columns). To test the rotational invariance of the code we re-run the simulation with the same initial conditions rotated by $\pi/2$ along the y axis. Then we rotate by $-\pi/2$ along the same axis the resulting inertia tensor (right column), which we compare to the one from the original simulation. The agreement is very good, better than 99% after 30 dynamical times.

at studying the dynamics of elliptical galaxies (see Hernquist 1990).

The associated basis is then defined as follows:

$$\rho_{nlm}(\vec{r}) = \frac{K_{nl}}{2\pi}\frac{r^l}{r(1+r)^{2l+3}}W_{nl}(\xi)\sqrt{4\pi}Y_{lm}(\theta,\phi), \quad (3.31)$$

$$\Phi_{nlm}(\vec{r}) = -\frac{r^l}{(1+r)^{2l+1}}W_{nl}(\xi)\sqrt{4\pi}Y_{lm}(\theta,\phi), \quad (3.32)$$

where K_{nl} are normalization constants and the functions $W_{nl}(\xi)$ give the higher order elements of the basis, with $\xi = \xi(r)$. The precise form of the functions $W_{nl}(\xi(r))$ is given by Hernquist & Ostriker (1992). Here it is sufficient to remember that the potential and the density can be eventually expressed as:

$$\rho(r,\theta,\phi) = \sum_{l=0}^{\infty}\sum_{m=0}^{\infty} P_l^m(cos\theta)\,[A_{lm}(r)cos(m\phi) + B_{lm}(r)sin(m\phi)] \quad (3.33)$$

$$\Phi(r,\theta,\phi) = \sum_{l=0}^{\infty}\sum_{m=0}^{\infty} P_l^m(cos\theta)\,[C_{lm}(r)cos(m\phi) + D_{lm}(r)sin(m\phi)] \quad (3.34)$$

which are similar to the Equations (3.13-3.14) that we have derived for the *CGS* code, with the difference that here the coefficients A_{lm}, B_{lm}, C_{lm} and D_{lm} are computed using the expansion in Equations (3.31-3.32).

Apart from this point, the structure of the self-consistent field method is essentially the same as in our code, since it employs a global time step and particles are advanced with a leap-frog scheme.

In our approach we have traded some accuracy (the *SCFM* is claimed to conserve *exactly* the total energy and the total angular momentum) for a greater flexibility in the range of density profiles that the code is able to handle efficiently.

To assess the performance of our code we have run some comparison simulations using both the *CGS* code and the *SCFM* (within the *NEMO* distribution; Teuben 1995) with the aim to quantify in particular the relaxation effects. In practice we have replicated the experiments done by Hernquist & Ostriker (1992) (see Sect. 5.3 of their paper), which measure the scatter in the single particle energy and angular momenta for stable configurations. Some representative results are reported in the set of Figs. 3.13-3.14. The measured diffusion in phase space is lower for the *SCFM*, but only slightly: the relative difference between the two codes is of the order 10%.

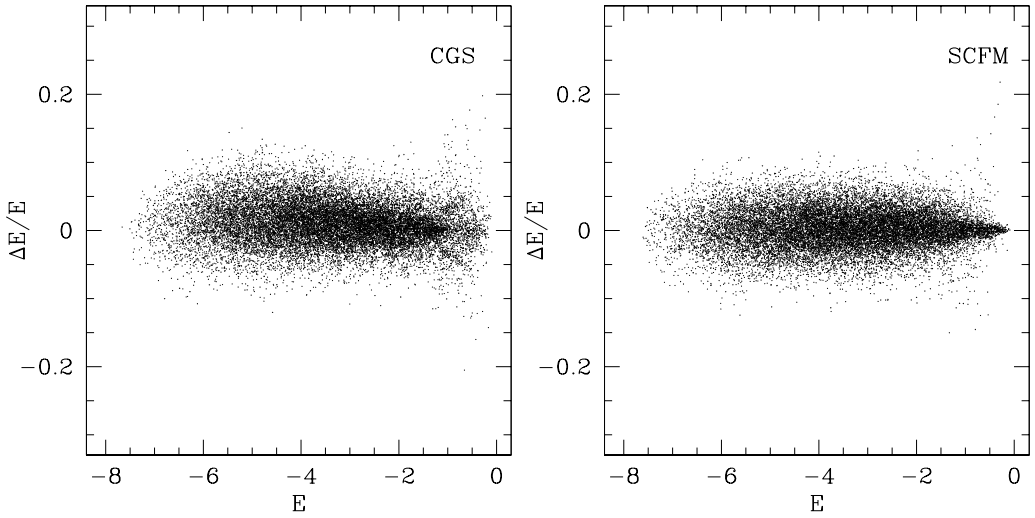

Figure 3.13: Changes the energy of individual particles in a Plummer model between 4 and 8 t_d as a function of the single-particle energy per unit mass at time 4 t_d. Energy differences are measured relative to the energy value at $t = 4\,t_d$. A total of 2×10^4 particles were used, with a time step $\Delta t = 0.002\,t_d$. The left panel refers to a simulation performed with the *CGS* code, while the right one with the *SCFM* method by Hernquist & Ostriker (1992). The single particle energy diffusion in the two codes is at the same level: the measured mean absolute deviation $\langle|\Delta E/E|\rangle$ is 0.026 for the *CGS* code and 0.022 for the *SCFM*.

3.6 Comparison with GyrFalcON (Dehnen 2000)

As a further test, we have also run a few test simulations by comparing, under identical conditions, the performance of our code to that of the fast tree code *GyrFalcON* (Dehnen 2000, 2002), within the *NEMO* distribution (Teuben 1995). In such tests, we adopt the following procedure. We first generate the initial conditions in the physical units used by our code (see Sect. 6.2) and we run the simulation. We then convert the initial conditions to the natural units defined by Heggie & Mathieu (1986) and used in Dehnen's code. Finally, we run the simulation within the *NEMO* environment. The quality of the integration is checked with the standard *NEMO* tools of analysis. At the end of the simulation, a "snapshot" of the system is exported and converted back to our units, in such a way that it can be processed by the same diagnostics used for the particle-mesh code.

The initial conditions for these runs have been chosen in order to be representative of the sample investigated for the study of the formation of

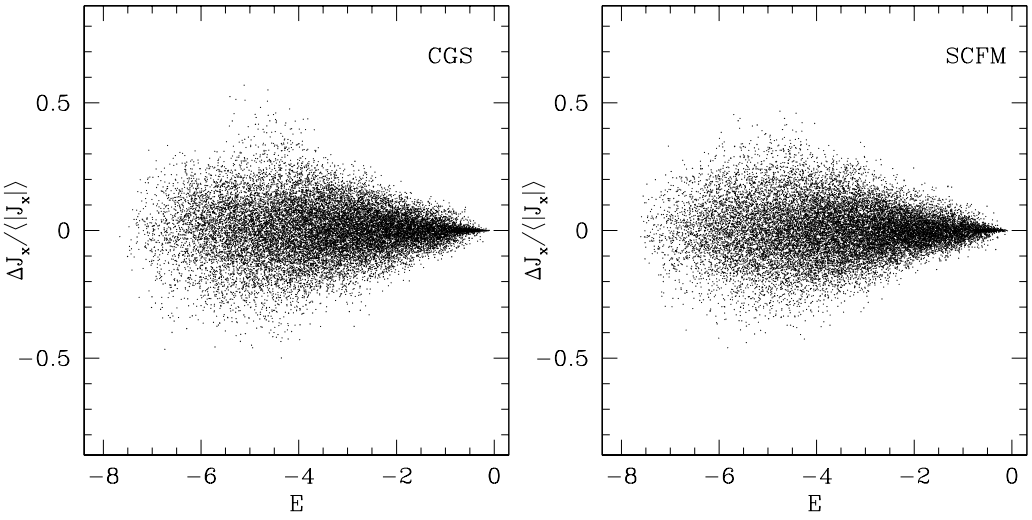

Figure 3.14: Changes in the x component of the angular momentum of individual particles in a Plummer model between 4 and 8 t_d as a function of the energy per unit mass at time 4 t_d. Angular momentum differences are measured relative to $t = 4\ t_d$. A total of 2×10^4 particles were used, with a time step $\Delta t = 0.002\ t_d$. The left panel refers to a simulation performed with the *CGS* code, while the right one with the *SCFM* method by Hernquist & Ostriker (1992). The single particle angular momentum diffusion in the two codes is at the same level: the measured mean absolute deviation $\langle|\Delta J_x|\rangle/\langle|J_x|\rangle$ is 0.080 for the *CGS* code and 0.076 for the *SCFM*.

partially relaxed stellar systems via collisionless collapse; they are described in Table 6.1 ($C4.1$ and $C4.3$ entries), with the properties of the final equilibrium state listed in Table 6.3.

For the runs with Dehnen's tree code we adopted the following choice of integration parameters: tolerance parameter $\theta = 0.5$ (standard choice 0.6) to improve accuracy in the calculation of forces; softening length $\epsilon = 0.01$ (in natural units; standard choice 0.05) to increase central resolution; minimum allowed time step $1/2^8$ (i.e. ≈ 724 steps per dynamical time). With this choice of integration parameters, the energy and angular momentum conservation is very good: in one dynamical time t_d, the relative changes are $\Delta E_{\rm tot}/E_{\rm tot} < 10^{-5}$ and $\Delta J_{\rm tot}/J_{\rm tot} < 10^{-4}$.

The required CPU time to complete the simulation with GyrFalcON is only marginally higher than with our code, which, however, has not yet been optimized for speed.

As desired, for these runs we find a substantial similarity in the properties of the end-products obtained by the two different methods of integration

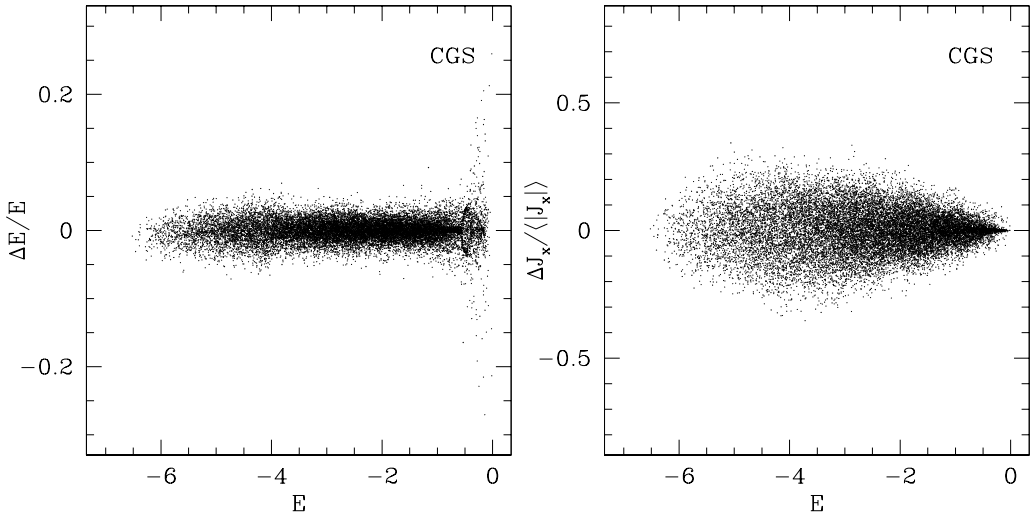

Figure 3.15: Changes in the binding energy (left panel) and in the x component of angular momentum of individual particles in a $(1;5)$ $f^{(\nu)}$ model between 2 and 6 t_d as a function of the binding energy per unit mass at time 2 t_d. A total of 2×10^5 particles were used for the simulation with our *CGS* code, with a time step $\Delta t = 0.002\ t_d$. The measured mean absolute deviation are $\langle|\Delta E/E|\rangle = 0.012$ and $\langle|\Delta J_x|\rangle/\langle|J_x|\rangle = 0.047$.

(see Fig. 3.16). To be sure, small differences naturally arise, as expected. The main systematic difference is in the degree of pressure anisotropy characterizing the end-products of the simulations. In fact, the output from the tree code is slightly more isotropic: the final global anisotropy, measured by $2K_r/K_T$, is up to 7% lower, with a slight outward shift of the pressure anisotropy profile $\alpha(r)$, corresponding to a more efficient core relaxation.

3.7 Diagnostics

N-body simulations are important tools to investigate the dynamical evolution of gravitational structures and can provide a unique insight in the detailed phase space structure of self-gravitating systems. In fact, in the *observations* of these systems, photometric and spectroscopic data points sample only limited spatial regions with finite accuracy, projected on the plane of sky.

The numerical simulations thus play the role of laboratory experiments, providing extremely detailed information (in principle the positions and the velocities of all the particles at every time step). These quantities may be directly stored and analysed later, or the data-processing may be performed

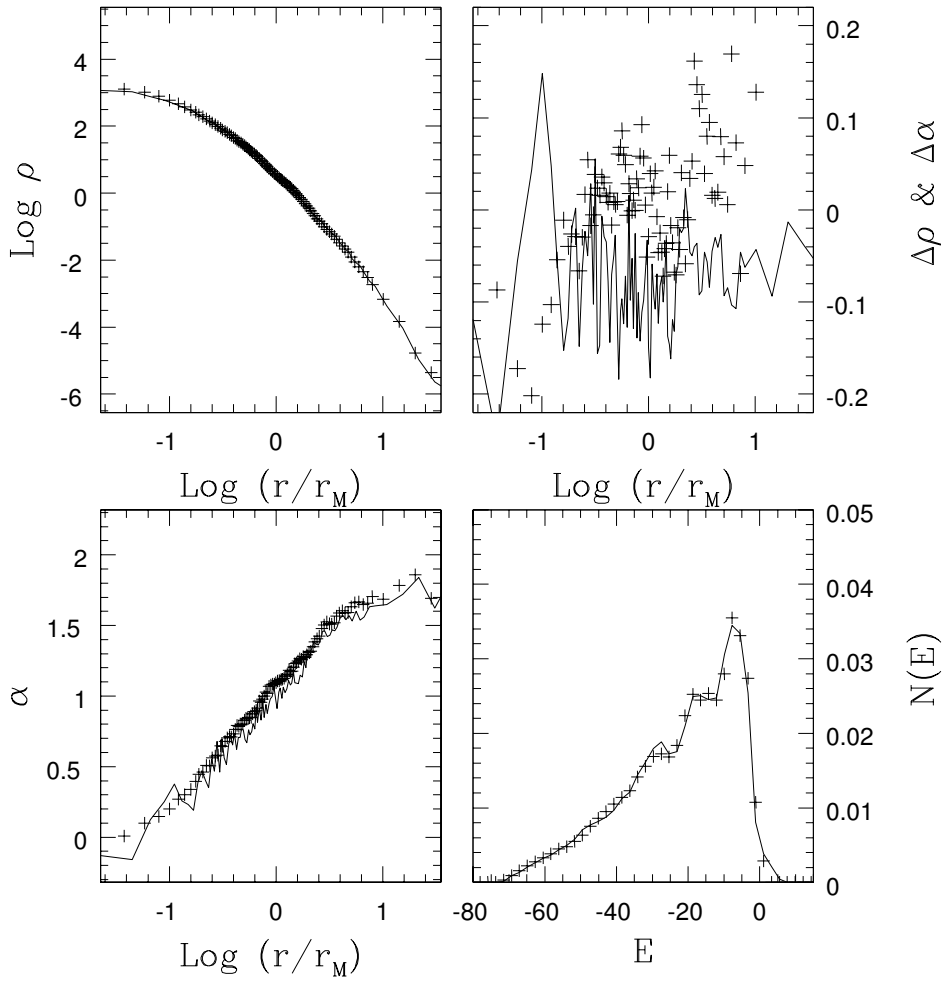

Figure 3.16: Comparison between our code and *GyrFalcON* (Dehnen 2000) for a collisionless collapse simulation (run $C4.1$ in Chapter 6). Final density (upper left) and pressure anisotropy (bottom left) profiles, and single-particle energy distribution (bottom right) for a run starting from 10^5 particles in 10 cold clumps with $u = 0.15$ (see Tables 6.1 and 6.3 for further details about the simulation); here the solid lines give the results obtained with *GyrFalcON*, while the crosses refer to our code. In the upper right panel we plot the differences in the density profile $\Delta\rho = 2(\rho_{falcon} - \rho_{CGS})/(\rho_{falcon} + \rho_{CGS})$ (crosses) and in the pressure anisotropy profile $\Delta\alpha = \alpha_{falcon} - \alpha_{CGS}$ (solid line).

in real-time, i.e. while the simulation is running, to reduce the amount of data stored.

In the *CGS* code an extensive set of processed diagnostic quantities is provided; in addition, we save a complete snapshot of the N-body system every few dynamical times. This snapshot can be used either as a restart file or to further analyse the simulation.
As diagnostic our code provides the following quantities in fuction of time:

- The total energy E_{tot}, the virial ratio $2K/|W|$, the total angular momentum $|J_{tot}|$ in the standard output file *fort.20*;

- The single components of the angular momentum vector J_x, J_y, J_z and the mean orbital ellipticity $\langle e \rangle = (1/N) \sum_{i=1,N} 2E_{(i)} J^2_{(i)} / (\Phi^2(r_{(i)}) r^2_{(i)})$ in the standard output file *fort.19*;

- The density profile $\rho(r)$, estimated with the radial grid used to solve the Poisson equation in the standard output file *fort.18*;

- The ellipticity ratios $\kappa = b/a$ and $\eta = c/a$, where $c \leqslant b \leqslant a$ and a, b, c are the semiaxes of the system estimated from the inertia tensor, in the standard output file *fort.17*;

- The complete inertia tensor in the standard output file *fort.16*;

- The radial (K_r) and tangential (K_T) kinetic energy and their ratio $2K_r/K_T$ in the standard output file *fort.14*;

- The pressure anisotropy profile $\alpha(r)$, estimated with the radial grid used to solve the Poisson equation in the standard output file *fort.13*;

- Selected Lagrangian radii in the standard output files *fort.11* and *fort.12*;

- The single-particle energy distribution $N(E)$ (normalised as $M_{tot} = \int N(E) dE$) in the standard output file *fort.22*. This quantity is computed using a binning method over a grid in E;

- The single-particle energy angular momentum distribution $N(E, J)$ (normalised as $M_{tot} = \int N(E, J^2) dE dJ^2$) in the standard output file *fort.23*. This quantity is computed using a binning method over a grid in (E, J^2);

In addition, a summary with the most important quantities selected from the list above is provided in the standard output file *fort.2*.

3.8 Reconstructing the underlying distribution function from the products of N-body simulations

In a simulation of a collisionless N-body system a fundamental diagnostic quantity is the distribution function $f(\vec{x};\vec{w},t)$ (see Equation 3.1). If f is known, all the mean properties (e.g. density and anisotropy profile, line of sight velocity dispersion profiles) of the N-body system can be readily computed.

A direct measure of f in the six-dimensional phase space is not easy, although recently there is a growing interest on this topic in the field of cosmological simulations (see, e.g. Ascasibar & Binney 2004; Williams et al. 2005).

So, instead of working in the six-dimensional $(\vec{x},\vec{w})$ space, we introduce the assumptions of spherical simmetry and approximate dynamical equilibrium with the goal of simplifying the measure of the phase space density. In this case, if the system is also isotropic, the distribution function will depend only from the single particle energy $E = w^2/2 + \Phi(r)$, and thus the complexity of the problem has been greatly reduced since we have to measure the one dimensional phase space density $N(E)$, normalised as

$$M_{tot} = \int N(E) dE. \tag{3.35}$$

The distribution function $f(E)$ (with $M_{tot} = \int f(E) d^3\vec{x} d^3\vec{w}$) will be obtained from $N(E)$ by considering the Jacobian factor associated to the transformation from E to $(\vec{x},\vec{w})$ (see Equation 3.46).

Below we illustrate our method, starting from the reconstruction of the potential well under the assumption of spherical symmetry.

For the main purpose of this Thesis, i.e. for the comparison between the $f^{(\nu)}$ family of models and the end-products of simulations starting from cold initial conditions, we have to dismiss the assumption of isotropy. Thus we consider (see Sect. 6.6.4) the bi-dimensional (E, J^2) phase space. In this case the measure of $N(E, J^2)$ is a straightforward generalisation of the isotropic case, but we have not yet developed a reliable method to compute the conversion factor Ω_r from $N(E, J^2)$ to $f(E, J^2)$ (i.e., $f(E, J^2) = N(E, J^2)/\Omega_r(E, J^2)$; see Sect. 3.8.3). In Sect. 6.6.4 we will thus compare the end-products of the simulations and the $f^{(\nu)}$ models at the level of $N(E, J^2)$ rather than $f(E, J^2)$.

3.8.1 Potential well reconstruction

To define the single particle energy $E = w^2/2 + \Phi(r)$ we need to construct an estimator for the potential $\Phi(r)$. In principle, to compute the potential one may resort to a subroutine borrowed from a N-body code, such as our *CGS* code. This way may be natural when the single particle energy E is defined within a simulation, and thus $\Phi(r)$ has been already computed. However the so obtained potential depends from the specific N-body code used and in general is not spherically symmetric.

Thus, if we are interested in the estimation of the distribution function under the assumption of spherical symmetry, we find more appropriate to define a consistent method to compute the potential $\Phi(r)$. The particles are thus treated as infinitely thin spherical shells, except in the central regions where a softening kernel is introduced to avoid unbound errors near the centre.

In a continuum system with a spherically symmetric mass distribution $M(r)$, where the symbol indicates the mass M enclosed in a sphere of radius r, the potential can be expressed as:

$$\Phi(r) = -G\frac{M(r)}{r} - G\int_r^\infty \frac{dM(r')}{r'}, \tag{3.36}$$

which becomes, in terms of a discrete system made of infinitely thin shells, each of mass $m_{(j)}$:

$$\Phi(r) = -G\frac{M(r)}{r} - G\sum_{j\in\{j|r_{(j)}>r\}} \frac{m_{(j)}}{r_{(j)}}. \tag{3.37}$$

In Equation (3.37) the mass $M(r)$ within the radius r contributes to the potential as if it were all concentrated in the centre, while the outer shells contribute with their own radius $r_{(j)}$. The potential obtained from Equation (3.37) is thus constant within the innermost shell and "piecewise Kepler" between two shells.

By introduction of the quantity $s_{(j)}$, defined as:

$$s_{(j)} = Max(r, r_{(j)}), \tag{3.38}$$

Equation (3.37) becomes:

$$\Phi(r) = -G\sum_{j=1}^{N} m_{(j)}/s_{(j)}. \tag{3.39}$$

A softening kernel can thus be naturally introduced in terms of $s_{(j)}$ in Equation (3.39). If we consider the K_0 kernel (Dehnen 2001, App. B), acting over a softening length ϵ:

$$\begin{aligned} K_0(r) &= \frac{1}{\epsilon}\left\{1+\frac{1}{2}\left[1-\left(\frac{r}{\epsilon}\right)^2\right]+\frac{21}{16}\left[1-\left(\frac{r}{\epsilon}\right)^2\right]^2\right\} \; If\ r<\epsilon \\ K_0(r) &= \frac{1}{r} \qquad\qquad If\ r>\epsilon, \end{aligned} \tag{3.40}$$

then we can rewrite Equation (3.39) as:

$$\Phi(r) = -G\sum_{j=1}^{N} m_{(j)} K_0(s_{(j)}). \tag{3.41}$$

The adopted kernel has the advantage of being unbiased with respect to the estimation of the central potential for a sphere with constant density (Dehnen 2001). Also, since the softening has a compact support, the potential calculation is exact (within the shell approximation) outside the softening radius.

To be sure the kernel introduces a small bias in the values of the potential evaluated between the centre and ϵ; $\Phi(r)$ is lower than the "true" value of the potential for a spherical mass distribution of constant density if $r < \epsilon$. To estimate the bias introduced we can consider the potential of a uniform sphere of unit radius equal to the kernel length ϵ. The unsoftened potential within the sphere is:

$$\Phi(r) = -\frac{1}{2}+\frac{r^2}{6}, \tag{3.42}$$

while $\Phi(r)$ evaluated through the K_0 kernel gives:

$$\Phi(r) = -\frac{1}{2}+\frac{15r^3}{16}-\frac{5r^5}{8}+\frac{3r^7}{16}-\frac{r^3}{3}\left[1+\frac{1}{2}\left(1-r^2\right)+\frac{21}{16}\left(1-r^2\right)^2\right]. \tag{3.43}$$

The two curves are plotted in Fig. 3.17.

From Equations (3.42-3.43), we can see that, as an order of magnitude, the relative error in the potential introduced within the region ϵ is smaller than the fractional mass contained in the smoothing region with respect to the total mass of the system. Since the softening length ϵ is usually chosen to be of the order of the mean inter-particle distance in the core, the bias is negligible in most situations.

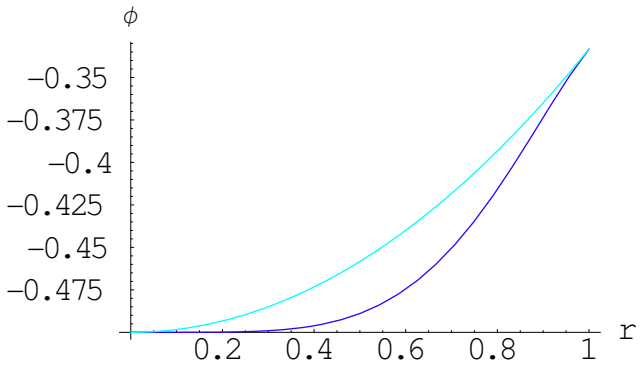

Figure 3.17: True (upper curve) and softened (lower curve) potential within a homogeneous sphere of unit radius. The softening length in the figure is $\epsilon = 1$.

3.8.2 Estimating $N(E)$: data binning

Having computed the spherically symmetric potential, we can readily obtain the single particle energy $E = w^2/2 + \Phi(r)$ and then recover a phase space density $N(E)$, normalised so that $M_{tot} = \int N(E)dE$.

A simple way to compute $N(E)$ is to order the particles with respect to their energy, and then bin them. For each bin the density in energy space is given by the sum of the masses of the bin members, divided by the difference between the maximum and minimum energy in the bin. A natural binning size, in order to reduce the noise, is given by the nearest integer to the square root of the number of particles of the system.

This binning method is the standard choice for computing $N(E)$ and $N(E, J^2)$ (normalized as $M_{tot} = \int N(E, J^2)dEdJ^2$) in our code.

We stress at this point that, while $N(E)$ can be measured in every dynamical condition of the N-body system under consideration, the step presented in the next subsection, i.e. the transformation from $N(E)$ to $f(E)$ is meaningful only for spherically symmetric isotropic configurations in quasi dynamical equilibrium.

3.8.3 From $N(E)$ to $f(E)$

Finally we have to express our measured $N(E)$ in term of the distribution function $f(E)$ for the system. The relation between $N(E)$ and $f(E)$ is given

by the following integration:

$$\begin{aligned} N(E) &= \int \delta(E-E')f(E')d\vec{x}'d\vec{w}' \\ &= 16\pi^2 \int_0^{\Phi^{-1}(E)} \sqrt{2[E-\Phi(r)]}f(E)r^2dr, \end{aligned} \tag{3.44}$$

where $\Phi^{-1}(E)$ is the radius r_{max} defined implicitly by $E = \Phi(r_{max})$. We have:

$$f(E) = \frac{N(E)}{16\pi^2 \int_0^{\Phi^{-1}(E)} \sqrt{2[E-\Phi(r)]}r^2dr}, \tag{3.45}$$

and so we need to compute the conversion factor:

$$C_r(E) = 16\pi^2 \int_0^{\Phi^{-1}(E)} \sqrt{2(E-\Phi(r))}r^2dr, \tag{3.46}$$

which is proportional to the mean radial frequency of an orbit with energy E in the potential Φ. In fact:

$$C_r(E) = \int_0^{J^2_{max}(E)} \Omega_r(E,J^2)dJ^2, \tag{3.47}$$

where $J_{max}(E)$ is the maximum angular momentum for a particle with energy E and $\Omega_r(E,J^2)$ is the classical formula for the radial frequency of orbits with a given energy and angular momentum:

$$\Omega_r(E,J^2) = 4\pi^2 \int_{r1}^{r2} \frac{dr}{\sqrt{2[E-\Phi(r)]-J^2/r^2}}. \tag{3.48}$$

In passing we note that $\Omega_r(E,J^2)$ is also the conversion factor between $N(E,J^2)$ and $f(E,J^2)$:

$$f(E,J^2) = \frac{N(E,J^2)}{\Omega_r(E,J^2)}. \tag{3.49}$$

In Fig. 3.18 we present a first application of this method to measure the distribution function $f(E)$. This is referred to a simulation of a *collisional* stellar systems, i.e. a globular cluster, and thus this example is by itself outside the scope of this Thesis, which is focused on *collisionless* systems. [For further details on the simulation from which the example has been taken, see Hut et al. (2005)].

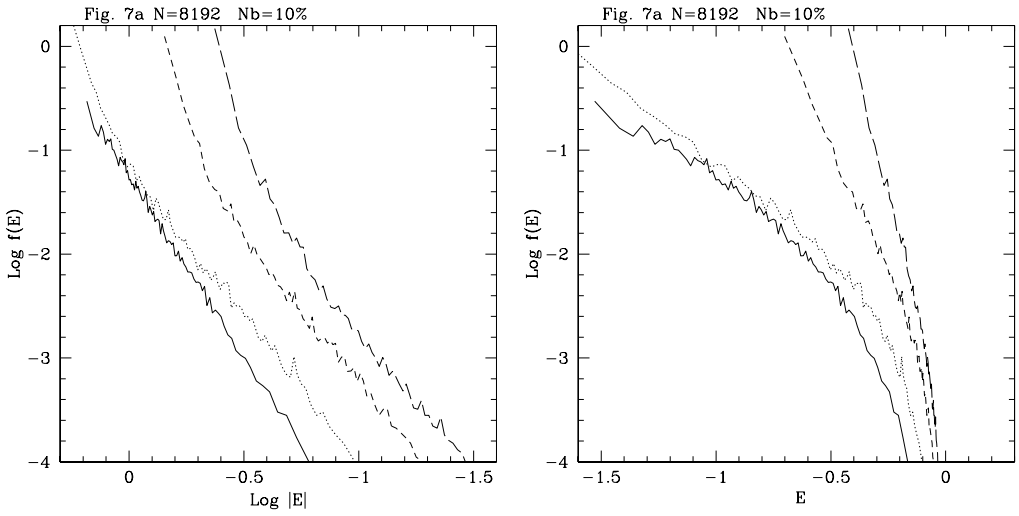

Figure 3.18: Example of a measurement of the distribution function $f(E)$ using the method presented in this Section. We note that the simulation from which $f(E)$ is measured refers to the evolution of a Plummer model with 8192 stars and a population of 10% of primordial binaries (for further details see Hut et al. 2005) and is not related to the collisionless simulations discussed in this Thesis. The only purpose here is to illustrate the method to measure $f(E)$. In the figures the distribution function per unit mass is measured, from left to right, at times $t = 0; 10; 50; 100\ t_{r_M(0)}$, where $t_{r_M(0)}$ is the initial half mass relaxation time ($t_{r_M(0)} = 0.138 N r_M^{3/2}(0)/\ln(0.11N)$). The left panel reports a logarithmic scale for E, so that the initial polytropic profile with $n = 5$ is evident. Instead the right panel has a linear scale, so that a straight line in this graph represents an isothermal profile. Note the progressive expansion ($f(E)$ is shifted to the right) of the star cluster.

3.9 Initialisation from a given distribution function

Initialising an N-body simulation according to a given distribution function $f(\vec{x}, \vec{w})$ requires to sample random points from a six dimensional probability distribution.

Usually the available random number generators provide (pseudo) random numbers uniformly distributed in the range $[0, 1]$.

Given a generic distribution function $p(\vec{x})$, there are basically two methods for sampling points from it that require only the availability of a standard uniform random number generator: (1) exact inversion (and composition) methods; (2) hit/miss method (Press et al. 1986; see also Succi 2003 Chapter 5 for a detailed discussion).

The exact inversion method works only in one dimension since it is based on the knowledge of the inverse function of the primitive of the probability distribution $P^{-1}(x)$, where P is defined as:

$$P(x) = \int_{-\infty}^{x} p(y)dy. \tag{3.50}$$

The exact inversion to generate a random number r_x from $p(x)$ simply reads:

$$r_x = P^{-1}(r_y), \tag{3.51}$$

where r_y is a random number drawn from a uniform distribution in $[0, 1]$. A geometrical representation of the concept behind exact inversion is given in Fig. 3.19. This method is especially useful to sample from exponential or Gaussian (via the Box-Muller transformation) distribution functions.

When dealing with multi-dimensional distributions, usually the second method (hit/miss) is the only one viable (except when the multi-dimensional distribution is the product of independent one-dimensional distributions). The hit/miss method was first proposed by von Neumann. The idea, illustrated for simplicity in one dimension (see Fig. 3.20), is to draw a pair of uniform random numbers (r_2, r_1) and to accept/reject them depending on whether the corresponding point falls or not within the graph of the distribution $p(x)$. The generalisation for N dimensional distribution functions is straightforward: $N+1$ uniform random numbers are drawn and are accepted if the point thus identified is below the graph of $p(\vec{x})$.

At variance with the exact inversion, the hit/miss method may suffer from efficiency problems when $p(\vec{x})$ is strongly peaked. In these cases analytical transformations to bias the uniform trial extractions of random numbers may be considered (this method is called "importance sampling" see, e.g. Succi

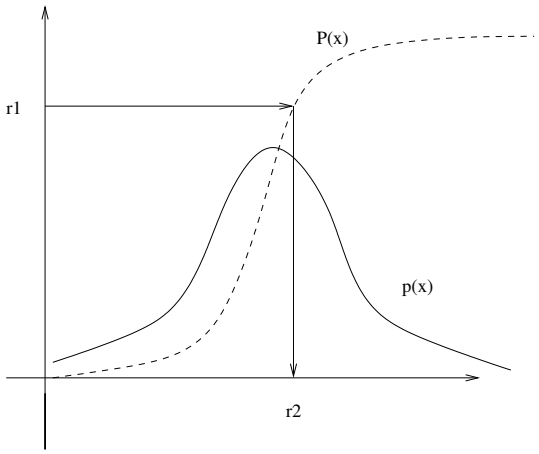

Figure 3.19: Exact inversion from a distribution $p(x)$. The uniform random number r_1 is mapped into r_2, distributed according to $p(x)$.

2003, Chapter 5). The method does not work, if the distribution function p is singular.

The initialisation of *N-body* snapshots from a given spherically symmetric distribution function can be performed by considering that the position initialisation depends only on the integrated mass profile and that exact inversion for sampling the radius of each particle can be naturally performed. Once the radius has been obtained, the angular coordinates can be sampled (uniform sampling in ϕ and in $cos(\theta)$). The velocities can then be obtained by the hit/miss method applied to the distribution function $f(\vec{x}, \vec{w})$, where $\vec{x}$ is known. The dimension of the sampling space is reduced to three (and often even more by considering additional symmetries of the distribution function, such as in the case $f(E, J)$) and efficiency problems are typically not severe. The sampling of most of the distribution functions used in this Thesis has been performed with this method. One important exception is given by low concentration polytropic spheres, that present a singular probability distribution for the velocity (see below).

3.9.1 Polytropic spheres

These isotropic models have a distribution function of the kind (e.g., see Binney & Tremaine 1987, Chapter 4)

$$f(E) = A(-E)^{n-3/2}\theta(-E), \tag{3.52}$$

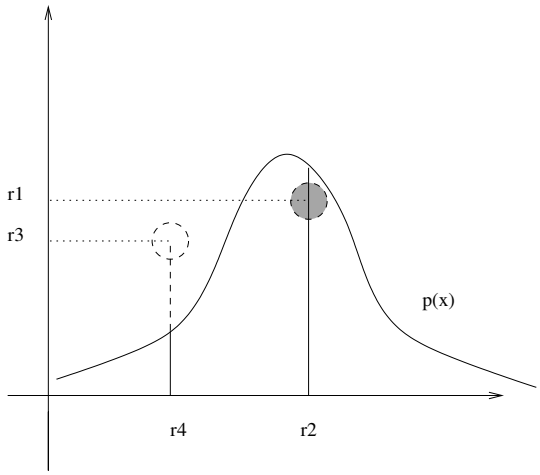

Figure 3.20: Hit/miss sampling from a distribution $p(x)$. The random number r_2 is accepted, while r_4 is rejected.

where A and $n \geqslant 1/2$ are free parameters and $\theta(x)$ is the Heavyside function ($\theta(x) = 1$ if $x \geqslant 0$ and $\theta(x) = 0$ if $x < 0$).

In general the initialisation of simulations according to the distribution function Equation (3.52) is straightforward: the positions are sampled by inversion of the mass profile to obtain r and the direction of the vector $\vec{r}$ is extracted at random. Then, the dimensionless velocity $\hat{w} = w/\sqrt{-2\Phi(r)}$ has to be sampled from the distribution:

$$p(\hat{w}) = \hat{w}^2(1 - \hat{w}^2)^{n-3/2}, \tag{3.53}$$

that is a combination of the distribution function and the phase space factor $\hat{w}^2$. If $n \geqslant 3/2$ the hit/miss method works very well, otherwise p is unbound and we must resort to exact inversion. The integral $P = \int p$ (Equation 3.50) of p (Equation 3.53) can be expressed in terms of a hypergeometric function and then inverted numerically.

3.9.2 The $f^{(\nu)}$ models

The integrated mass profile of the $f^{(\nu)}$ models, obtained by solving the self-consistent Poisson equation, is inverted numerically to sample the position space. In principle, the models extend out to infinite radii. In practice, we set a cut-off radius $r_{cutoff} \approx 50 r_M$, and rescale the mass profile in such a way that $M(r_{cutoff}) = M_{tot} = 1$.

Once the radius has been chosen, we use the hit/miss method for the sampling of the two dimensional $(w_r; w_\perp)$ velocity space, deciding at random the remaining freedom in the direction of $w_\perp$.

The combination of the adopted sampling methods ensures good accuracy, as the properties of the generated synthetic galaxies are in agreement with the theoretical expectations within 10^{-2} for typical numbers of particles $N \approx 10^5$; this limit is mainly due to the introduction of the cut-off. The method is also reasonably efficient, since between 10^2 and 10^3 hit/miss attempts, depending on the content of radial anisotropy, are required to generate the positions and velocities of one particle.

3.10 Candidate collisionless equilibria generated by the Jeans equations

Sometimes it may be interesting to initialise stellar dynamical configurations corresponding to systems with given density and pressure anisotropy profiles, for those situations where we can not resort to equilibrium models expressed in terms of distribution functions. As is well known, in general this problem is not well-posed, because a given pair $(\rho(r), \alpha(r))$ may even lack a physically acceptable underlying equilibrium distribution function. We proceed by applying the necessary constraints of the Jeans equations and then initialise our simulations with a procedure described below, well aware that we may actually miss the desired equilibrium conditions (see comment at the beginning of Sect. 4.4).

The knowledge of the density profile immediately identifies the self-consistent potential $\Phi(r)$. In addition, it defines the integrated mass profile, from which the positions of the particles can be correctly initialised. In the absence of an analytical distribution function, to complete the initialisation of the N-body collisionless candidate equilibrium configuration, we then resort to the Jeans equations to extract the information about the velocity dispersion profile that would be required by the conditions of equilibrium. In practice, for a non-rotating spherically symmetric system the relevant hydrostatic equilibrium equation can be written as:

$$\frac{d(\rho(r)\sigma_r^2(r))}{dr} + \frac{\alpha(r)}{r}\rho(r)\sigma_r^2(r) = -\rho(r)\frac{d\Phi(r)}{dr}, \tag{3.54}$$

where Φ represents the mean field gravitational potential (which can be taken to be known for known $\rho(r)$) and $\sigma_r^2 = \langle w_r^2 \rangle$ the velocity dispersion in the radial direction. For assigned profiles $(\rho(r), \alpha(r))$, under the natural boundary condition given by

$$\rho(\infty)\sigma_r^2(\infty) = 0, \tag{3.55}$$

the equation can be solved for σ_r^2:

$$\sigma_r^2(r) = \frac{1}{\rho(r)} \int_r^{+\infty} dr' \frac{d\Phi(r')}{dr'} \rho(r') \exp\left\{ \int_r^{r'} \frac{\alpha(\tilde{r})}{\tilde{r}} d\tilde{r} \right\}. \tag{3.56}$$

Thus we have obtained the velocity dispersion profiles consistent with the given density and anisotropy profiles.

At this point, we initialise our N-body code by assuming that the velocity dispersion profiles obtained above correspond, at least approximately, to a truncated Gaussian distribution in velocity space (the truncation is imposed by the requirement that only bound particles, i.e. particles with negative energy, belong to the system). This assumption gives a reasonable description of systems for which the velocity distribution is determined by physically motivated distribution functions (e.g., for the stable $f^{(\nu)}$ models); but, in general, there is no guarantee that N-body systems initialised by this method be in approximate dynamical equilibrium.

This method will be used in this Thesis to study the stability of configurations similar to those obtained as results of the evolution of cold initial conditions. Thus the limitations of this approach are not severe, because we are interested in a *stability* study. If we happen to obtain a configuration with no significant signs of evolution, we are certain *a posteriori* that a quasi-equilibrium state has indeed been produced. On the other hand, even if the initialisation gives a configuration not in dynamical equilibrium, but a nearby equilibrium configuration is approached on a very short time scale (typically on the order of one dynamical time), then we may argue that we have also obtained our goal of producing a quasi-equilibrium state with characteristics close to those desired.

3.10.1 Tests on known distribution functions

We have tested our method on isotropic systems by initialising Plummer and polytropic models and then on some anisotropic configurations associated with the $f^{(\nu)}$ family, under conditions of stability. By construction, we have a good match at the level of density, velocity dispersion, and anisotropy profiles. Differences in the fourth order moment of the velocity distribution are typically at the level of a few percent. The models initialised with the method outlined above appear to be stable, except for some modest re-arrangements of the initial anisotropy profile in the case of the $f^{(\nu)}$ models. In the latter

case, there is a tendency for the anisotropy content in the central region to decrease so that a flatter profile in $\alpha(r)$ is eventually generated.

Chapter 4

A study of the radial orbit instability

In this Chapter we investigate, by means of numerical simulations performed with the CGS code, the stability of collisionless stellar systems. In the first part of the Chapter we focus on the radial orbit instability in the $f^{(\nu)}$ family. In the second part we discuss a side, but interesting, issue with respect to the goals of this Thesis: the dependence of the radial orbit instability on the shape of the central density and anisotropy profiles. The results presented in Sect. 4.2 have been published in Trenti & Bertin (2005), while the remaining issues are discussed in a short paper (Trenti & Bertin) recently submitted.

4.1 The radial orbit instability

The study of the stability of stellar system whose distribution function is available in analytical form can be carried out along three different approaches: N-body simulations (e.g., see Henon 1973; Merritt & Aguilar 1985; Barnes et al. 1986; Aguilar & Merritt 1990; Allen et al. 1990; Stiavelli & Sparke 1991; and following papers), linear modal analysis (Polyachenko & Shukhman 1981; Palmer & Papaloizou 1987, 1988; Weinberg 1989, 1991, 1994; Saha 1991, 1992; Bertin et al. 1994; see also Fridman & Poliachenko 1984; Palmer 1993, and references therein), and energy principles (e.g., Sygnet et al. 1984; Kandrup & Sygnet 1985; Goodman 1988, and references therein).

Spherical stellar systems with too many radial orbits have thus been found to be unstable to perturbations that break the spherical symmetry and remove the excess of kinetic energy in the radial degree of freedom (see Fridman & Poliachenko 1984 and Palmer 1993). The existence of such

radial orbit instability was first investigated by Polyachenko & Shukhman (1981), who proposed an "empirical criterion" for the onset of instability ($2K_r/K_T > 1.7 \pm 0.25$) based on the global content of kinetic energy in the radial with respect to that in the tangential degrees of freedom. Following investigations (Barnes 1985; Merritt & Aguilar 1985; Aguilar & Merritt 1990; Palmer 1993) noted that different families of models may exhibit different anisotropy thresholds for the instability, thus widening the uncertainty interval around the value of 1.7 suggested earlier. For example, while for the so-called f_∞ and $f^{(\nu)}$ models a threshold value similar to that suggested by Polyachenko and Shukhman may be applicable (see Bertin & Stiavelli 1989 and next Section), for the family of Dehnen (1993) density profiles with an Osipkov-Merritt type (Osipkov 1979; Merritt 1985) of anisotropy profile it has been argued that such value is as high as ≈ 2.5 (Meza & Zamorano 1997). On the other hand, systems with an arbitrarily small content of radial anisotropy can be unstable, although with very small growth rates (as shown by Palmer & Papaloizou (1987) by means of a linear modal analysis).

The study of the stability is of primary importance in stellar dynamics, since models that are unstable on a short time scale cannot be applied to interpret the structure of observed stellar systems, because most of the observed systems are likely to be slowly evolving.

In this context, the boundary between stable and unstable models can play an interesting role, because it is often argued that galaxies are in a dynamical state close to *marginal stability*. The slow evolution of the system may be influenced by other physical processes acting on the galaxy, such as interactions with gas, globular clusters and black holes or tidal effects from neighboring objects (Bertin & Trenti 2003). Thus, while studying the stability of the $f^{(\nu)}$ models in the next Section, we also focus on the properties of the final equilibrium state reached by marginally unstable models.

In the second part of this Chapter we then discuss some interesting results on the relation between the radial orbit instability and the kinematic properties of the central region of the stellar system. Although, these results are somewhat outside the main topic of this Thesis, a better understanding of the role played by the radial orbit instability in defining the properties of collisionless systems is of high interest for the violent collapse simulations that we discuss in Chapter 6 and in the current context of structure formation.

4.2 Stability of the $f^{(\nu)}$ models

From the simple Polyachenko & Shukhman criterion for the onset of the radial orbit instability we should expect the $f^{(\nu)}$ models to become unstable

when $2K_r/K_T \gtrsim 1.75$ (Polyachenko & Shukhman (1981); see also Fridman & Poliachenko (1984)). We thus note that models with $\Psi \lesssim 4$ should be unstable, in a way that is basically independent of ν (cf. Fig. 5.9).

The study of the stability of the $f^{(\nu)}$ models could be approached either through a linear modal analysis (see Bertin et al. 1994) or by means of N-body simulations. Here we prefer the latter approach, starting from initial conditions obtained by sampling the relevant distribution functions with Monte Carlo techniques.

We have simulated the evolution of different $f^{(\nu)}$ models by means of our particle-grid code, described in Sect. 3.3. We recall that the evolution of the system is (nearly) collisionless because the simulation particles interact with one another via a mean field computed with Fourier techniques; the mean density associated with the particle distribution is expanded in spherical harmonics with contributions up to $l = 4$ (the code can handle contributions up to $l = 6$). This choice of code is well suited for our stability problem, since its performance has been tested to be high for quasi-equilibrium conditions and for smooth spherically symmetric spatial distributions. To further check our results, we have run a comparison simulation with the tree code of Londrillo (see Londrillo et al. 2003) for the $(1; 3.2)$ model and found no significant differences.

In order to sample points from the $f^{(\nu)}$ distribution function and thus to create the initial conditions needed to study the stability of the $f^{(\nu)}$ models, we have used the exact inversion technique described in Sect. 3.9.2. In principle, the models extend out to infinity. In practice, we set a cut-off radius $r_{cut} \approx 50\, r_M$, and we rescale the mass profile in such a way that $M(r_{cut}) = M$. The introduced mass "loss" is generally less than 1%.

Most simulations have been run with 2×10^5 particles. If we refer to a system with total mass $M = 10^{11}\ M_\odot$ and half-mass radius $r_M = 5\ kpc$, the evolution is followed from $t = 0$ up to $t = t_{end} = 2\ Gyr$. This corresponds to more than 20 dynamical times; in fact, for the range of $(\nu; \Psi)$ considered and the above scales for M and r_M, we have $t_d \approx (0.65 - 0.80) \times 10^8 yr$. At $t \gtrsim 10 t_d$ the system, even when it has initially evolved because of initial unstable conditions, settles down into an approximate equilibrium state.

The total energy is typically conserved within 10^{-5} over one dynamical time. The models are non-rotating; the total angular momentum remains within 10^{-4} around the small value generated in the initialization process.

To quantify the effects of the radial orbit instability, we have focused on the evolution of the central density concentration, of the shape of the inertia ellipsoid, computed on the basis of the distribution of the simulation particles within a sphere of radius $3\ r_M$, and of the global anisotropy $2K_r/K_T$ ratio. The end-products of unstable initial conditions are characterized by a final

prolate state (with axial ratios $a_2/a_1 \approx a_3/a_1 < 1$), with maximum projected ellipticity consistent with that of an $E3$ galaxy. For initially unstable models, the central density concentration drops during evolution, but the radial scale of the system remains approximately constant. For example, for the $(1/2; 3)$ model, the central concentration at the end of the simulation is more than 10 times smaller than that of the initial conditions, but the radius of the sphere that contains 5% of the total mass increases only by 6%, while the half-mass radius remains basically unchanged.

We have studied the evolution of the unstable models in terms of exponential growth curves of the form

$$g(t) = g_0 + g_1[\exp(kt) - 1], \tag{4.1}$$

where g_0, g_1, and the growth rate k are free parameters and g represents a global quantity such as the global anisotropy ratio. To capture the initial, approximately linear phase of the evolution, we have decided to make the fit in terms of the exponential growth over a reduced time interval, from $t = 0$ to $t = t_{lin} < t_{end}$, defined implicitly by the relation:

$$\left(\frac{2K_r}{K_T}\right)(t_{lin}) = \frac{1}{2}\left[\left(\frac{2K_r}{K_T}\right)(t_{end}) + \left(\frac{2K_r}{K_T}\right)(0)\right]. \tag{4.2}$$

Obviously, this choice of t_{lin} is arbitrary and should be considered only as a convenient reference time-scale.

In principle the results from the fit could be influenced by the number of particles N employed in the simulation, since we resort to the noise associated to the initial conditions to trigger the radial orbit instability. In practice we have checked that the growth rate k is measured consistently (with differences of the order 15% at most) over a wide range of N (from $2\ 10^4$ to $8\ 10^5$).

The results of the simulations are reported in Table 4.2. The threshold for instability is found to be at $2K_r/K_T \approx 1.70$, consistent with the criterion of Polyachenko & Shukhman (1981). Close to conditions of marginal stability, quantities such as $2K_r/K_T$ vary slowly and by very small amounts, so that the fit in terms of exponential growth curves is not well determined.

An interesting result is the following. We checked whether the final state reached as a result of the instability could be represented by a model of the $f^{(\nu)}$ family to which the initial unstable model belonged. To do this, we fitted the spherically averaged density and anisotropy profiles of the end-states of the simulations by means of the same family of $f^{(\nu)}$ models. The best fit model thus identified (note the quality of the fit in relation to both kinematics and density distribution) turns out to be the marginally stable model of the sequence with the same value of ν (see also the interesting

arguments and results by Palmer et al. (1990)). In the case of $\nu = 1$, which we studied in greatest detail, the profiles of the end-states obtained starting from initially unstable models with Ψ in the range from 3 to 4 are well fitted by the $(1; 4.2)$ model (see Fig. 4.1). For the violently unstable initial $(1; 2)$ model, the final state is best reproduced by the $(7/8; 4)$ model, which is still moderately unstable.

We have also run a number of simulations of models expected to be stable and checked that indeed the models preserve their state for many dynamical time scales. One of the most concentrated model that we have been able to simulate properly is the $(1/2; 9.4)$ model, for which we recall that the central concentration is $\rho(0)/\rho(r_M) = 1.14 \times 10^5$ (see Fig. 3.10).

Table 4.1: Growth rate k, with an estimate of the related uncertainty Δk, for the radial orbit instability from the simulation of a set of $f^{(\nu)}$ models. Here $\kappa = 2K_r/K_T$ is the global anisotropy parameter and $\eta = a_3/a_1$ is the axis ratio of the inertia ellipsoid referred to the sphere of radius 3 r_M. For $M = 10^{11}\ M_\odot$ and $r_M = 5\ kpc$, k is given in units of $10^{-8}\ yr^{-1}$.

$(\nu; \Psi)$	k	Δk	$\kappa(0)$	$\kappa(t_{end})$	$\eta(t_{end})$
(1;2.0)	0.85	0.1	2.65	1.87	0.65
(1;3.0)	0.48	0.07	2.17	1.84	0.67
(1;3.2)	0.37	0.07	2.09	1.84	0.69
(1;3.4)	0.34	0.07	2.02	1.83	0.74
(1;3.6)	0.30	0.05	1.95	1.85	0.80
(1;3.8)	0.16	0.04	1.89	1.82	0.85
(1;4.0)	0.08	0.05	1.84	1.81	0.91
(1;4.2)	0.007	0.10	1.78	1.76	0.94
(1;5.0)	0.001	0.01	1.60	1.60	0.99
(1;9.0)	$< 10^{-4}$	-	1.32	1.32	0.99
(3/8;3.0)	0.90	0.10	2.28	1.86	0.73
(3/8;5.0)	0.45	0.15	1.75	1.71	0.93
(1/2;3.0)	0.70	0.10	2.21	1.86	0.70
(1/2;4.0)	0.43	0.05	1.92	1.80	0.85
(1/2;5.0)	0.1	0.2	1.68	1.67	0.96
(1/2;6.0)	$< 10^{-3}$	-	1.54	1.54	0.99
(3/4;3.0)	0.64	0.05	2.20	1.85	0.70
(3/4;4.0)	0.16	0.02	1.86	1.76	0.84
(3/4;5.0)	$< 2\ 10^{-2}$	-	1.63	1.63	0.98

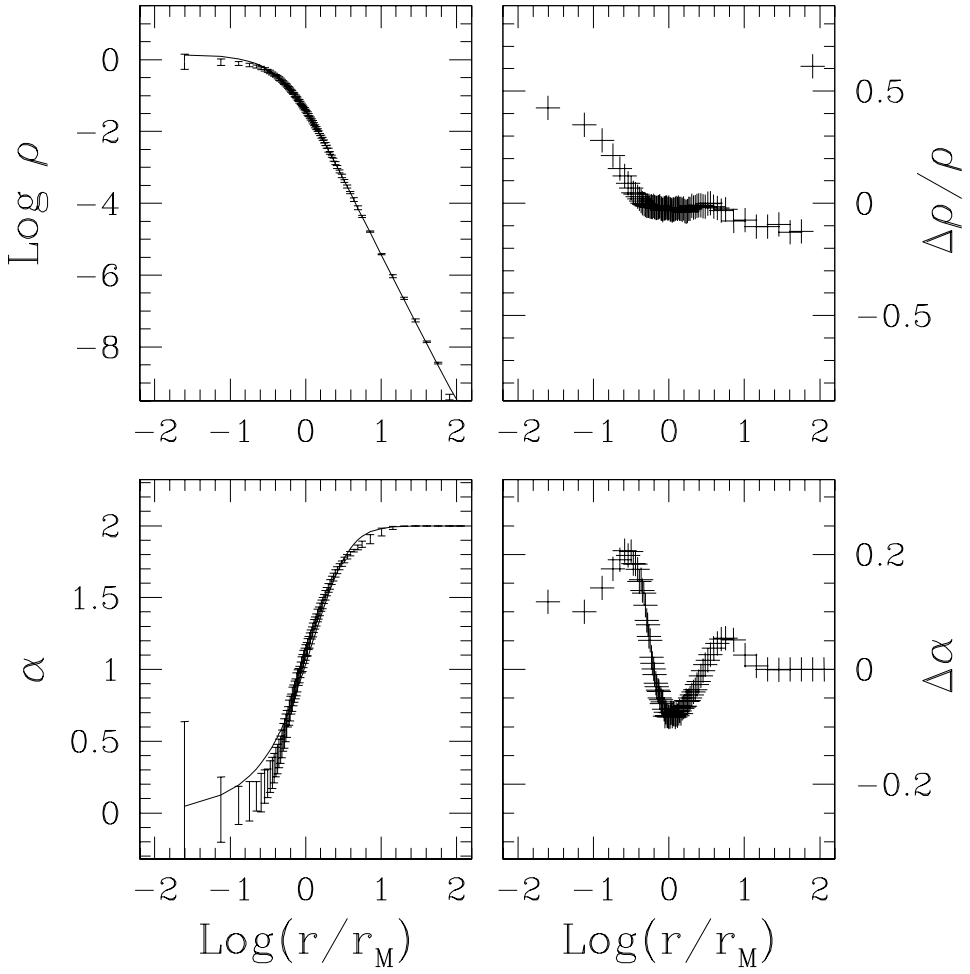

Figure 4.1: On the left frames, density and anisotropy profiles of the end-products of a simulation starting from the unstable $(1; 3.2)$ model (error bars) fitted by the marginally stable $(1; 4.2)$ model of the $f^{(\nu)}$ family (solid line); units for ρ are the units adopted in the simulation. The right frames show the residuals $\Delta\rho = \rho^{(4.2)} - \rho$ and $\Delta\alpha = \alpha^{(4.2)} - \alpha$.

4.3 Exceptionally stable equilibria resulting from special processes of collisionless collapse

In this second part of the Chapter we investigate a side, but interesting, issue with respect to the objectives of this Thesis: the apparent suppression of the radial orbit instability, that we observed in simulations starting from very cold initial conditions, and its possible physical explanations in terms of the shape of the density and anisotropy profiles reached during the collapse.

The radial orbit instability is thought to play an important role during the formation of self-gravitating structures from collisionless collapse via incomplete violent relaxation, a process that has been argued to be the main driver for the formation of elliptical galaxies (van Albada 1982). In fact, if a system starts from sufficiently cold initial conditions (i.e. with a low initial virial ratio $u = (2K/|W|)_{t=0} \lesssim 0.15$), it collapses with stars falling in almost radially toward the center, often ending up in triaxial configurations, the origin of which is attributed to the radial orbit instability (Palmer et al. 1990; Udry 1993; Hjorth & Madsen 1995). In general, when such collisionless collapse leads to "realistic" final configurations, the values of pressure anisotropy achieved at the end of the collapse turn out to be consistent with the threshold value associated with the instability criterion proposed by Polyachenko & Shukhman (1981). Currently, galaxy formation is approached in the generally accepted cosmological context of hierarchical clustering (see e.g. Meza et al. 2003, and references therein), but the mechanism of incomplete violent relaxation remains an important ingredient and thus quantifying the effects of the radial orbit instability is relevant to the explanation of the observed flattening of gravitational structures in cosmological simulations (see Hopkins et al. 2005).

Here we present the results of some numerical experiments that are aimed at clarifying the following two issues: Are there processes of collisionless collapse able to lead to equilibria of the exceptional type, that is equilibria violating the criterion proposed by Polyachenko and Shukhman (1981)? What is the structural property that makes some models with low levels of global radial anisotropy unstable and others with high levels of global radial anisotropy stable?

As to the first issue, in a set of simulations of collisionless collapse (Trenti et al. 2005; see also Chapter 6) we have investigated the role of mixing in phase space on the relaxation of the end products of the simulations. We have thus run, for comparison, a number of experiments in which phase mixing is inefficient. These are simulations with highly symmetric initial

conditions. In spite of the cold initial conditions, with $u < 0.1$, and of the high level of radial anisotropy achieved in the final configurations, with $2K_r/K_T$ sometimes above 2.5 (during the process of collapse values of $2K_r/K_T$ above 10 are reached), the radial orbit instability did not develop. From inspection of the structure of the final products of these simulations, it appears that most likely the physical factor at the basis of the observed partial suppression of the radial orbit instability is the existence of an almost perfectly isotropic central region that is realized in these systems, which appears to be more efficient for more concentrated models. This is the clue that we consider in order to address the second issue raised above.

In fact, we note that at fixed content of global anisotropy $2K_r/K_T$, the $f^{(\nu)}$ and f_∞ models (for which we find that the threshold value of $2K_r/K_T$ is close to 1.7) are less isotropic locally, in their core, than similar systems with anisotropy profiles of the type introduced by Osipkov (1979) and Merritt (1985), as studied by Meza & Zamorano (1997), which in turn are less isotropic in their central regions than the equilibrium states obtained at the end of our set of simulations. In the opposite direction, we recall that the generalized polytropic spheres, with small content of global anisotropy, found to be unstable by Palmer & Papaloizou (1987) are characterized by a constant and finite local anisotropy level down to $r = 0$. To confirm this picture and to study the effects on the radial orbit instability of central density and anisotropy profiles decoupled from each other, we cannot resort to equilibrium models with the above characteristics and with analytically available distribution function. We have then constructed with the help of the Jeans equations N-body equilibria with density and anisotropy profiles qualitatively similar to those found as end states for the simulations of collisionless collapse violating the criterion proposed by Polyachenko & Shukhman (1981) and thus demonstrated that some configurations with $2K_r/K_T$ up to ≈ 2.9 do not show evidence of rapid evolution.

4.3.1 Numerical simulations

Most of the numerical simulations of this set have been carried out with our particle-mesh code. We have also run a few simulations with the fast tree code GyrFalcON (Dehnen 2000, 2002) to check, with success, that our results are not biased by the specific choice of the numerical code.

We focus on a set of simulations that start from homogeneous spherically symmetric configurations obtained by symmetrizing a clumpy configuration with ten cold clumps, the kinetic energy of which is in the collective motion of their center of mass. In most of the runs $u = (2K/|W|)_{t=0} < 0.1$; the clump radius is taken to be equal to one half of the half-mass radius of the

Table 4.2: Collapse simulations. The simulations have been run with $N = 10^5$ particles, except $S1^+$ for which $N = 8 \times 10^5$. The columns list the initial virial ratio $u = (2K/|W|)_{t=0}$, the fractional mass loss $\Delta M = [M(t = 0) - M(t_{end})]/M(t = 0)$, the final global anisotropy $\kappa = 2K_r/K_T$ of the system of bound particles, its anisotropy radius r_α (i.e. the radius where the local anisotropy parameter is $\alpha = 1$) in units of the half-mass radius, and the ratios $\epsilon = b/a$ and $\eta = c/a$, where $a \geqslant b \geqslant c$ are the axes of the final quasi-equilibrium state computed from the inertia tensor.

	u	ΔM	κ	r_α/r_M	ϵ	η
$S1^+$	0.07	0.01	2.49	0.18	1.00	0.99
$S1^*$	0.07	0.01	2.54	0.18	0.99	0.98
$S1^\dagger$	0.07	0.01	2.52	0.18	0.98	0.97
Sa	0.05	0.03	2.75	0.18	0.98	0.97
Sb	0.03	0.07	2.56	0.16	0.79	0.66
$S2$	0.08	0.10	2.16	0.30	1.00	0.98
$S3$	0.25	0.00	2.13	0.29	0.99	0.98

system. The symmetrization is performed by accepting the radius and the magnitude of the velocity of each simulation particle, following the procedure to generate clumpy conditions discussed in Sect. 6.3, and by redistributing uniformly the angular variables in both position and velocity space. This initialization procedure leads to a smooth initial density profile, decreasing approximately linearly in radius ($\rho(0) \approx 2\rho(r_M)$), which creates a potential well that is deeper than the one of a uniform sphere with the same cutoff radius. The initial system is non-rotating and isotropic. Mild correlations in the magnitude of the velocities are present, since there is a residual memory of the cold clumpy state. The precise form of the density profile as well as the strength of the velocity correlations depend on the details of the initial random positions of the clump centers, i.e. on the seed of the random number generator.

In Table 4.2 we summarize the properties of this set of simulations. The initial conditions of the $S1$ series are generated using the same positions for the clump centers but a different total number of particles N (to ensure that the properties of the end products do not depend on N). Run $S1^+$ has 8×10^5 simulation particles; $S1^*$ and $S1^\dagger$ have 10^5 particles, but the first simulation is run with our particle-mesh code, while the second with Dehnen's code. Runs Sa and Sb are colder versions of $S1^*$ (obtained by means of a global rescaling of the initial velocities by a constant factor). Runs $S2$ and $S3$

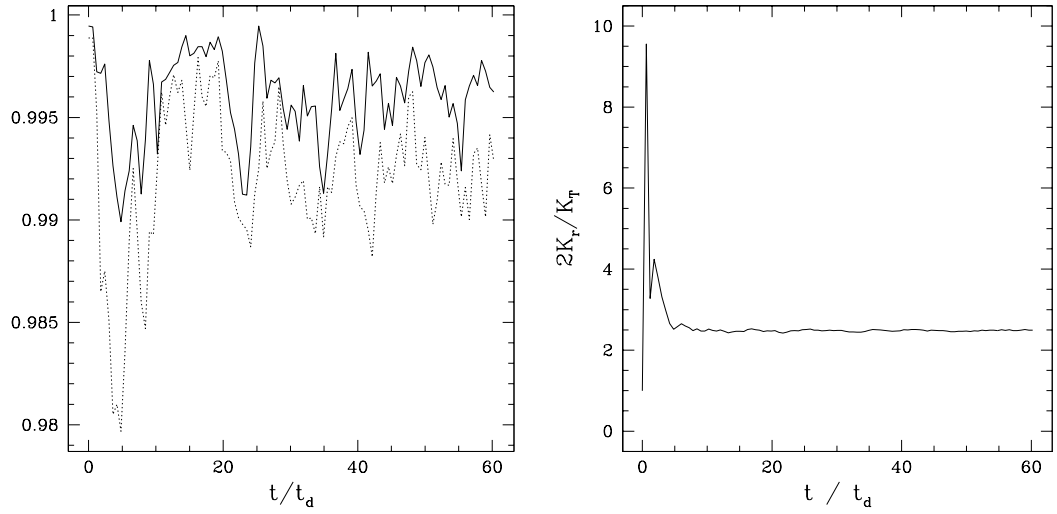

Figure 4.2: Left Panel: evolution of the aspect ratios $\epsilon = b/a$ and $\eta = c/a$, where $a \geq b \geq c$ are the values of the axes of the system evaluated from the inertia tensor, for the $S1^+$ simulation. Right panel: evolution of the ratio $2K_r/K_T$ for the same simulation.

are generated using a different seed for the random numbers. In order to characterize the level of anisotropy achieved in the end-states obtained from the simulations, we refer to the global anisotropy parameter $2K_r/K_T$ and to the anisotropy profile $\alpha(r)$, defined as $\alpha(r) = 2 - (\langle v_\theta^2 \rangle + \langle v_\phi^2 \rangle)/\langle v_r^2 \rangle$.

During collapse, the spherical symmetry is well preserved, as can be seen for $S1$ not only from the evolution of the eigenvalues of the inertia tensor of the system (Fig. 4.2), but also from the conservation of the single particle angular momenta (Fig. 4.3). Mass loss (i.e. the number of particles that acquire a positive energy during the collapse) is limited, well below the loss recorded for homogeneous uniform spheres with similar initial virial ratio u, where the system can lose up to one third of its total mass. The combination of spherical symmetry and limited mass loss leads to high final density concentrations, with $\rho(0)/\rho(r_M) \gtrsim 1500$ in run $S1$. As shown in Fig. 4.4, the density profile is reasonably well represented by a rather concentrated $f^{(\nu)}$ model or by a Jaffe density profile (Jaffe 1983).

The global amount of pressure anisotropy (see Fig. 4.2) evolves rapidly in the first few dynamical times and then reaches its quasi-equilibrium value at $t \approx 5t_d$. When $2K_r/K_T$ reaches its peak value, at the time of maximum contraction of the system, the anisotropy radius r_α (defined implicitly by $\alpha(r_\alpha) = 1$) is located well inside: at that time, for run $S1$ the mass within

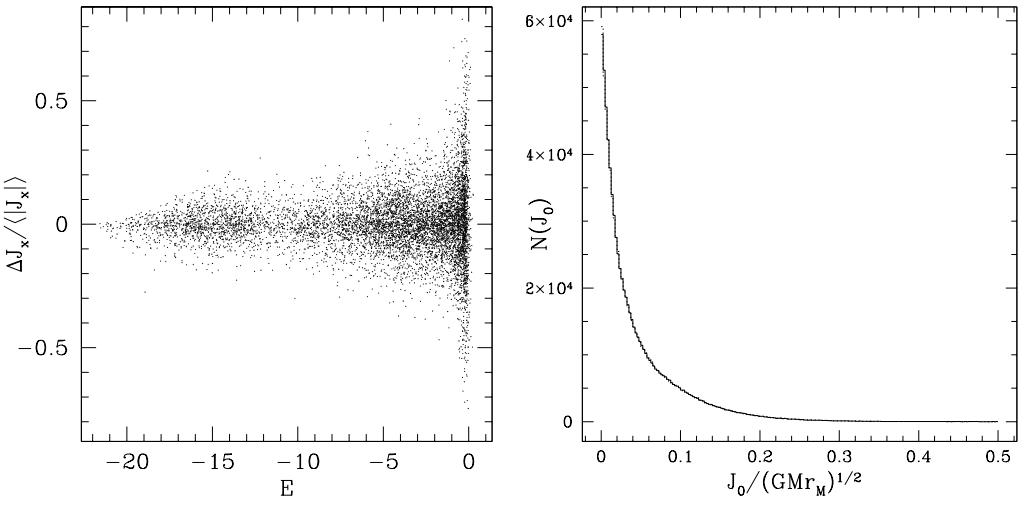

Figure 4.3: Left Panel: Variation of one component of the specific angular momentum of the simulation particles ($\Delta J_x = J_x(t_{end}) - J_x(t=0)$) relative to a reference scale, defined as the average value of $|J_x|$, for run $S1^+$. Due to the spherical symmetry, the single particle angular momenta are approximately conserved. The single particle energy E is given in code units. Right panel: Distribution of initial angular momenta for the same simulation.

r_α is only 1% of the total mass, while later the sphere associated with the anisotropy radius contains approximately 20% of the total mass. The final global content of pressure anisotropy is high also for run $S3$, which starts from moderately warm initial conditions ($u = 0.25$; for comparison, see the results of non-symmetrized runs with phase-space mixing presented in Chapter 6).

Interestingly, the central regions have a final pressure anisotropy profile slightly biased toward tangential orbits (see Fig. 4.4). This effect appears in the high resolution $S1^+$ simulation, with 8×10^5 particles; the realization with 10^5 particles ($S1^*$) does not exhibit this feature and indeed is characterized by a slightly higher value of $2K_r/K_T$. In any case the transition from isotropic to radial pressure is very sharp. The shape of the anisotropy profile cannot be represented either by a profile similar to those of the $f^{(\nu)}$ models or by an Osikpov-Merritt profile (Osipkov 1979; Merritt 1985).

To check the robustness of the numerical results, with Dehnen's tree code we have let the final configuration reached in $S1^*$ evolve for 30 additional dynamical times, without noticing any sign of significant changes. In addition, we have run a collapse simulation starting with the same initial conditions as $S1^*$ using Dehnen's tree code during the entire simulation (run $S1^\dagger$); this simulation shows no macroscopic differences with respect to $S1^*$.

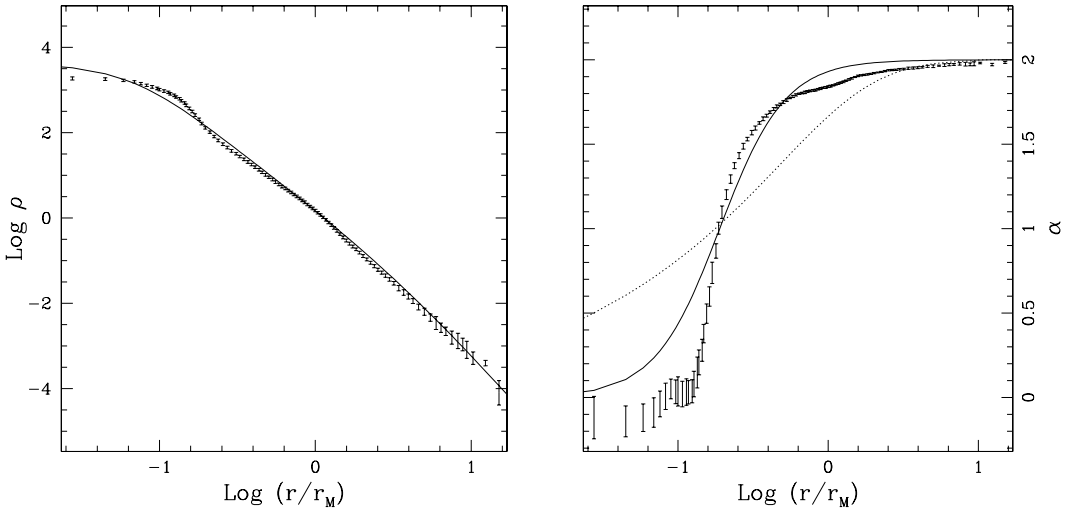

Figure 4.4: Density (left) and anisotropy profile (right) for the final state reached in the $S1^+$ simulation. The solid line in the left panel is the density profile associated with the $(1/2; 6.4)$ $f^{(\nu)}$ model. The anisotropy profile is compared to the Osipkov-Merritt profile (solid line) and to the profile for an $f^{(\nu)}$ model which has a similar amount of global anisotropy (dotted line; the $(1/2; 1)$ model with the same r_α as the end-state for $S1^+$). Clearly the theoretical models are unable to capture the rapid increase in α at $r \sim r_\alpha$.

If we consider colder and colder initial conditions within the framework of simulations considered in this paper, the radial orbit instability eventually sets in. A reduction of the initial virial ratio u below 0.05 for $S1$-like initial conditions (by rescaling the velocities by a constant factor) leads to runs that show evidence for the radial orbit instability: a simulation with $u = 0.03$ (Sb) leads to a strongly flattened system, with a final amount of global anisotropy close to 2.5.

A simulation starting from $u = 0.05$ shows an interesting behavior which we may identify as that of marginal stability, since the final state is characterized by an aspect ratio (see Fig. 4.5) η that oscillates between 0.99 and 0.93, on a time scale longer than the dynamical time; the related anisotropy content is high ($2K_r/K_T \approx 2.75$).

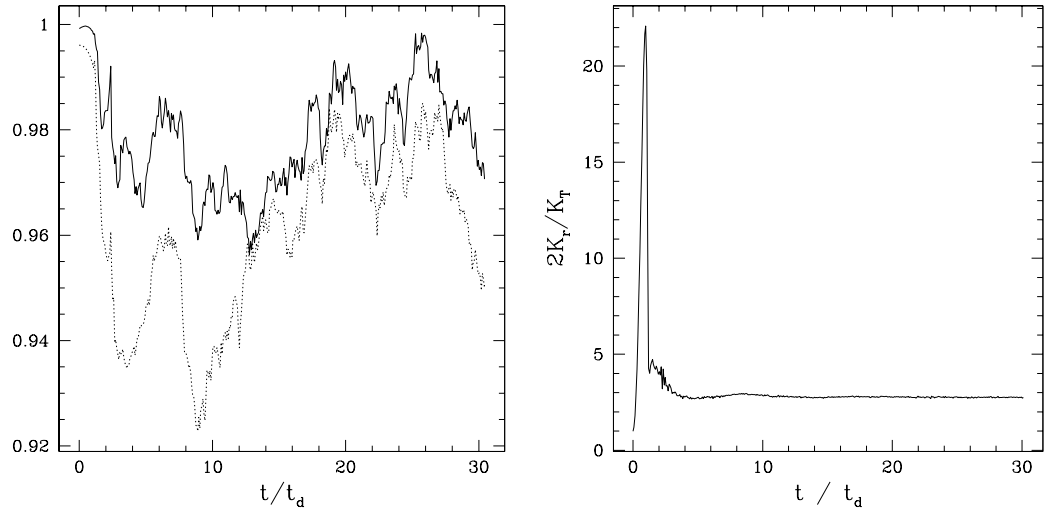

Figure 4.5: Ellipticity ratios (left) and anisotropy content (right) for the Sa simulation, as plotted in Fig. 4.2. Note the extremely high value of anisotropy content ($2K_r/K_T > 20$) reached during the collapse.

4.4 Exceptionally stable equilibria constructed from the Jeans equations

We now address the issue of whether a given initial configuration, characterized by assigned density $\rho(r)$ and pressure anisotropy $\alpha(r)$ profiles, is stable with respect to the radial orbit instability. We are not aware of models with analytical distribution function able to incorporate the sharp feature in the anisotropy profile, of the kind observed at the end of the simulations described in the previous Section. Therefore, we decided to initialize the simulations by means of candidate equilibrium solutions obtained from the Jeans equations, as outlined in Sect. 3.10. We should emphasize that the simulations that we describe below in this Section are simulations of *candidate* equilibria. In fact, since we never reach the point of actually reconstructing an underlying equilibrium distribution function, if we happened to find significant evolution we could be either in a situation of genuine instability, or, more simply, in a situation of non-equilibrium. In turn, since we will show cases where we do *not* find such evolution, we may claim that indeed we have found not only a genuine quasi-equilibrium state but also proved that it is approximately stable.

To model a density profile of the kind found in the $S1$ simulations, we

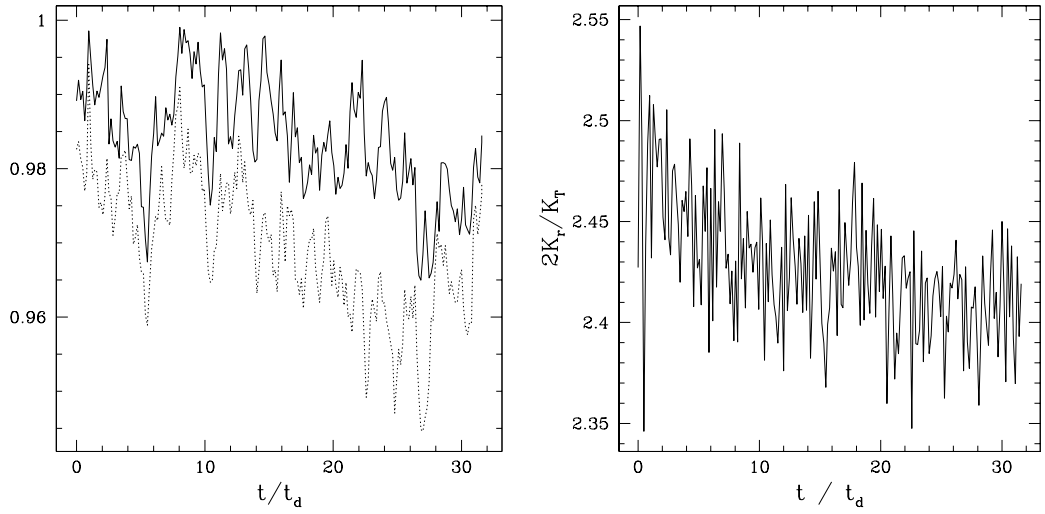

Figure 4.6: Ellipticity ratios (left) and anisotropy content (right) for the $J1$ simulation, as plotted in Fig. 4.2.

use a superposition of a regularized Jaffe profile:

$$\rho_J(r) = \frac{A}{(r^2+\epsilon^2)(r+b)^2}, \tag{4.3}$$

with A, ϵ, and b free scales, and a central core of the form:

$$\rho_C(r) = \frac{A'}{(r^2+\xi b^2)^{20}}, \tag{4.4}$$

where A' is a free scale, while ξ a dimensionless parameter of order 1 ($\xi \approx 0.6$). The form for the density $\rho_{mod} = \rho_J + \rho_C$ is taken for convenience, so as to reproduce not only the large-scale structure of the density distribution realized in the $S1$ simulations, but also the bump in the density profile around $r_M/5$ (see Fig.4.4).

As noted earlier, the $S1$ anisotropy profile is flatter than the corresponding Osipkov-Merritt profile with same r_α at small radii, while it is less steep at large radii. Thus we chose to represent the profile with:

$$\alpha(r) = 2\frac{r^\gamma}{r^\gamma + r_a^\gamma} \tag{4.5}$$

with r_a and γ being free parameters. A single choice of the $(r_a;\gamma)$ values is unable to correctly reproduce the anisotropy profile measured from the simulation over the entire radial range. Thus we fit separately the anisotropy

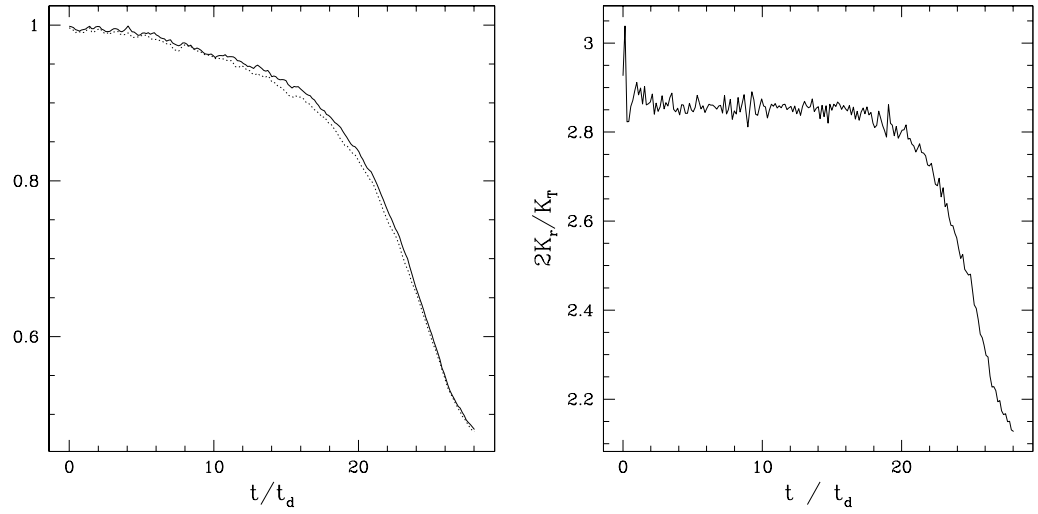

Figure 4.7: Ellipticity ratios (left) and anisotropy content (right) for the $J2$ simulation, as plotted in Fig. 4.2.

in the core, up to a radius $r_{ch} \gtrsim r_\alpha$, where $\gamma = 4$, and in the halo, i.e. for $r > r_{ch}$, where $\gamma = 6/5$. In a neighborhood around r_{ch} the two profiles are matched so that the final $\alpha(r)$ and its derivative are continuous functions.

With a suitable choice for the various parameters that define the above functions, the profiles obtained from the simulation can be fitted with an accuracy of better than 10%. We take this as a good starting point to investigate the stability of equilibrium configurations similar to those produced in the simulations of collisionless collapse.

We have first studied the evolution of a model initialized with density and anisotropy profiles similar to those of runs $S1$ (see entry $J1$ in Table 4.3). We have then proceeded to study the evolution of neighboring configurations by slightly modifying the density and/or the anisotropy profiles. In particular, we have considered models with a density profile without the inner "bump" (i.e., without the ρ_C contribution), and different forms for the anisotropy profile, ranging from steep profiles over the entire radial range, to Osipkov-Merritt and $f^{(\nu)}$-like profiles. Interestingly we have found that although none of the various combinations turns out to be violently unstable, nevertheless, the only simulation where practically no sign of evolution occurs is $J1$, the one associated with the profiles that best fit those of $S1$.

For the systems that show definite signs of evolution, the evolution appears to be very slow. For example, in the $J2$ simulation the initial configuration lasts basically unchanged for more than 10 dynamical times. In this

Table 4.3: Simulation runs initialized with models constructed from the Jeans equations. The simulations have 2×10^5 particles. Here we list the initial and final global anisotropy $\kappa = 2K_r/K_T$ of the system, its final anisotropy radius in terms of the half-mass radius, and the final aspect ratios $\epsilon = b/a$ and $\eta = c/a$, where $a \geqslant b \geqslant c$ are the axes evaluated from the inertia tensor. The initial conditions are summarized in the last column and range from the best fit of $S1$, simulation $J1$, to regularized Jaffe profiles ρ_J (see Equation 4.3) with Osipkov-Merritt or $f^{(\nu)}$ like anisotropy. Note that simulation $J4$, initialized with a regularized Jaffe density plus an unstable $f^{(\nu)}$ anisotropy profile ($\kappa \approx 2.3$) evolves rapidly within the first dynamical time and the anisotropy is quickly reduced below $\kappa = 2$ while preserving the spherical symmetry.

	κ_0	κ_{end}	r_α/r_M	ϵ	η	notes:
J1	2.47	2.42	0.26	0.98	0.98	as S1
J2	2.92	2.12	0.37	0.48	0.48	$\rho_J + \alpha_{S1}$
J3	2.40	2.45	0.28	0.96	0.94	$\rho_J + \alpha_{OM}$
J4	2.29	1.93	0.61	0.99	0.99	$\rho_J + \alpha_{f(\nu)}$
J5	2.47	2.26	0.30	0.63	0.63	$\rho_{S1} + \alpha_{OM}$

case, illustrated in Fig. 4.7, the system remains close to spherical symmetry with $2K_r/K_T \approx 2.9$, and ends up only much later as a prolate system.

4.5 Discussion and conclusions

In this Chapter we have investigated some issues related to the radial orbit instability by means of an extensive set of numerical simulations aimed at identifying the conditions for the onset of the instability.

We have checked that the $f^{(\nu)}$ models are stable if the concentration parameter Ψ is not too low (i.e., $\Psi \gtrsim 4$.) In the stable range of central concentration the models are well suited to describe the observed photometric and kinematic properties of the luminous component of bright elliptical galaxies (see Chapter 5), and provide a very good fit to the phase space structure of the end products of simulations of cold collapse (see Chapter 6). Curiously, we find that unstable models tend to evolve by staying close to the equilibrium sequence, while moving up in Ψ so as to reach marginal stability. This suggests that the products of the evolution of unstable models may be used to describe gravitational systems that shows departure from the spherical symmetry.

Interestingly the coincidence for the $f^{(\nu)}$ models between *negative thermodynamic temperature* and presence of the radial orbit instability, that we had conjectured in Sect. 2.7 on the basis of the Polyachenko & Shukhman (1981) criterion, is confirmed by the numerical investigation of the stability carried out here.

In the second part of the Chapter, we have then studied and clarified the dependence of the radial orbit instability on the shape of the anisotropy profile in the central region of a stellar system. By means of a series of numerical simulations we have shown that stable, centrally isotropic equilibria with a significant global amount of anisotropy can be reached during highly symmetric cold collapse events or initialized by solving the Jeans equations. In particular we have found a metastable state with $2K_r/K_T \approx 2.9$.

The experiments that we have performed suggest that the presence of an isotropic core may act as an important stabilizing factor for the radial orbit instability. The two-component (core-halo) structure for run $S1^+$ is indeed evident not only in the density and pressure anisotropy profiles (see the structure out to $r \approx r_M/5$ in Fig. 4.4), but also in the phase space distribution $N(E)$, as ind icated by the peak located at high values of the binding energy ($E \approx -14$, in code units; see bottom left panel of Fig. 4.4).

These results are reminiscent of the stabilizing role that a hot bulge can provide in relation to the stability of self-gravitating disks, as noted in a number of papers starting with Berman & Mark (1977) and Sellwood (1981). For disks, the detailed mechanisms underlying the origin or the suppression of global bar and spiral instabilities are reasonably well understood and known to depend on the key structural properties of the basic state (i.e., the disk density, effective velocity dispersion, and differential rotation profiles). For anisotropic spherical stellar systems we still lack a clear picture of the relevant underlying mechanisms. In this respect, the results presented here offer an interesting clue to more systematic studies that should be devoted to investigating the nature of the radial orbit instability in two-component systems, also in view of the central properties of the dark halo.

Chapter 5

$f^{(\nu)}$ Models

In this Chapter we investigate the dynamical properties of the $f^{(\nu)}$ models systematically . We also present a first comparison with the observations by fitting the photometric and kinematic profiles of the standard elliptical galaxy NGC3379. It is surprising to find that the models, in spite of their simplicity and of their one-component nature (which effectively ignores the possible presence of dark matter), manage to fit well the observations (the entire photometric profile and the kinematics out to $R \lesssim R_e$). The content of this Chapter has been published in Trenti, M. & Bertin, G. (2005) A&A 429, 161.

5.1 Introduction

A simple picture for the incomplete violent relaxation of stellar systems considers the collapse of a dynamically cold cloud of stars or star-clumps initially far from equilibrium. The study of this ideal and relatively simple process, pioneered by important analysis in the 60s (starting with Lynden-Bell 1967) and simulations in the 80s (see van Albada 1982), is still incomplete. A proper understanding of such process is a prerequisite to more ambitious attempts at constructing physically justified models of elliptical galaxies in which the problem of galaxy formation is set in the generally accepted cosmological context of hierarchical clustering.

Before the development of such cosmological scenarios, a first step (in the direction of incorporating in a simple analytical and physically justified framework the clues gathered from simulations of collisionless collapse) had been taken in terms of the so-called f_∞ models (Bertin & Stiavelli 1984). These models are constructed from a distribution function which, in the spherical limit, reduces to $f_\infty = A(-E)^{3/2} \exp(-aE - cJ^2/2)$, for negative

values of E, and vanishes for positive values of E; here A, a, and c are positive constants and E and J denote the specific star energy and angular momentum.

From those earlier investigations, it immediately became clear that the physical clues gathered from the picture of collisionless collapse (i.e., that incomplete violent relaxation leads to systems that are well relaxed in their inner regions, $r \ll r_M$, and characterized by radially anisotropic envelopes for $r \gg r_M$) do not lead uniquely to the f_∞ models, but instead identify a wide class of attractive distribution functions of which f_∞ represents just one simple and interesting case. At that time, the primary goal of a series of investigations (described, e.g., by Bertin & Stiavelli 1993) was to test whether the models inspired by studies of collisionless collapse were realistic and thus could serve as a useful tool to interpret the observations. Indeed, the f_∞ models turned out to "explain" the $R^{1/4}$ luminosity law (de Vaucouleurs 1948) and, extended to the two-component case, were used successfully to probe the presence and size of dark halos in elliptical galaxies.

Because of the focus on such astronomical applications, the problem of a detailed comparison between the f_∞ or other models and the products of collisionless collapse from N-body simulations was given lower priority and basically left aside. Yet, it was pointed out that, with respect to the products of numerical simulations of collisionless collapse, the f_∞ models had the undesired feature of being too isotropic. Some authors (Merritt et al. 1989) thus suggested that the f_∞ models should be extended to and used in the parameter domain where $a < 0$; however, this attempt failed, not only because a proper physical justification was lacking, but especially because such "negative-temperature" models suffer from the opposite difficulty, i.e. they were shown to be so anisotropic that they are violently unstable and bound to evolve on a time scale even smaller than the typical crossing time.

In a recent paper (Bertin & Trenti 2003; see also Chapter 2) we have revisited the problem of the structure and dynamics of partially relaxed stellar systems starting from a thermodynamic description. In view of the paradigm of the *gravothermal catastrophe* (see Antonov 1962; Lynden-Bell & Wood 1968; Katz 1978, 1979, 1980), we found it appropriate to approach the problem in terms of the so-called $f^{(\nu)}$ models (for a definition, see Sect. 5.2); with respect to the f_∞ models, the $f^{(\nu)}$ models follow from a statistical mechanical derivation (Stiavelli & Bertin 1987) that is formally straightforward, while they are also known to have generally similar and reasonably realistic structural properties. It should be noted that the dynamical properties of the $f^{(\nu)}$ models had not been studied earlier in detail. Such recent investigation, focusing on the issue of the gravothermal catastrophe, convinced us that the $f^{(\nu)}$ models do have many attractive features; in particular, these models

turn out to have a higher degree of radial pressure anisotropy with respect to the f_∞ models, making them more suitable to describe the results of simulations of collisionless collapse. Such encouraging preliminary inspection was the basis for a thorough study that we have thus performed and that we present here.

We provide here a systematic description of the dynamical properties of the $f^{(\nu)}$ models. In the spherical limit, these models define a *two-parameter family*, characterized by the dimensionless parameter Ψ, measuring the depth of the galaxy potential, and the dimensionless parameter ν, defining the form of a third global quantity Q (which is argued to be approximately conserved during collisionless collapse, in addition to the total energy and the total number of stars; see Sect. 5.2 for the relevant definitions). In Sect. 5.3 we present intrinsic and projected density profiles and fit the latter structural characteristics in terms of the $R^{1/n}$ law (Sersic 1968). We then proceed to illustrate in detail their phase space properties, in particular by calculating the relevant pressure tensor profiles, the pressure anisotropy content, the projected velocity dispersion profiles, the line profiles (line-of-sight velocity distribution), and the relevant phase space densities $N(E, J^2)$ and $N(E)$ (Sect. 5.4). In Sect. 5.5 we perform a first test of the viability of these models by applying them to the observed properties of NGC 3379, a galaxy that is characterized by lack of significant rotation and is likely to possess only small amounts of dark matter. The conclusions are drawn in Sect. 5.6.

This Chapter also sets the basis for a detailed comparison between the $f^{(\nu)}$ family of models and the products of collisionless collapse resulting from N-body simulations, to be presented in the next Chapter. For a full comparison with the observations of elliptical galaxies, the models should be extended to allow for the presence of a sizable dark halo and of significant rotation.

5.1.1 Models of galactic structure: physical outlook

The need for anisotropic models to describe elliptical galaxies can be traced back to the empirical arguments that come from the observations of non-spherical geometry in the absence of significant rotation (e.g., see the discussion provided by Bertin & Stiavelli 1993 and references therein); to be sure, direct evidence for pressure anisotropy in round systems is not easy to obtain, because so far the observed line profiles show only modest deviations from a Gaussian (e.g., see Gerhard et al. 2001).

The main goal of this Chapter is to study the properties of a given specific dynamical context able to provide physical justification for the existence of anisotropic equilibria, that is the dynamical framework of collisionless collapse. The process of collisionless collapse, together with its accompanying

mechanism of incomplete violent relaxation, is one (but not the only) element that is expected to play an important role in the formation of stellar systems. In spite of the many papers that have addressed issues related to such dynamical context (in addition to the papers cited earlier in the Introduction, e.g. see Shu 1978, 1987; Voglis 1994; Hjorth & Madsen 1995), it is not yet clear whether an analytically tractable distribution function, or family of distribution functions, can be assigned to the products of such collisionless collapse. Here we try to provide a contribution to this problem. At the same time, we still need to establish how far the properties of such products, often studied in a simplified one-component picture, would be from those of observed stellar systems, and in which way.

An enormous amount of work has focused and is currently focusing on the demands (on galactic structure) from the cosmological context. In particular, this has led astronomers to look for the presence, in observed objects, of cuspy density distributions of dark matter, following a universal profile suggested by cosmological simulations (see Navarro et al. 1997; Moore et al. 1998; Ghigna et al. 2000). Other studies have addressed the issue of the establishment of the galaxy scaling laws (such as the Fundamental Plane for elliptical galaxies; e.g., see Meza et al. 2003; Lanzoni et al. 2004) in the accepted cosmological scenario. These demands are beyond the scope of the present work, but should eventually be faced, as a point of contact between dynamical investigations of individual galaxies and studies of the evolving universe from which they were formed.

In this respect, a point to be noted, to avoid unnecessary confusion about the aims of purely dynamical studies, is the following. *A priori*, studies of collisionless collapse within the line of research adopted here have nothing to say about some important issues such as the establishment of the Fundamental Plane (but see González-García & van Albada 2003; Nipoti et al. 2003), because the relevant scaling laws depend on physics that goes beyond pure dynamics, which is inherently scale-free. In turn, pure dynamical studies can try to explain why galaxies prefer the $R^{1/4}$ law, which is a structural property, instead of just accepting it as an empirical fact (as often done in a number of otherwise important astrophysical studies).

Thus we would like to emphasize that this work represents only one step in the direction of a comparison with the observations. To deal fruitfully with the presence of dark matter and other important ingredients (such as significant rotation and the possible presence of an additional disk component), one first has to master the properties of one-component models, which, as shown in this Chapter, turn out to exhibit a variety of interesting dynamical properties. In fact, it is rewarding and *a priori unexpected* to find that, as a result of a simple conjecture about the way to characterize incomplete

violent relaxation (the addition of Q to the natural constraints under which Boltzmann entropy is extremized; see Sect. 5.2), one-component spherical models are identified able to fit products of N-body simulations over nine orders of magnitude in density (see next Chapter) and, at the same time, the observed photometric profile (over about ten magnitudes) and the inner kinematic profile (inside R_e) of the best studied elliptical galaxy (see Sect. 5.5). Therefore, in spite of its incompleteness, the stage reached so far is definitely interesting from the physical point of view. Discrepancies with respect to the observations play the welcome role of providing concrete indications about the role of the ingredients that are *a priori* ignored by the purely dynamical and highly simplified picture considered in this paper.

5.2 Model construction, solution and the relevant parameter space

In the spherically symmetric limit, in order to allow for the possibility that a stellar system is only partially relaxed, one may extremize the Boltzmann entropy $S = -\int f \ln f d^3x d^3w$ under the constraint that the total energy $E_{tot} = (1/3)\int E f d^3x d^3w$, the total mass $M = \int f d^3x d^3w$, and the additional quantity

$$Q = \int J^\nu |E|^{-3\nu/4} f d^3x d^3w \tag{5.1}$$

are constant (see also Sect. 2.4). We recall that $E = w^2/2 + \Phi$ and $J^2 = |\vec{r} \times \vec{w}|^2$ represent the specific energy and the specific angular momentum square of a single star subject to a spherically symmetric mean potential $\Phi(r)$.

Such extremization leads to the following expression for the $f^{(\nu)}$ distribution function:

$$f^{(\nu)} = A \exp\left[-aE - d\left(\frac{J^2}{|E|^{3/2}}\right)^{\nu/2}\right], \tag{5.2}$$

where ν, a, A, and d are positive real constants. This set of constants provides two dimensional scales, e.g. a mass and radius scale, and two dimensionless parameters, e.g. ν and γ, with

$$\gamma = \frac{a d^{\nu/2}}{4\pi G A} \tag{5.3}$$

From the definition of the $f^{(\nu)}$ distribution function (see Equation 5.2), the

constants (A, a, d) have the following dimensions:

$$A = [ML^{-6}T^3], \tag{5.4}$$
$$a = [L^{-2}T^2], \tag{5.5}$$
$$d = [L^{-\nu/2}T^{-\nu/2}]. \tag{5.6}$$

Therefore, as scales for mass and radius we may refer to:

$$R_{scale} = a^{-1/4}d^{-1/\nu}, \tag{5.7}$$
$$M_{scale} = Aa^{-9/4}d^{-3/\nu}. \tag{5.8}$$

Then, if we introduce the dimensionless potential $\hat{\Phi} = -a\Phi$, the dimensionless radius $\hat{r} = r/R_{scale}$, the dimensionless velocity $\hat{w} = \sqrt{a}w$ and a dimensionless density $\hat{\rho} = \int f^{(\nu)}d^3\hat{w}$ we can construct the $f^{(\nu)}$ models by writing the Poisson equation cast in dimensionless quantities as:

$$\frac{1}{\hat{r}^2}\frac{d}{d\hat{r}}\hat{r}^2\frac{d}{d\hat{r}}\hat{\Phi}(\hat{r}) = \frac{1}{\gamma}\hat{\rho}(\hat{r}, \hat{\Phi}), \tag{5.9}$$

in which γ is considered as an eigenvalue to be determined by imposing the two natural boundary conditions $\hat{\Phi}(0) = -\Psi$ and $\hat{\Phi}(\hat{r}) \sim -\hat{M}(\hat{r})/(4\pi\gamma\hat{r})$ as $\hat{r} \to \infty$, where $\hat{M}(\hat{r}) = \int_0^{\hat{r}} \hat{\rho}(s)d^3s$.

We have computed the two-dimensional integral for the density with an adaptive seven-point scheme (Berntsen et al. 1991) in order to properly handle the presence of a peaked integrand for certain values of the pair $(\hat{r}, \hat{\Phi})$. The Poisson equation has then been solved with a fourth order Runge-Kutta code by starting from $\hat{r} = 0$ with a seed value for γ and iterating the procedure until the boundary condition at large radii is matched within a certain accuracy. The general behavior of the function $\gamma(\Psi)$ is similar to that of the corresponding function for the f_∞ models; after some oscillations, γ tends to a "plateau" at large values of Ψ (as indicated by Fig. 5.1).

In order to check the accuracy of the numerical integration we have performed the following tests: (1) The virial theorem is satisfied with accuracy of the order 10^{-6} or better; (2) The integrated mass (from its definition) and the mass derived from the asymptotic behaviour of the potential at large radii are the same with accuracy of the order 10^{-4}; (3) The expression for $\hat{\Phi}(\hat{r})$ at large radii to two significant orders in the relevant asymptotic expansion has been checked to be correct with an accuracy from 10^{-3} to 10^{-4}; (4) The asymptotic analysis allows us to estimate the contributions to integrated quantities such as $\hat{M}$ and $\hat{E}$ external to a sphere of large radius R; this has

been checked to help improve the numerical determination of these global quantities[1].

Then we introduce the additional dimensionless quantities $\hat{r}_M = \hat{r}_M(\nu, \Psi) = r_M/R_{scale}$ and $\hat{M} = \hat{M}(\nu, \Psi) = M/M_{scale}$ for half mass radius and total mass respectively. Recalling the expression for γ (see Equation 5.3), for given ν we can express (A, a, d) in terms of (M, r_M, Ψ):

$$a = \frac{1}{4\pi G\gamma(\nu,\Psi)} \frac{r_M}{\hat{r}_M(\nu,\Psi)} \frac{\hat{M}(\nu,\Psi)}{M}, \tag{5.10}$$

$$d = [4\pi G\gamma(\nu,\Psi)]^{\nu/4} \left(\frac{M}{\hat{M}(\nu,\Psi)}\right)^{\nu/4} \left(\frac{\hat{r}_M(\nu,\Psi)}{r_M}\right)^{5\nu/4} \tag{5.11}$$

$$A = \frac{1}{[4\pi G\gamma(\nu,\Psi)]^{3/2}} \left(\frac{\hat{r}_M(\nu,\Psi)}{r_M}\right)^{3/2} \left(\frac{\hat{M}(\nu,\Psi)}{M}\right)^{1/2} \tag{5.12}$$

We have explored the parameter space (ν, Ψ) by means of an equally spaced grid from $\nu = 3/8$ to $\nu = 1$ at steps of $1/8$, and from $\Psi = 2$ to $\Psi = 13$ at steps of 0.2. A given model will be denoted by the values of the two parameters $(\nu; \Psi)$ in parentheses.

For given (ν, Ψ), once the solution for the potential $\Phi(r)$ is obtained, it can be inserted in the expression of $f^{(\nu)}$, from which all the intrinsic and observable profiles and properties of the model can be calculated.

The problem of constructing the line profiles $F(w, R)$ for a given distribution function of the form $f(E, J^2)$ is often discussed in the literature (see Gerhard 1991, 1993; Carollo et al. 1995). The calculation requires the evaluation of a triple integral (two integrations over the velocity space orthogonal to the line of sight and one over the radial coordinate along the line of sight), which we have performed numerically with the same adaptive algorithm used to compute the density (Berntsen et al. 1991). In practice, we have followed the procedure described by Gerhard (1991). The calculation of the quantities σ_{proj} and h_4 is then performed as described at the end of Sect. 5.4.3, where they are introduced and defined.

5.2.1 The parameter Ψ and the density concentration

In the following we will often refer to the parameter Ψ as the *concentration parameter*. Strictly speaking, such term is justified only at relatively large

[1]We estimate that the final relative error in the quantities along the equilibrium sequence is of the order of some parts times 10^{-4} for $\hat{M}$ and $\hat{Q}$ and some parts times 10^{-5} for $\hat{E}$. The total energy is less sensitive to the finite radius truncation error, due to its $1/R^2$ convergence.

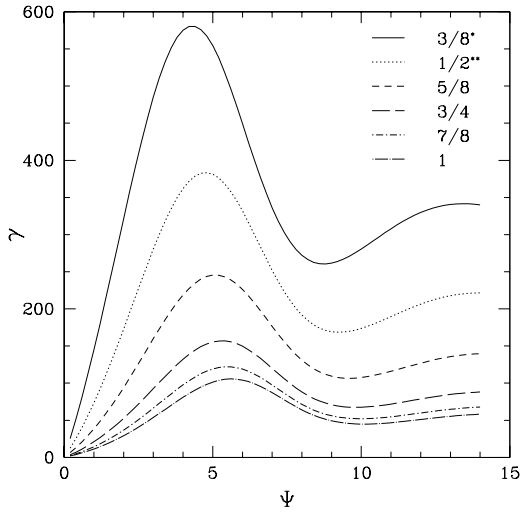

Figure 5.1: Relation $\gamma(\Psi)$ for the $f^{(\nu)}$ family of models, for selected values of ν. To fit the adopted frame, the γ values corresponding to $\nu = 3/8$ have been multiplied by a factor 1/6 and the ones corresponding to $\nu = 1/2$ by a factor 2/3.

values of Ψ ($\Psi \gtrsim 5$).

A more intuitive measure of the central concentration of a model is given by the ratio $\rho(0)/\rho(r_M)$ of the central density to the value of the density attained at the half-mass radius r_M. As illustrated in Fig. 5.2, this ratio is a monotonic increasing function of Ψ only beyond a minimum at $\Psi \approx 4.5$.

5.3 Density profiles

In this Section we start with the discussion of the properties of the density distribution.

5.3.1 The intrinsic density profile

In the outer parts, i.e. at radii such that $r \gtrsim r_M$, the density profile (Fig. 5.3) is basically the same for all models of the $f^{(\nu)}$ family. In fact, the dimensionless density associated with the $f^{(\nu)}$ distribution function can be expressed, at large values of r, as:

$$\hat{\rho}(\hat{r}) = \frac{3\pi^2}{2\sqrt{2}} \frac{\Gamma(2/\nu)}{\nu} \frac{1}{\hat{r}^2} \left(\hat{\Phi}^2(\hat{r}) + O(\hat{\Phi}^3) \right), \tag{5.13}$$

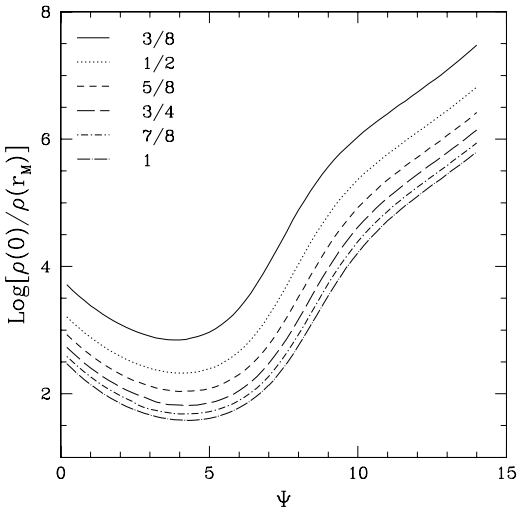

Figure 5.2: Density contrast between the center and the half-mass radius along the equilibrium sequence for different values of ν. The solid line refers to $\nu = 3/8$; at fixed Ψ, models with higher values of ν are less concentrated.

where $\Gamma(x)$ is the standard Gamma function (Abramowitz & Stegun 1965). Curiously, the $1/r^4$ behavior is found to start from well inside the main body of the system, not too far beyond r_M, while the density distribution of the inner half of the system is similar to that of an isothermal sphere. A power-law of the form $r^{-3.2}$ fits reasonably well the profiles in the transition region from r_M to $3r_M$.

As the concentration parameter Ψ increases, the point where the density profiles merge into a profile common to all the models sets in at smaller and smaller radii, so that for increasing values of Ψ the models appear to converge toward a common (singular) model with a central cusp. In these respects, the general behavior of the intrinsic density profiles is similar to that of the f_∞ models. Therefore, the behavior of concentrated models is well captured by the following simple formula (Jaffe 1983):

$$\hat{\rho}_J(\hat{r}) = \frac{1}{\hat{r}^2} \frac{1}{(1+\hat{r})^2}, \tag{5.14}$$

as shown in Fig. 5.3. Here, and in the remaining part of this subsection, a hat symbol denotes that a quantity is expressed in a suitable dimensionless form, obviously with no reference to the scaling procedure described in Sect. 5.2.

In turn, low-Ψ models are characterized by a prominent core. In fact, some models have density profiles close to that of the isochrone model (Henon 1959) or of the so-called perfect sphere ($\hat{\rho}_p = (1+\hat{r}^2)^{-2}$). The core may be

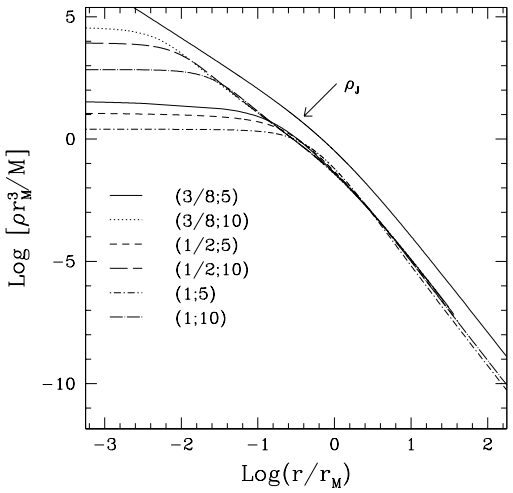

Figure 5.3: Density profile of some representative $f^{(\nu)}$ models, with $\nu = 3/8$, $1/2$, and 1, and $\Psi = 5$ and 10. The most concentrated model corresponds to $(3/8; 10)$ and the least concentrated to $(1; 5)$. If the scales are fixed so that $r_M = 10\ kpc$ and $M = 10^{11}\ M_\odot$, the units for the density are $10^{-1}\ M_\odot/pc^3$. The density profiles overlap in the outer parts, beyond a radius that becomes smaller and smaller as Ψ increases. In the plot we also record the ρ_J profile, shown here on an arbitrary scale for a convenient comparison.

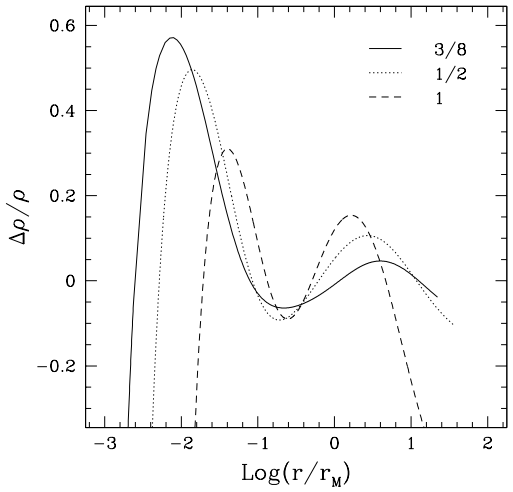

Figure 5.4: Residuals ($\triangle\rho = \rho - \rho_J$) of the density profile of some concentrated models ($\Psi = 10$, for different values of ν) from ρ_J (see Fig. 5.3 and Equation (5.14)).

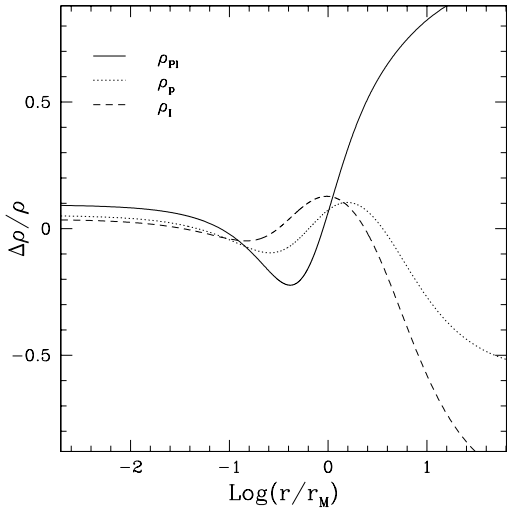

Figure 5.5: Residuals of the density profile of a low-Ψ model $(1; 4.6)$ from the isochrone density ρ_I, the perfect sphere ρ_p, and the Plummer sphere ρ_{Pl}.

even represented by the density profile of a Plummer sphere (Plummer 1915),

$$\hat{\rho}_{Pl}(r) = \frac{1}{(1+\hat{r}^2)^{5/2}}. \tag{5.15}$$

These density profiles are mentioned to better illustrate the properties of the mass distribution of the $f^{(\nu)}$ models in terms of well-known profiles (see Fig. 5.5). For a discussion of the merits and limitations of physically based models (such as the $f^{(\nu)}$ models) with respect to other models constructed on the basis of analytical convenience (e.g., see Merritt 1985, Hernquist 1990), the reader is referred to the review article by Bertin & Stiavelli (1993). On the other hand, in relation to phase-space properties, we should emphasize the following point. As will be clear from Sect. 5.4, in the approach adopted in this Thesis (in which the distribution function is constructed from physical arguments) the final velocity dispersion and pressure anisotropy profiles cannot be set independently, but follow from the self-consistent solution. In other words, all the "observable" profiles can be seen as consequences of the physical framework considered. This is in sharp contrast with other modeling procedures that are descriptive, rather than predictive (e.g., see Merritt 1985).

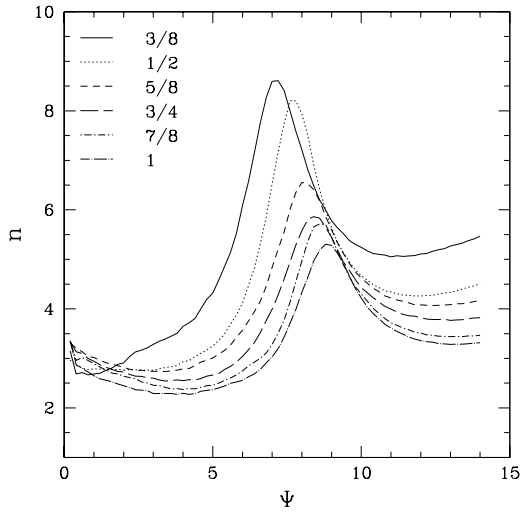

Figure 5.6: Best fit value of the index n (of the $R^{1/n}$ law) associated with the projected density profile of the $f^{(\nu)}$ models, for selected values of ν.

5.3.2 The projected density profile

We have then proceeded to compute a library of projected density profiles (which may be compared to observed luminosity profiles, under the assumption of a constant M/L ratio). A first way to characterize these profiles is to fit them with the $R^{1/n}$ law (Sersic 1968). Such fit has been performed over a very wide radial range, from $0.1R_e$ to $10R_e$. It shows that the $f^{(\nu)}$ family is well represented by the $R^{1/n}$ law, with the index n ranging from 2.5 to 8.5 (see Fig. 5.6; the slightly bumpy behavior of the $\nu = 3/8$ curve just reminds us of the uncertainties associated with the best-fit determination of n). The $n = 4$ behavior, characteristic of the de Vaucouleurs law (de Vaucouleurs 1948), is mostly associated with concentrated high-Ψ models, but we note that many intermediate-Ψ models also have the same structural property. The residuals from the $R^{1/n}$ best fit (see Fig. 5.7) are typically within 0.05 mag for concentrated models, while at low values of Ψ they are within 0.2 mag; the general behavior can be compared with that of the f_∞ models (see Fig. A.1 in Bertin et al. 2002).

5.4 Phase space properties

Here we describe the properties of the $f^{(\nu)}$ models related to the velocity space.

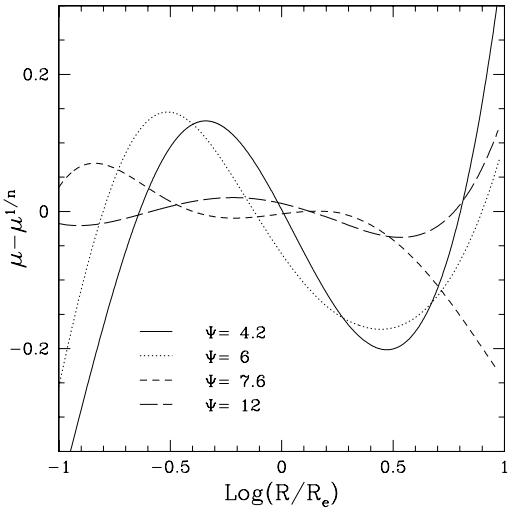

Figure 5.7: Residuals $\mu - \mu^{1/n}$, in magnitudes, obtained by fitting the $R^{1/n}$ law to the projected density profiles of the $f^{(\nu)}$ models for $\nu = 1/2$ and selected values of Ψ. The quality of the fit is excellent for concentrated models ($\Psi > 7$).

5.4.1 Pressure anisotropy profiles and global anisotropy indicators

The pressure anisotropy of the models can be described by means of the anisotropy profile $\alpha(r)$, defined as $\alpha(r) = 2 - (\langle w_\theta^2 \rangle + \langle w_\phi^2 \rangle)/\langle w_r^2 \rangle$. This function, illustrated in Fig. 5.8, shows that the cores are approximately isotropic and that in the outer parts the pressure is mostly in the radial direction, in line with the qualitative expectations of the violent relaxation scenario (Lynden-Bell 1967). Higher values of ν are associated with a sharper transition from central isotropy to radial anisotropy.

The degree of anisotropy globally present in our models can be characterized in terms of the ratio $2K_r/K_T$, where K_r is the total kinetic energy associated with the radial degree of freedom, and K_T the corresponding quantity related to the two tangential directions. All models present an excess of kinetic energy in the radial direction, as illustrated in Fig. 5.9. The ratio $2K_r/K_T$ is greater than ≈ 1.3 over the whole sequence and becomes larger than 2 in the low-Ψ region. As a general trend, at fixed Ψ, $f^{(\nu)}$ models with higher values of ν are more isotropic.

In addition to $2K_r/K_T$, as a global anisotropy indicator we can also refer to the parameter r_α/r_M (see Fig. 5.9); here the radius r_α denotes the anisotropy radius, defined from the relation $\alpha(r_\alpha) = 1$. In contrast with the

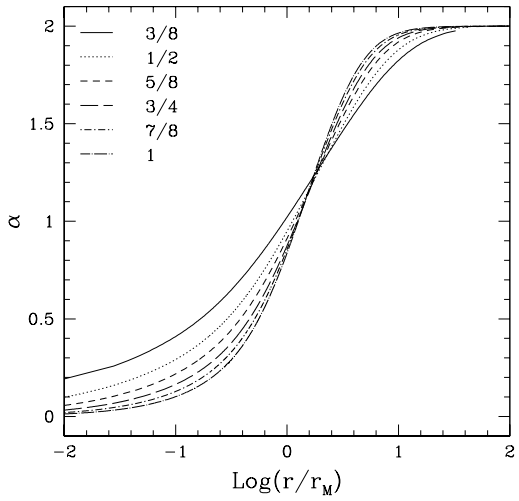

Figure 5.8: Anisotropy profiles $\alpha(r)$ of $\Psi = 5$ models for different values of ν.

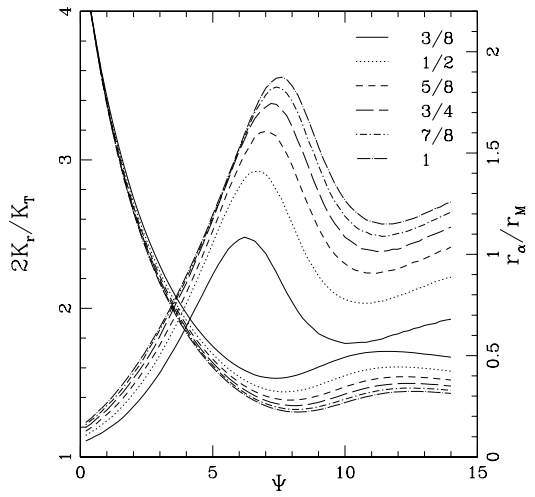

Figure 5.9: Global anisotropy of the $f^{(\nu)}$ models shown in terms of the parameter $2K_r/K_T$ (group of curves starting from the top left) and of the ratio r_α/r_M (anisotropy radius to half-mass radius; group of curves starting from the bottom left) as a function of Ψ. For low values of Ψ the global anisotropy $2K_r/K_T$ is basically independent of ν. At fixed value of Ψ the global anisotropy decreases with ν.

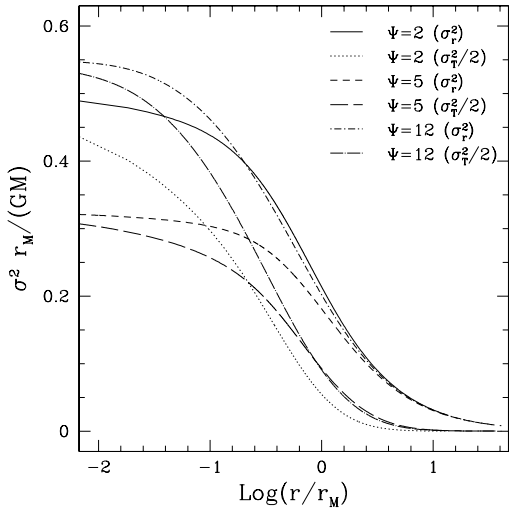

Figure 5.10: Intrinsic "pressure" profiles ($\sigma_T^2/2 = (\langle w_\theta^2\rangle + \langle w_\phi^2\rangle)/2$ and $\sigma_r^2 = \langle w_r^2\rangle$) for selected $f^{(\nu)}$ models with $\nu = 1/2$.

f_∞ models, for which $r_\alpha \approx 3r_M$ for relatively large values of Ψ, here we find that concentrated models are characterized by $r_\alpha \approx r_M$.

5.4.2 Velocity dispersion and projected velocity dispersion profiles

As we have seen, the models can be characterized by significant "pressure" anisotropy. This can be illustrated directly by the intrinsic velocity dispersion profiles, for which one may find significant differences between the tangential $\sigma_T^2/2$ and the radial dispersion σ_r^2 as far in as $r \approx 0.1\ r_M$ (see Fig. 5.10). These velocity space properties, in combination with the density distribution, give rise to the projected velocity dispersion profiles (calculated from the line profiles, as described in the next subsection), which may eventually be compared with the observed kinematical profiles; some projected velocity dispersion profiles are shown in Fig. 5.11.

5.4.3 Line profiles

Pressure anisotropy can affect the shape of the velocity distribution integrated along a given direction, which can be tested observationally by studying the profiles of the lines used to determine the observed velocity dispersion. In this context, since observational limitations prevent us from obtaining ac-

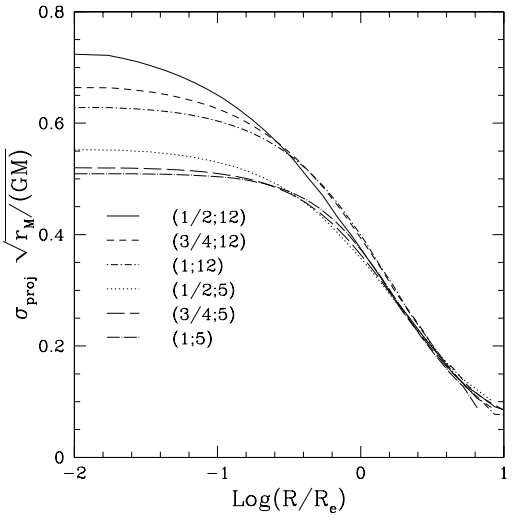

Figure 5.11: Projected velocity dispersion profile for selected $f^{(\nu)}$ models. If the scales are fixed so that $r_M = 10\ kpc$ and $M = 10^{11}\ M_\odot$, the velocity dispersion σ_{proj} is given in units of 207.4 km/s.

curate measurements of line profiles, comparisons between data and models are often carried out in terms of certain shape parameters, which measure the deviations from a Gaussian profile (e.g., see Gerhard 1991; de Zeeuw et al. 2002). In view of this approach, we have first computed the line profiles for a number of models, following the procedure described in Sect. 5.2 and then we have extracted from them the related value of the h_4 parameter (being non rotating and spherically symmetric, the $f^{(\nu)}$ models are associated with line profiles characterized by vanishing h_3).

To extract the velocity dispersion σ_{proj} and the value h_4 we fit the line profile $F(w, R)$, at fixed R, with a Gaussian corrected by a fourth order Gauss-Hermite polynomial (Abramowitz & Stegun 1965):

$$F(w,R) = F_0 \exp\left[-(w/\sigma_{proj})^2/2\right] \times \left\{1 + h_4\left[12 - 48\left(\frac{w}{\sigma_{proj}}\right)^2 + 16\left(\frac{w}{\sigma_{proj}}\right)^4\right]\right\}, \tag{5.16}$$

where F_0, σ_{proj}, and h_4 are free parameters. The fit has been performed with a Simulated Annealing method (Press et al. 1986).

In general, the deviations from a Gaussian are modest, $\approx 5\%$, and reduce to within 1% for $R \lesssim R_e$. The h_4 parameter takes on slightly negative values at the center of the system and then becomes positive in the outer parts (see Fig. 5.12), in line with the results found by Gerhard (1991).

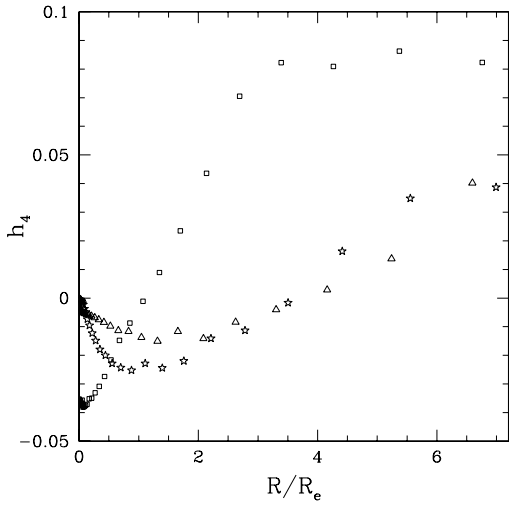

Figure 5.12: Profiles of the h_4 parameter for selected $f^{(\nu)}$ models with $\nu = 3/4$ and different values of Ψ (the $\Psi = 2$ model is denoted by squares, $\Psi = 6$ by triangles, and $\Psi = 10$ by stars).

5.4.4 The phase space densities $N(E, J^2)$ and $N(E)$

As discussed in Sect. 3.8, in view of a comparison with N-body simulations, a physically interesting way to characterize the phase space properties of the $f^{(\nu)}$ models is in terms of the $N(E, J^2)$ and $N(E)$ densities, defined in such a way that $M = \int N(E)dE = \int N(E, J^2)dEdJ^2$. Therefore, the relation between $f^{(\nu)}(E, J^2)$ and the phase space density $N(E, J^2)$ is given by the Jacobian of the transformation from $d^3\vec{x}d^3\vec{w}$ to $dEdJ^2$:

$$N(E, J^2) = \frac{2\pi f^{(\nu)}(E, J^2)}{\Omega_r(E, J^2)}, \tag{5.17}$$

where $\Omega_r(E, J^2)$ is the radial frequency of stellar orbits in the given potential $\Phi(r)$ (see Equation 3.48 for the definition of Ω_r). At variance with the f_∞ models, the $f^{(\nu)}$ models exhibit a singular behavior of $N(E, J^2)$ near the origin in the $dEdJ^2$ phase space (see Fig. 5.13).

5.5 A first comparison with the observations

The results in terms of the $R^{1/n}$ law described in Sect. 5.3.2 already show that the $f^{(\nu)}$ models possess realistic density profiles. This encouraged us to consider a direct comparison with an observed galaxy. For the purpose,

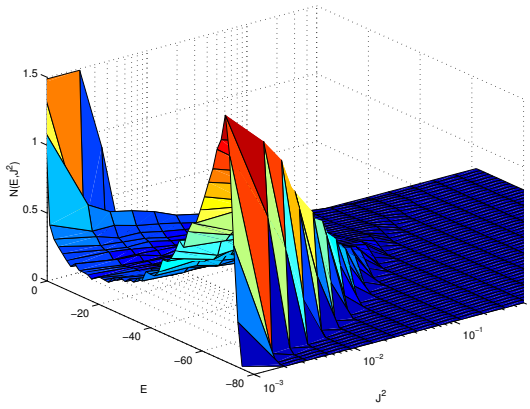

Figure 5.13: The phase space density $N(E, J^2)$ for the $(1/2; 6.2)$ $f^{(\nu)}$ model. The graph has been obtained by a Monte Carlo sampling of the distribution function with 2×10^6 points.

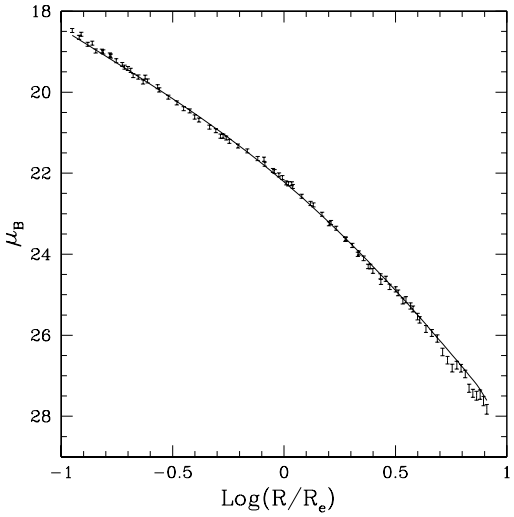

Figure 5.14: Comparison between the photometric profile of *NGC 3379* and the (1/2;9.4) model of the $f^{(\nu)}$ family. The photometric profile in B is taken from de Vaucouleurs & Capaccioli (1979). Other members of the family (e.g. the (1;9.2) model) could better reproduce the observed data especially at large radii, but they would perform less well on the velocity dispersion profile.

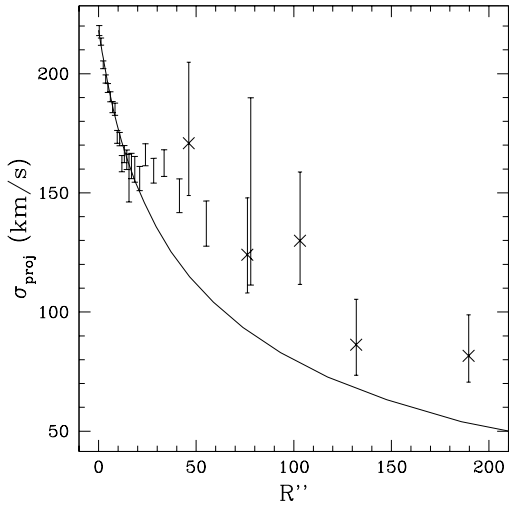

Figure 5.15: Kinematic data for *NGC 3379* described in terms of the (1/2;9.4) model of the $f^{(\nu)}$ family. The inner data (plain error bars) are taken from the stellar spectroscopy of Statler & Smecker-Hane (1999), while the outer data (crosses with error bars) refer to the binned velocity dispersion determined from the study of planetary nebulae (Romanowsky et al. 2003).

we picked the round elliptical galaxy *NGC 3379*, which apparently does not possess significant amounts of dark matter (Saglia et al. 1992, Romanowsky et al. 2003; note that the $f^{(\nu)}$ models are one-component models and thus are not applicable to systems with prominent dark halos). This galaxy has an $R^{1/4}$ luminosity profile (de Vaucouleurs & Capaccioli 1979, Capaccioli et al. 1990). For the kinematics, we considered the data of Statler & Smecker-Hane (1999) and recently published data-points based on planetary nebulae that extend well beyond R_e (Romanowsky et al. 2003).

The $f^{(\nu)}$ model that best describes the data is shown in Figs. 5.14-5.15. From such model, by adopting a distance of 11 *Mpc* for the galaxy and an absolute magnitude in B band $M_B = -20.0$, we obtain a mass-to-light ratio $M/L_B = 4.7$ in solar units. Population synthesis models for NGC 3379 predict a mass-to-light ratio between 4 and 9 (Gerhard et al. 2001). In comparison, Romanowsky et al. (2003) report a mass-to-light ratio $M/L_B = 7.1 \pm 0.6$.

5.6 Discussion and conclusions

In this Chapter we have studied the structural and dynamical properties of a two-parameter family of models of partially relaxed stellar systems. These models had been proposed earlier (Stiavelli & Bertin 1987) as physically relevant to the galaxy formation scenario based on collisionless collapse and incomplete violent relaxation. They had been noted to possess some realistic properties (for ν in the range $1/2 - 1$ and for relatively large values of Ψ). However, they had been left basically aside and not studied further in systematic detail. Additional physical interest was noted recently (Bertin & Trenti 2003), in an investigation focused on their thermodynamic properties, in relation to the paradigm of the gravothermal catastrophe. Because of such physical interest, we have decided to undertake a thorough comparison between the models and the products of collisionless collapse, as generated in N-body simulations. Such a comparison will be the subject of the next Chapter, of which the present analysis forms the necessary basis. In the next Chapter we will consider a relatively large set of simulations of collisionless collapse, starting from a variety of initial conditions. We will address the issue of the conservation of Q and identify the range of ν for which the global quantity is best conserved. Furthermore, we will show that in many cases the $f^{(\nu)}$ models can provide a surprisingly good fit to both the density and the pressure profiles, over nine orders of magnitude of the density distribution (see Sect. 6.6). The best-fit models will turn out to be close to marginal stability with respect to the radial orbit instability.

Here we have shown that the family of $f^{(\nu)}$ models exhibits a variety of structural properties, within a common general behavior. The model characteristics can be summarized by referring to three separate regimes: low-Ψ models (typically, $\Psi < 4$), intermediate-Ψ models (typically, $4 < \Psi < 8$), and high-Ψ models (typically, $\Psi > 8$). In practice, the values of Ψ that mark the transition between different regimes do not depend significantly on the value of ν, at least in the range explored in this paper (i.e., from $\nu = 3/8$ to $\nu = 1$).

In the intermediate-Ψ and the high-Ψ regimes the concentration ratio $\rho(0)/\rho(r_M)$ increases monotonically with Ψ; models with lower values of ν have larger values of $\rho(0)/\rho(r_M)$ (by up to one order of magnitude at given Ψ, in the explored range of ν). In the same regimes, as Ψ increases, the density distribution converges onto a common profile characterized by an approximate r^{-4} behavior at $r > r_M$ and by an approximate r^{-2} behavior at $r < r_M$, with an inner core that becomes smaller and smaller. In contrast, models in the low-Ψ regime have a substantial core, comparable in structure to that of a Plummer or of an isochrone model. In general, the projected

density distribution of the models is well fitted by the $R^{1/n}$ law, with n ranging from 2.5 to 8.5. Typically, high-Ψ models are accurately described in terms of the $R^{1/4}$ law.

The models are all characterized by significant radially-biased pressure anisotropy. In terms of the global anisotropy ratio $2K_r/K_T$, at given Ψ models in the low-Ψ regime have similar amounts of pressure anisotropy, which increases rapidly as Ψ decreases. In practice, all low-Ψ models should all be unstable with respect to the radial-orbit instability (see Sect. 4.2). Intermediate-Ψ and high-Ψ models appear to be safely stable, but they may be only marginally so for the lowest value of ν that we considered. This latter remark also explains why we have decided not to move below $\nu = 3/8$, given the fact that radial pressure anisotropy is larger for lower-ν models. In terms of velocity dispersion profiles, to some extent pressure anisotropy is already significant at $r \approx 0.1\ r_M$, even for stable models. However, out to $r \approx r_M$ the line profiles of stable models deviate very little from a Gaussian, with h_4 within the 5% level.

Finally, a comparison with the observed surface brightness and kinematical profiles for the galaxy NGC 3379 has shown some merits and some limitations of the one-component family of $f^{(\nu)}$ models when applied to observed objects. In particular, it is interesting to see that, within the extremely idealized framework at the basis of the construction of these models (see also the general comments made in Sect. 5.1.1), the observed luminosity profile is very well reproduced over about ten magnitudes; at the same time the models can well reproduce the inner part of the relevant kinematical profile, inside R_e. This comparison supports the view that the $f^{(\nu)}$ models may be helpful to describe the luminous component of elliptical galaxies. The obvious limitations of the one-component models that we are considering are clearly brought out by their inadequacy to capture the change in the observed kinematical profile occurring around R_e and thus their failure to reproduce such profile in the outer parts. This is interpreted as a signature of the presence of an additional component that our models, in the form developed so far, *a priori* ignore.

Chapter 6

Comparison with the products of collisionless collapse

In this Chapter we present a successful comparison between the $f^{(\nu)}$ models and the end products of simulations of collisionless collapse. The content of this Chapter has been published in Trenti, M., Bertin, G., & van Albada, T.S. (2005) A&A 433, 57.

6.1 Introduction

The collapse of a dynamically cold cloud of stars can lead to the formation of realistic stellar systems, with projected density profiles well represented by the $R^{1/4}$ law (van Albada 1982). The theoretical framework for the mechanism of incomplete violent relaxation that governs this process of structure formation was proposed by Lynden-Bell (1967), who argued that fast fluctuations of the potential during collapse would lead to the formation of a well-relaxed isotropic core, embedded in a radially anisotropic, partially relaxed halo. This general picture served as a physical justification for the construction of the so-called f_∞ models, which indeed recovered the $R^{1/4}$ law and, suitably extended to the case of two-component systems (to account for the coexistence of luminous and dark matter), led to a number of interesting applications to the observations (see Bertin & Stiavelli 1984, 1993, and references therein).

An attempt at deriving the relevant distribution function directly from the statistical mechanics of incomplete violent relaxation suggested that, in addition to the f_∞ models, one could consider alternative models, called the $f^{(\nu)}$ models (Stiavelli & Bertin 1987), with similar overall characteristics. The key ingredient for the construction of the $f^{(\nu)}$ distribution function is

the conjecture that a *third* quantity Q, in addition to the total mass M and the total energy $E_{\rm tot}$, is *approximately* conserved during the process of collisionless collapse (of course, we are referring to systems characterized by vanishing total angular momentum, $J_{\rm tot} = 0$). This quantity is introduced to model the process of *incomplete* violent relaxation, ensuring a radially biased pressure tensor and a $1/r^4$ density profile in the outer parts of the system. Because of their relatively straightforward derivation from the Boltzmann entropy, these models were revisited recently (Bertin & Trenti 2003) and used to demonstrate the onset of the gravothermal catastrophe (Lynden-Bell & Wood 1968) for such a one-parameter sequence (at fixed ν) of anisotropic equilibria; a preliminary inspection of the general characteristics of the $f^{(\nu)}$ models then convinced us that, with significant advantage over the f_∞ models, they might also serve as a good framework to interpret the results of simulations of collisionless collapse not only qualitatively, but also in *quantitative detail*. Therefore, we proceeded to examine their intrinsic properties systematically (Trenti & Bertin 2005; see also Chapter 5), and we will take advantage of that work for the study presented here.

We describe the results of a relatively wide set of numerical simulations of collisionless collapse, aimed at studying the phase space evolution and settling of the system during violent relaxation, and we then compare in detail the properties of the quasi-equilibrium end-products thus obtained with those of the $f^{(\nu)}$ models. In particular, we discuss the role played by the initial conditions and find that a certain degree of clumpiness is required for an efficient mixing in the single-particle angular momentum distribution; this form of relaxation turns out to be crucial for a good match with the $f^{(\nu)}$ family of models. The Q conservation is then studied directly by looking at its time evolution. For a significant range of collapse factors, virial ratio $u = (2K/|W|)_{t=0}$, an approximate conservation is indeed observed. The end-products (and thus the best-fitting models) tend to be characterized by a value of the global anisotropy parameter close to marginal stability with respect to the radial orbit instability (Polyachenko & Shukhman 1981).

The Chapter is organized as follows. After introducing our basic models and notation (Sect. 6.2), in Sect. 6.3 we discuss the initial conditions adopted for the simulations of collisionless collapse, with special attention to the issue of clumpiness in phase space. In Sect. 6.4 we characterize the end-products of the simulations in terms of a few key indicators (i.e., central concentration, global anisotropy, density and anisotropy profiles, deviations from spherical symmetry) and describe their dependence on the initial conditions. In Sect. 6.5 we examine the hypothesis of the approximate conservation of Q. We then move, in Sect. 6.6, to the comparison of the end-products of the simulations with the $f^{(\nu)}$ models (in terms of density and anisotropy profiles

and directly in phase space). In Sect. 6.7 we provide additional comments on the issue of clumpiness in phase space. Finally, in Sect. 6.8, we draw the main conclusions from this study.

6.2 $f^{(\nu)}$ models, units, and notation

The $f^{(\nu)}$ models (supported by the one-particle distribution function $f^{(\nu)} = A \exp\left[-aE - d(J^2/|E|^{3/2})^{\nu/2}\right]$, where a, A, d, and ν are positive constants) represent equilibrium configurations designed to describe the products of incomplete violent relaxation. They are characterized by a density profile $\rho(r)$ falling off as $1/r^4$ at large radii and as $1/r^2$ in the inner part of the system, outside a central "core". The size of the core becomes smaller as the concentration parameter Ψ increases. On the large scale, apart from such freedom in central concentration and core size, the shape of the density profile is basically independent of the $(\nu; \Psi)$ parameters (see Fig. 5.3). Interestingly, although this feature had not been imposed at the beginning (when the function $f^{(\nu)}$ is constructed), the projected density distribution of the $f^{(\nu)}$ models is typically well fitted, on the large scale, by the $R^{1/4}$ law; residuals in the fit are reduced if one considers the generalized $R^{1/n}$ law (with n a free parameter; Sersic 1968), depending on Ψ (see Figs. 5.6-5.7).

In contrast with other approaches (e.g., see Osipkov 1979 and Merritt 1985) where the anisotropy profile is assigned *a priori*, in the $f^{(\nu)}$ models the velocity dispersion anisotropy profile $\alpha(r)$, defined as $\alpha(r) = 2 - (\langle w_\theta^2 \rangle + \langle w_\phi^2 \rangle)/\langle w_r^2 \rangle$, must be computed *a posteriori* and its shape depends on ν and Ψ (see Fig. 5.8). The structure of the distribution function only guarantees that the models match the asymptotic requirements suggested by the picture of incomplete violent relaxation, i.e. at large radii, where the pressure is radial, and in the central regions, where the pressure is isotropic. The global anisotropy, measured by the quantity $2K_r/K_T$, i.e. twice the ratio of the radial to the tangential kinetic energy, depends on the choice of $(\nu; \Psi)$ and correlates with the central concentration (e.g., see Fig. 5.9). Models with $\Psi \lesssim 4$ are characterized by an excessive degree of radial anisotropy (i.e. $2K_r/K_T \gtrsim 1.7$), and are thus unstable.

The physical system of units adopted is defined by 10 kpc for length, 10^{11} $M_\odot$ for mass, and 10^8 yr for time. In this system, natural for studies on galactic scales, velocities are measured in units of ≈ 97.8 km/s and the value of the gravitational constant G is 4.4971.

The majority of simulations consists of runs starting from 20 cold clumps of 16 kpc radius in a sphere of 40 kpc radius, with $u = (2K/|W|)_{t=0}$ in the range 0.05-0.25. After the collapse the system has a half-mass radius

around 8 kpc. The total mass of the system is $2 \times 10^{11}\ M_{\odot}$. The dynamical time, which we define as $t_d = GM^{5/2}/(-2E_{\rm tot})^{3/2}$, is therefore typically $\approx 1.2 \times 10^8$ yr, i.e. 1.2 in our units. As a result, when we stop the simulation at time 80, the system has evolved for several tens of dynamical times. In any case, we should recall that the results obtained are scale-free, that is they can be rescaled to other choices of mass and radius if so desired.

6.2.1 The code

The code used in the present study is our new particle-mesh code, described in Chapter 3. For completeness, we have also run a number of comparison simulations with the fast code developed by Dehnen (2000).

6.3 Choice of initial conditions

If the initial conditions are not too artificial, during the process of collisionless collapse violent relaxation can take place, with significant mixing in phase space, and wipe out much of the details that characterize the initial conditions. In reality, violent relaxation is incomplete. Therefore, the final state is that of an approximate dynamical equilibrium characterized by an anisotropic distribution function, different from a Maxwellian (which would correspond to thermodynamic equilibrium). Because of such incomplete relaxation, the end-products of the simulations do conserve some memory of the initial state.

6.3.1 Uniform initial conditions, clumpy initial conditions, and the cosmological framework

Some of the papers addressing the problem of collisionless collapse start from "uniform" initial conditions in position and velocity space. For example, Aguilar & Merritt (1990) assume an initial $1/r$ density profile and then explore the way the collapse proceeds by varying, in addition to the initial virial ratio $u = (2K/|W|)_{t=0}$, the shape of the initial density profile (by shrinking the system along one axis) and the amount of rotation. Udry (1993) starts from uniform cold spheres, and also varies, in addition to the above-mentioned parameters, the initial anisotropy content $2K_r/K_T$. Recently, Boily et al. (2002), starting from cold uniform spheres or spheroids, focus on the effects introduced by the number of particles used in the simulation.

A few earlier investigations (van Albada 1982; McGlynn 1984; May & van Albada 1984; Londrillo et al. 1991) compared "clumpy" to "uniform" (or "homogeneous") initial conditions, showing that clumpy initial conditions lead to end-states with projected density distributions well fitted by the $R^{1/4}$ law (although Aguilar & Merritt 1990 point out that, for very small values of u, the $R^{1/4}$ law is approximately recovered even for homogeneous initial conditions). [Udry (1993) argues that starting from a multi-component initial mass spectrum for the simulation particle distribution can be an alternative way to represent a clumpy initial density configuration. However, the introduction of simulation particles so massive as to be representative of clumps would introduce effects of dynamical friction that *per se* would go beyond the picture of collisionless violent relaxation.]

Recently Roy & Perez (2004) studied the outcome of violent collapse starting from an initial uniform background with the possible addition of small clumps of stars. Although their clumpy initial conditions are rather different from those considered here, they also noted that clumpy simulations lead to steep density profiles with small cores.

As will also be demonstrated later on (see Sect. 6.4.3), the key point that distinguishes clumpy from uniform initial conditions is that, in general, only the former allow significant mixing in phase space, thus making it possible for violent relaxation to proceed properly. Here we will thus focus on simulations starting from clumpy configurations. As discussed below, for the present study we do not require that our initial clumps be in internal dynamical equilibrium, since their purpose is to avoid excessive homogeneity in the (E, J^2) phase space (see also Appendix). In particular, the clumps are *not* intended to be a realistic representation of possible conditions at a given epoch in the past. In fact, the effects of violent relaxation become important in a few dynamical times, independently of the precise epoch when the process is imagined to occur.

To be sure, to identify a realistic set of initial conditions one should consider a satisfactory cosmological framework. We plan to do this in future investigations, because this would lead us well beyond the scope of the present work. In this respect, the use of clumps is already one important step forward with respect to the use of homogeneous initial conditions. Eventually, we should devise a method for determining a "spectrum" of clumps with properties compatible with the expectations of current cosmological scenarios (see also Katz 1991, and further discussion in Sect. 6.7). For the moment, we are satisfied with identifying the initial conditions under which sufficient mixing in phase space is guaranteed. Note that cosmologically oriented simulations are centered on the clustering and growth of dark matter halos, while in this Thesis, given our focus on the $R^{1/4}$ law and on the deviations from it,

we have in mind mostly luminous matter.

6.3.2 Setting up clumpy initial conditions

In a clumpy initial state the N particles are grouped in N_C spherical clumps, each of them containing N_i stars, so that $N = \sum_{i=1}^{N_C} N_i$, with $\langle N_i \rangle = N/N_C$. Within each clump the star distribution is homogeneous. The centers of mass of the clumps are distributed uniformly inside a sphere of radius R, which defines the size of the system at the beginning of the simulation. The clump radius is R_C, with $R_C < R$, but such that $N_C \times R_C^3 > R^3$ (this condition ensures that the sphere of radius R is well filled by stars). The initial kinetic energy may be associated with the ordered motion of the center of mass of each clump (this is our default choice for the simulations of type C described below; in this case the velocity is assigned by drawing from an isotropic distribution) or with the random motions of the stars within the clump (in these cases we add a subscript h to the simulation label; here the center of mass of each clump is taken to be at rest). In general, with this choice of initial conditions the clumps are not in internal dynamical equilibrium. We note that when the number of clumps used is low, the initial configuration may deviate significantly from spherical symmetry (with projected shapes up to those of an $E3$ galaxy). Formally the limits $N_C \longrightarrow N$ and $N_C \longrightarrow 1$ both lead to homogeneous initial conditions.

In the case of homogeneous initial conditions (simulations of type U and S), which we run for comparison, we employed two kinds of distributions: (1) a constant density within a sphere of radius R; (2) a symmetrized version of a given clumpy configuration (simulations of type S). The symmetrization process in (2) is performed by accepting the radius and the magnitude of the velocity of each particle, following the procedure for initial clumpy conditions, but by redistributing the angular variables uniformly.

In principle, we have a wide parameter space to explore, because we have to deal with the initial virial ratio u, the number and size of the clumps, the cold/hot choice for the initial kinetic energy distribution (and the intermediate range of possibilities), the spatial distribution of the centers of mass of the clumps and of the stars within each clump. As noted earlier (e.g., see Londrillo et al. 1991), we anticipate that the main controlling physical parameter is the initial virial ratio.

Table 6.1 lists for each simulation the following information: the number N of particles used, the number of clumps N_C, the initial virial ratio u, the initial values of the shape parameters ϵ_0, η_0 (based on the lengths of the axes of the homogeneous ellipsoid associated with the inertia tensor, taken to be in the order $a \geq b \geq c$, so that $\eta = c/a$ and $\epsilon = b/a$; the inertia

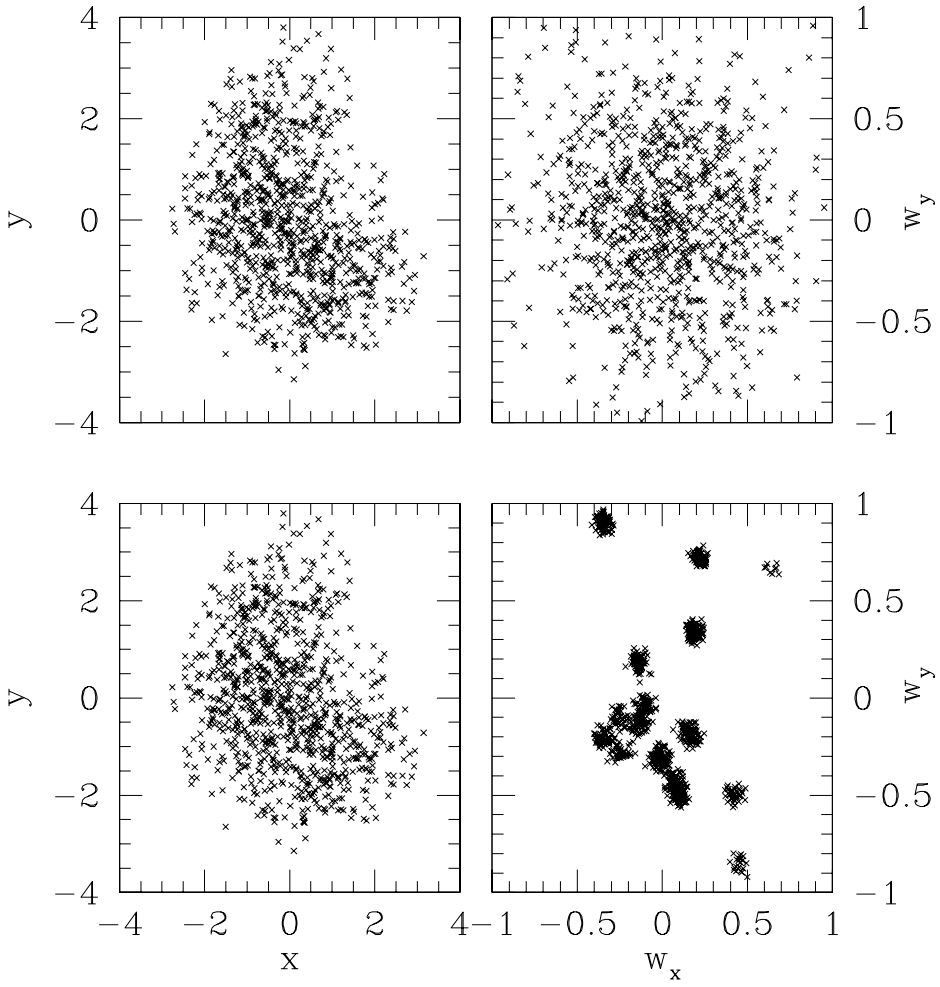

Figure 6.1: Typical projected distributions in position (left) and velocity (right) space for hot (upper panels, run $C4.1_h$) and cold (lower panels, run $C4.1$) clumpy initial conditions.

tensor is referred to the particles within a sphere of radius $3r_M$), and the initial concentration $C_{\rho 0} = (\rho(0)/\rho(r_M))_{t=0}$. As a summary for the notation used, we note the following. We have divided the set of clumpy simulations in five subsets, from $C1$ to $C5$. The simulations belonging to $C1$ start with 10^5 particles in 10 clumps, the positions of which are fixed. The $C2$ series is a high resolution (8×10^5 particles) version of $C1$, but uses instead 20 clumps. In the $C3$ (high resolution, 8×10^5 particles) and $C4$ (10^5 particles) series we use different seeds for the initial positions of the clumps and we also change other parameters as described in Table 6.1. Runs $CV5.1$ and $CP5.2^*$ are test runs specially performed to clarify some issues related to clumpiness (see Appendix). $CV5.1$ has clumpy conditions in velocity space as in run $C4.1$, but uniform homogeneous conditions in position space; in turn, $CP5.2^*$ has a clumpy configuration in position space (40 clumps of 6 kpc, with a filling factor $N_C \times R_C^3/R^3 = 0.135$) and uniform conditions in velocity space. Runs U refer to uniform homogeneous spheres (here the seed for the random numbers is not relevant given the high symmetry of the configuration) and the S series refers to the symmetrized runs.

6.4 The products of collisionless collapse

Table 6.3 lists for each simulation the following information: the relative mass loss for the end-products $\Delta M = (M_0 - M)/M_0$, the relative conservation of the global quantity Q, with $\Delta Q = |Q_0 - Q|/Q_0$ referred to $\nu = 1/2$ unless otherwise noted, the concentration $C_\rho = \rho(0)/\rho(r_M)$ of the end-products in terms of the ratio of the central density to the density at the half-mass radius, the global anisotropy parameter $\kappa = 2K_r/K_T$, the anisotropy radius (defined by the relation $\alpha(r_\alpha) = 1$) relative to the half-mass radius r_α/r_M, and the final shape parameters ϵ and η. All quantities are referred to the final system of bound particles.

6.4.1 General properties

From the results reported in Table 6.3 we may infer some empirical trends. In particular, here we focus on: (1) central concentration; (2) anisotropy content; (3) deviations from spherical symmetry; (4) mass loss. Density and anisotropy profiles will be discussed and compared with our theoretical models in Sect. 6.6.

We have run two series of simulations (type $C1$ and $C2$) for which the initial particle positions and velocities are kept fixed within each series, except for a constant scaling factor in the velocities able to lead to different values

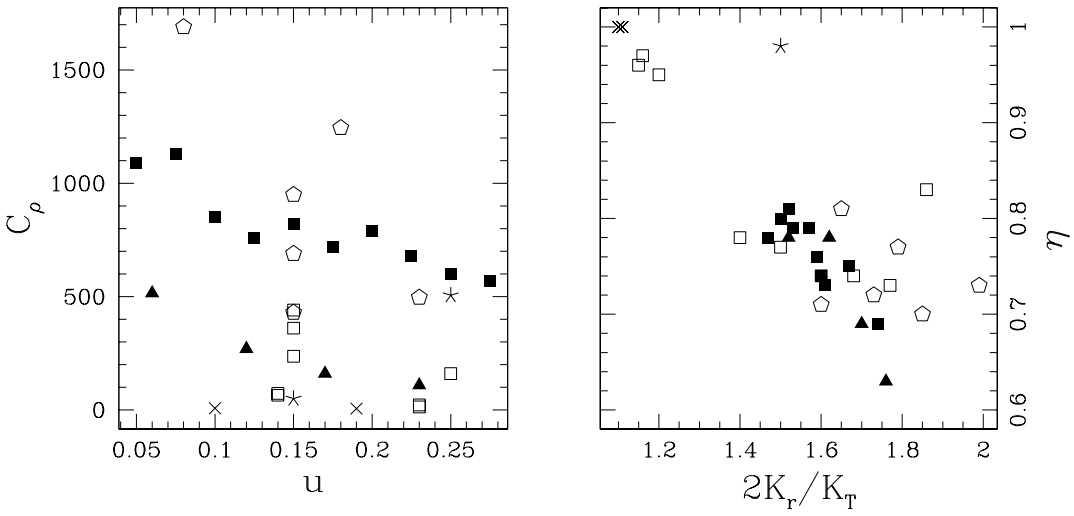

Figure 6.2: Correlations between final concentration C_ρ and initial virial ratio u (left), and between final ellipticity η and final global anisotropy $2K_r/K_T$ (right). Symbols mark the various sets of simulations as follows: filled squares for $C1$, filled triangles for $C2$, open pentagons for $C3$, open squares for $C4$, crosses for U, and stars for S.

of u (from 0.05 to 0.275 for $C1$ and from 0.06 to 0.24 for $C2$). This procedure thus allows us to explore the role of the initial virial ratio by keeping all other conditions strictly fixed.

The central concentration resulting from the collapse is expected to correlate with u. Londrillo et al. (1991) proposed a simple criterion to set an upper limit to the expected value of the central concentration by imposing the conservation of the maximum density in phase space. They argued that, for the collapse of an initially homogeneous system, the central concentration measured in terms of the ratio $r_M/r_{0.1}$ (of the half-mass radius to the radius of the sphere containing one tenth of the total mass) should scale as $1/u$. Our $C1$ and $C2$ simulations follow qualitatively the proposed trend. However, since relaxation is incomplete, it is natural to find that other factors, in addition to the value of u, can contribute to determine the properties of the final states. In fact, if we do not restrict our attention to the $C1$ and $C2$ sequences only and consider instead the entire set of simulations, we see that the correlation between u and C_ρ becomes weaker (see Fig. 6.2).

Differently from $C1$ and $C2$, the sets of $C3$ and $C4$ simulations, starting from different spatial configurations (different number and size of clumps, different seed in the random number generator), allow us to study other pos-

sible correlations, in particular those between initial and final concentration and between final concentration and initial deviations from spherical symmetry; the latter correlation was noted by Boily et al. (2002), starting from homogeneous spheroids. Again, if we include the entire set of simulations, the correlations that we find are, in general, relatively weak.

The final global anisotropy of the simulations (see the quantity κ in Table 6.3) is also weakly correlated with u, with larger values of u preferentially associated with lower levels of radial anisotropy. The series $C1$ has a systematic, but curiously non-monotonic trend, while $C3$ and $C4$ show that other factors, in addition to u, are important.

As to the shapes of the products of collisionless collapse, we note a relatively strong correlation (see Fig. 6.2) between the final shape (as measured by η) and the final level of global anisotropy (as measured by $2K_r/K_T$). This is likely to be related to the action of the radial orbit instability during collapse. In particular, for the $C2$ series lower values of u lead to more anisotropic and more flattened end products; the effect in the $C1$ series is less pronounced. Of course, the issue of the final shapes produced by collapse has been addressed by several investigations in the past, especially with the hope of establishing whether related dynamical mechanisms can account for the observed morphologies of elliptical galaxies (for simulations in the cosmological context, see Warren et al. 1992; see also Udry 1993).

Initial conditions with a small number of clumps, as considered here, often show significant deviations from spherical symmetry (from Table 6.1 we see that η_0 can be as low as 0.7). Curiously, the final value of η may even slightly exceed the value of η_0, thus showing that collapse may sometimes push the system toward spherical symmetry, not necessarily away from it.

Collisionless collapse can produce significant amounts of unbound particles and consequently give rise to mass loss. This effect is particularly severe in the cases where the collapse originates from a homogeneous sphere (see also Londrillo et al. 1991); here the system may lose up to one third of the mass (see run $U6.1$). Clumpiness appears to have a stabilizing effect with respect to mass loss; in fact, the mass lost is less than 7% even for run $C1.1$ characterized by $u = 0.06$. On the other hand, symmetrized clumpy initial states, of type S, are also found to evolve with limited mass loss. [Since the nature of the gravitational forces is mainly radial for both the collapsing homogeneous spheres (U simulations) and symmetrized clumpy configurations (S), the different amounts of mass loss might be related to the different radial density distributions for the two types of run. In fact, the effect of superimposing several clumps of particles creates a density profile decreasing approximately linearly with radius.]

6.4.2 The role of the radial orbit instability

Spherical stellar systems with an excess of radial orbits ($2K_r/K_T > 1.7 \pm 0.25$) are expected to be unstable and to evolve rapidly, on the dynamical time-scale, into ellipsoids; the precise value for the onset of the radial-orbit instability depends on the detailed structure of the system considered (Polyachenko & Shukhman 1981; see Palmer 1993, and references therein). The radial orbit instability is thought to act efficiently during collisionless collapse and is then argued to be the leading mechanism that makes cold and spherical initial configurations evolve into generally triaxial configurations (Aguilar & Merritt 1990; Polyachenko 1992). The instability may also be responsible for a reduction of the value of the central concentration reached during collapse (Merritt & Aguilar 1985); in fact, the evolution of concentrated anisotropic systems into ellipsoids is accompanied by a drastic softening of the density distribution (Stiavelli & Sparke 1991). As is the case for many other unstable systems, evolution tends to remove the source of instability and thus, in our case, to decrease the initial excess of radial orbits. Therefore, the threshold of instability should provide an upper limit to the global anisotropy of objects produced by collisionless collapse.

Our simulations largely confirm the general validity of this picture and the general applicability of the Polyachenko & Shukhman (1981) criterion (however, see Chapter 4). In particular, simulations $C2.3$ and $C2.4$ are characterized by a value of $\kappa > 1.7$ and lead to more flattened configurations than $C2.1$ and $C2.2$. Also the drop in the central concentration in simulation $C1.10$ with respect to $C1.9$ might be related to the action of the radial-orbit instability. Most of the end states are characterized by relatively high anisotropy (generally $\kappa > 1.5$, and values around 1.7 are not infrequent) and thus it seems that evolution tends to prefer a state very close to the stability boundary (as studied for the $f^{(\nu)}$ family of models in Sect. 4.2 by means of an extensive set of simulations). [An interesting finding is that symmetrized initial conditions, although artificial, can lead to spherical final states still able to sustain a large number of radial orbits ($\kappa \approx 2.1$ for simulation $S4.2$). See also Chapter 4].

6.4.3 Angular momentum mixing

Simulations with homogeneous initial conditions generate quasi-equilibrium final configurations that not only suffer from significant mass loss, but also exhibit unusual features in their anisotropy profiles (see Sect. 6.6.3 and Fig. 6.6).

If the degree of symmetry in the initial conditions is excessive, little room is left for relaxation in the (E, J^2) phase space even if the process itself

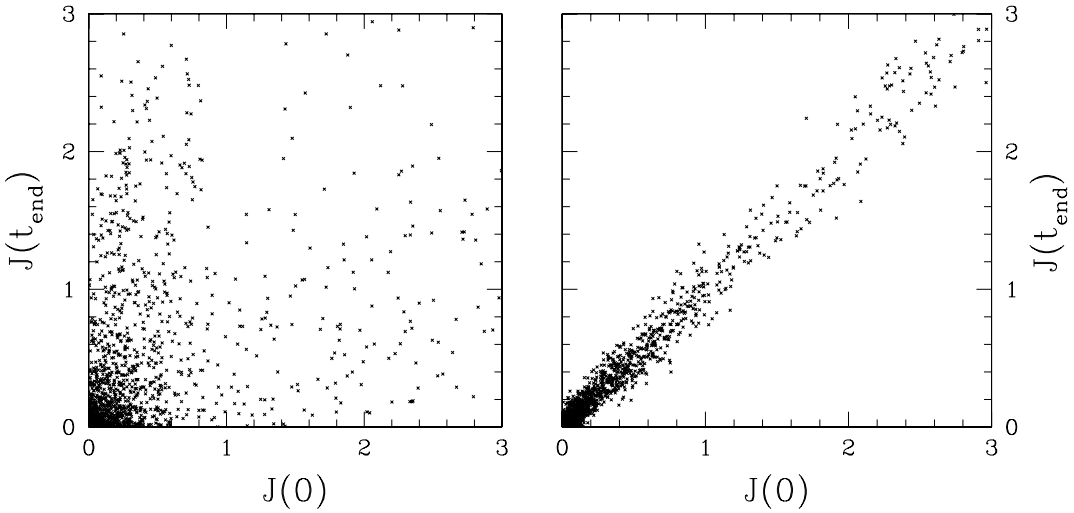

Figure 6.3: Scatter plot (final vs. initial values) for the single-particle specific angular momentum. Comparison between a clumpy simulation (run $C4.2$; left panel) and its symmetrized version (run $S4.2$; right panel). Units for J are $\mathrm{pc}^2/\mathrm{yr}$, see Sect. 6.2.

may be violent and lead to mass shedding. This is confirmed by the fact that little or no mixing is observed in the single-particle angular momentum distribution for homogeneous simulations, as reported in Fig. 6.3 (see also May & van Albada 1984). In fact, if the system evolves remaining close to spherical symmetry, the conservation of single particle angular momentum imposes severe constraints on the dynamical properties of the end-state of the collapse. On the other hand, a certain degree of clumpiness, even if limited to either position or velocity space, leads to angular momentum mixing. This is confirmed by two test simulations, $CV5.1$ and $CP5.2^*$, where mixing indeed turns out to be quite efficient and leads to J relaxation much like in the left panel of Fig. 6.3 (see also Appendix).

Clumps thus help the system reach a "universal" final state from a variety of initial conditions, which can explain the similarity of the density profiles observed in the final products of collapse simulations (see Sect. 6.6).

6.4.4 Dependence on the degree of clumpiness

A few simulations with a large number of clumps (400 in $C4.5$ and 80 in $C4.3$) and a spatial filling factor above unity confirm that, in the limit of large N_C, the evolution of the system approaches that of collapse simulations based on homogeneous conditions, with end-states characterized by a flat core and a

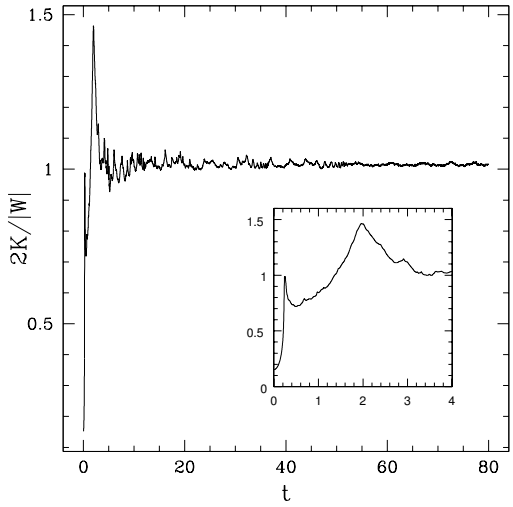

Figure 6.4: Evolution of the virial ratio during run $C4.4$, characterized by the presence of many small cold clumps. The insert box zooms in on the evolution at the beginning of the simulation, when a first collapse occurs, followed by an expansion of the clumps while collapsing toward the center of mass of the system.

low anisotropy content. A number of clumps of order 10 to 20 thus seems to be optimal for an efficient violent relaxation.

Even when limited to either position or velocity space, clumpiness can be important and still lead to end-states with general properties similar to those of the standard clumpy simulations considered in this paper (see $CV5.1$ and $CP5.2$ entries in Tables 6.1-6.3 and Sect. 6.6.5).

We also studied the dependence of the results of collisionless collapse on the spatial filling factor of the clumps. To do this, we took advantage of the ability of *GyrFalcON* to deal with systems with different scales and ran a simulation ($C4.4$) initialized with 80 *small* cold clumps (i.e. with a radius $R_C = 2.8\ kpc$ distributed in a sphere of radius 40 kpc). For this simulation, evolution basically occurs in two stages, with a first collapse in which strongly bound structures are formed in a very short time, followed by subsequent merging (see Fig. 6.4). Interestingly, the outcome of this simulation is highly isotropic ($\alpha \approx 0$ out to the half-mass radius) and very concentrated. We will see (Sect. 6.6.5) that, even in this case, the density profile remains very well represented by $f^{(\nu)}$ models (and by the $R^{1/4}$ law). For $C4.4$, after several tens of dynamical times, there remain traces (remnants) of the more strongly bound clumps, orbiting within the smooth system.

6.5 Conservation of Q

We recall that the quantity Q (for a discrete system of N particles $Q = \sum_{i=1,N}(J_i/|E_i|^{3/4})^{\nu}$; see also Sect. 6.2) has been introduced for the description of conditions in which partial violent relaxation occurs, where it is argued that information about the initial state is basically lost, except for an approximate conservation of a third quantity (in addition to total energy and total number of particles). Therefore, it would be wrong to invert the argument and imagine that, by itself, the conservation of a quantity such as Q is equivalent to the picture of incomplete violent relaxation. In particular, we note that, judging from our set of simulations, Q is well conserved for homogeneous initial conditions, both in the velocity and position space. However, this is less relevant to our goals, since homogeneous conditions do not allow mixing and violent relaxation at the level of angular momentum space to operate properly. Therefore, it is not surprising to find that the end-products of simulations with homogeneous initial conditions tend to be less well represented by the $f^{(\nu)}$ models, in spite of their relatively good conservation of Q.

In this Section we will show that the issues involved in the conjectured conservation of Q and the indications obtained from our simulations are complex. Therefore, it would be pointless to continue further in this direction, looking for a better definition of what might be defined as "acceptable degree of conservation" or searching for other quantities that might be conserved better than Q. Instead, to make a decisive test about the merits of our approach, we should take the models that have been constructed (by means of the *Ansatz* of the Q-conservation) and compare them in detail with the results of collisionless collapse obtained from our simulations. Such a test will be addressed in the following Sect. 6.6.

6.5.1 The "observed" conservation

The value of Q, computed with $\nu = 1/2$, is approximately conserved for a wide range of initial configurations. By approximate conservation we mean that $\Delta Q \leq 0.5$, although in some cases we have conservation as good as $\Delta Q \approx 0.01$. As a general rule, Q is better conserved if the initial virial ratio is not too low.

A curious property is that all clumpy simulations appear to lead to the *same* value of Q, with a scatter on the order of 10% (see Table 6.4). [I.e. the scatter is *less* than the mean deviation from exact conservation, around $20 - 30\%$.] This result can be interpreted, at the level of the simulations, by considering that, independently of the specific details of the initial clumpy

conditions, the large scale structure of the end products of the simulations is very similar, with respect both to physical scales (constrained by the conservation of mass and energy in the collapse) and to dimensionless dynamical properties at large radii (see Sect. 6.6). In addition, the fact that the values of $(M, E_{\rm tot}, Q)$ realized at the end of the simulations are approximately constant is consistent with the fact that the best-fit models do not exhibit wide variations in the values of Ψ and ν (cf. Table 6.4 and the discussion of parameter space given by Bertin & Trenti 2003, Sect. 3).

Strict conservation is not meaningful, for a number of reasons. Indeed, during collisionless collapse even the total number of particles N and the total energy $E_{\rm tot}$ are not conserved, if we refer these quantities to the final set of *bound particles*; it was noted (Stiavelli & Bertin 1987) that the non-conservation of Q actually correlates with the non-conservation of N and $E_{\rm tot}$. A simple argument also warns us that the conservation of Q should not be meant to apply to all conditions. The reason is that, if we refer to the proposed definition, Q cannot be conserved in the limit of an infinitely cold collapse. In fact, for an infinitely cold collapse (i.e. for $u \to 0$, with the stars kept at fixed initial positions), at the beginning of the simulation we would have $Q \to 0$ (because the single-particle angular momenta vanish, in the limit of vanishing initial velocities, while the single-particle binding energies remain at a finite value). On the other hand, at the end of the simulation, the formation of a quasi-isotropic core with finite kinetic energy content requires that the final value of Q be finite.

Furthermore, the quantity Q is referred to an ideal case characterized by spherical symmetry, while, as noted earlier, both the initial and the final configurations in our simulations of collisionless collapse can exhibit significant deviations from spherical symmetry. To get an estimate of changes of Q associated with deviations from spherical symmetry, we have considered a $(1/2; 3)$ $f^{(\nu)}$ model, unstable against the radial orbit instability, and let it evolve; the final quasi-equilibrium state is characterized by $\epsilon \approx \eta \approx 0.73$ and is associated with a change $\Delta Q = 0.12$. Similar changes are observed by stretching artificially an $f^{(\nu)}$ model to a non-spherical geometry, with $\epsilon = 1$ and $\eta \approx 0.7$. But these changes are given for comparison only, since they are not related to conditions in which violent relaxation takes place.

6.5.2 General polynomial dependence

Although aware of the fact that we should not really look for quantities conserved exactly during collisionless collapse, we decided to test the paradigm of Q conservation further by considering the more general class of Q functionals, defined, for a system of N points, as:

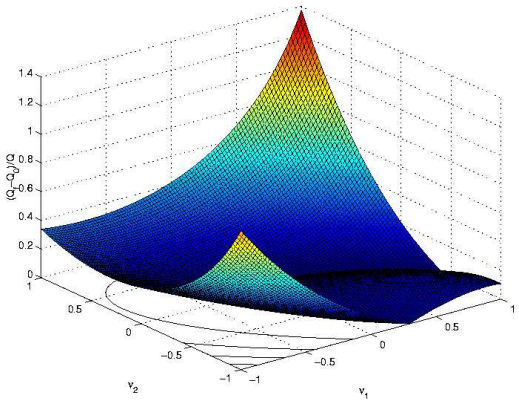

Figure 6.5: Conservation of the general functional $\tilde{Q}$ (see Equation 6.1) in a typical simulation ($C4.1$).

$$\tilde{Q} = \sum_{i=1}^{N} \frac{J_i^{\nu_2}}{|E_i|^{\frac{3}{4}\nu_1}}, \tag{6.1}$$

where ν_1 and ν_2 are free parameters. We explored the parameter space $-1 \leq \nu_1 \leq 1$ and $-1 \leq \nu_2 \leq 1$. The functional Q used to construct the $f^{(\nu)}$ models corresponds to the condition $\nu = \nu_1 = \nu_2 > 0$, which guarantees the desired asymptotic behavior for the associated density $\rho \sim r^{-4}$ at large radii.

We studied the change in the value of this functional computed at the beginning and at the end of a typical simulation (10^5 particles in 10 cold clumps, run $C4.1$; see Fig. 6.5). If we focus on the $\nu_1 = \nu_2 = \nu$ condition, the best conservation would be attained for low values of ν.

6.6 Fit with the $f^{(\nu)}$ models

We first fit the density and the pressure anisotropy profiles, $\rho(r)$ and $\alpha(r)$, of the end-products of our simulations by means of the $f^{(\nu)}$ family of models. The phase space properties of the best-fit model thus identified are then compared with those of the end-products of the simulations.

Smooth, angle-averaged simulation profiles are obtained by binning the particles in spherical shells and averaging over time, based on a total of 20 snapshots taken from $t = 64$ to $t = 80$, at an epoch when the system has already settled down in a quasi-equilibrium configuration. For the $f^{(\nu)}$ models, the parameter space explored is that of an equally spaced grid in (ν, Ψ), with a subdivision of 1/8 in ν, from 3/8 to 1, and of 0.2 in Ψ, from

0.2 to 14.0 (corresponding to the grid of models studied in Paper I). The mass and the half-mass radius of the models are fixed by the scales set by the simulations.

A minimum-χ^2 analysis is then performed, with error bars estimated from the variance in the time average process used to obtain the smooth simulation profiles. A critical step in this fitting procedure is the choice of the relative weights for the density and the pressure anisotropy profiles. We adopted equal weights for the two terms, checking a posteriori that their contributions to χ^2 are of the same order of magnitude.

6.6.1 Density profiles

Since the half-mass radius r_M and the total mass M are kept fixed in the fitting procedure, we are left with two degrees of freedom (i.e., the dimensionless parameters ν and Ψ). In practice, given the general behavior of the density profile of the $f^{(\nu)}$ models (see Fig. 5.3), at large radii the freedom in the fit is limited. Therefore, the excellent match at large radii to the density profile of the end-products of the simulations demonstrates that the $f^{(\nu)}$ family has been constructed on solid physical grounds. Different values of (ν, Ψ) correspond to different shapes of the inner potential well and of the anisotropy profile. As exemplified by Figs. 6.7-6.10, the density of the final systems produced by the high resolution set of simulations ($C2$ and $C3$) is well represented by the best-fit $f^{(\nu)}$ profile over the entire radial range, from 0.1 to 10 half mass radii. The fit is satisfactory not only in the outer parts, where the density falls by *nine orders of magnitude* with respect to the central regions, but also in the inner regions. The mean absolute relative deviation between simulations and models ($\langle|\Delta\rho/\rho|\rangle = (1/N_g)\sum_{i=1}^{N_g}|\rho_{\rm sim}(r_i) - \rho_{\rm model}(r_i)|/\rho_{\rm sim}(r_i)$), computed over this extended radial range, is usually around 10% (see Table 6.4); here N_g represents the number of radial grid points.

With a similar procedure, we have studied the end-products of simulations characterized by different numbers of particles and clumps ($C1$ and $C4$). No significant changes in the quality of the fits are found if we focus on simulations characterized by clumpy initial conditions (with the possible exception of those run with $N_C \geq 80$) .

6.6.2 Projected density profiles

The end-products of collisionless collapse are known to be characterized by projected density profiles generally well fitted by the $R^{1/4}$ law (de Vaucouleurs 1948), provided that the collapse factor is large (i.e., that the initial virial

ratio u is small; see van Albada 1982; Londrillo et al. 1991). With our set of simulations we confirm this result and we extend it by means of the $f^{(\nu)}$ models.

The successful comparison between models and simulations is interesting because, depending on the value of u, some simulations lead to configurations that exhibit deviations from the $R^{1/4}$ law. In these cases, the density profile projected along the line of sight is characterized by an $R^{1/n}$ behavior with $n \neq 4$. For example, the $C2.4$ simulation, which starts with a low collapse factor, has a best fit index $n \approx 3$, while the the simulation $C3.1$, which has a large collapse factor, is best represented by a profile with $n \approx 5$. Yet these systems all turn out to be well fitted by the $f^{(\nu)}$ models. Therefore, the family of models that we have identified might also be useful for describing systematic structural changes in galaxies, in the framework of the proposed weak homology of elliptical galaxies (Bertin et al. 2002).

6.6.3 Pressure anisotropy profiles

In our simulations the pressure anisotropy profiles follow the general trend expected for the process of collisionless collapse. In particular, the final configurations are characterized by an isotropic core, with $\alpha \approx 0$, while the outer regions have a strongly radially biased anisotropy (up to $\alpha = 2$). The transition region ($\alpha \approx 1$) is located around the half-mass radius (see column r_α/r_M in Table 6.3). Higher values of $2K_r/K_T$ are associated with lower values of r_α/r_M. For clumpy initial conditions (with the possible exception of those run with $N_C \geq 80$), the anisotropy profile $\alpha(r)$ is a monotonic increasing function of the radius. A curious feature is found for the results of collapse of uniform spheres (runs U). Here (see Fig. 6.6) the core is basically isotropic, with the region around the half-mass radius exhibiting an excess of *tangential* orbits (up to $\alpha \approx -0.4$). In the outer parts, but with a very sharp transition, the pressure profile becomes radially biased. In correspondence to the dip in α, where $\alpha < 0$, we note a clear feature in the density profile (see Fig. 6.6). Uniform spheres initialized with a very small particle number ($N < 10^4$) do not show this behavior; for them the pressure anisotropy rises quite regularly, although the profile is significantly affected by Poisson noise.

In conclusion, for all the clumpy C runs (again, we should mention, with the possible exception of those runs with $N_C \geq 80$), the anisotropy profile is represented extremely well by our models, with a mean absolute error ($\langle|\Delta\alpha|\rangle = (1/N_g)\sum_{i=1}^{N_g}|\alpha_{\rm sim}(r_i) - \alpha_{\rm model}(r_i)|$) typically around 0.1 but often as low as 0.05 (see Table 6.4).

To some extent, the final anisotropy profiles for clumpy initial conditions are found to be sensitive to the detailed choice of initialization. In other

words, runs starting from initial conditions with the same parameters, but with a different seed in the random number generator, give rise to slightly different profiles. In any case, the agreement between the simulation and the model profiles remains very good (see Figs. 6.7-6.10).

6.6.4 Comparison at the level of phase space

At the level of phase space, we have performed two types of comparison, one involving the energy density distribution $N(E)$ and the other based on $N(E, J^2)$. The chosen normalization factors are such that:

$$M = \int N(E)dE = \int N(E, J^2)dEdJ^2. \tag{6.2}$$

The energy distributions $N(E)$ that we find (see Fig. 6.7-6.10), qualitatively similar to those obtained in earlier investigations (see Fig. 2 in van Albada 1982 and Fig. 10 in Udry 1993), are characterized by an approximate exponential behavior at low energies ($N(E) \propto \exp(-aE)$) with a rapid cut-off near the origin, which is argued to go as $|E|^{5/2}$ because the potential is Keplerian in the outer parts (Udry 1993; see also the discussion by Jaffe 1987 and by Bertin & Stiavelli 1989). The final states of the simulations also show the presence of particles with positive energy, escaped from the system.

In Fig. 6.7 (bottom right frame) we plot the final energy density distribution for the simulation run C3.5 with respect to the predictions of the best-fit model identified from the study of the density and pressure anisotropy distributions. Similar plots are given in the following figures for other simulations. The agreement is very good ($\langle|\Delta E|\rangle \approx 0.2$, see Table 6.4), especially for the strongly bound particles. In particular, this means that we are correctly describing the innermost part of the system. The energy distribution for less bound particles (i.e. those associated mostly with the outer parts of the system) is less regular and sometimes presents a double peak (e.g., see Fig. 6.8), which obviously cannot be matched in detail by our models. This is an interesting example of the way some memory of the initial state can be preserved (the extra-peak is indeed related to the initial distribution of binding energies) and a direct sign of the incompleteness of violent relaxation.

Finally, at the deeper level of $N(E, J^2)$, simulations and models also agree rather well, as illustrated in the four panels of Figs. 6.11-6.14. For the cases shown, the distribution contour lines are in good agreement in the range from $E_{\rm min}$ to $E \approx -4$; however, the theoretical models show a peak located near the origin, not present in the simulations, which is related to the Jacobian factor arising from the transformation of the $f^{(\nu)}$ distribution function from the $(\vec{x}, \vec{w})$ to the (E, J^2) space.

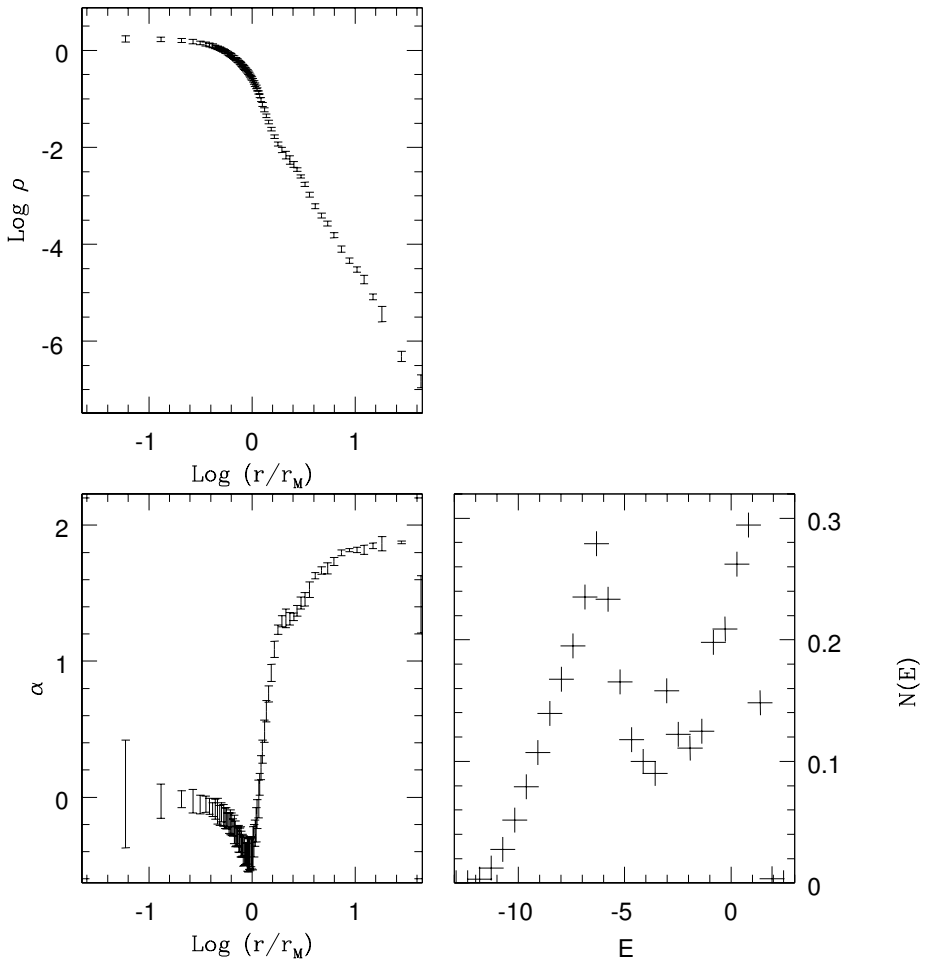

Figure 6.6: Density and anisotropy profiles (left frames) and energy density distribution (right frame) for simulation $U6.2$, starting from a homogeneous sphere. Note that in the vicinity of the half-mass radius the pressure anisotropy is *tangentially* biased.

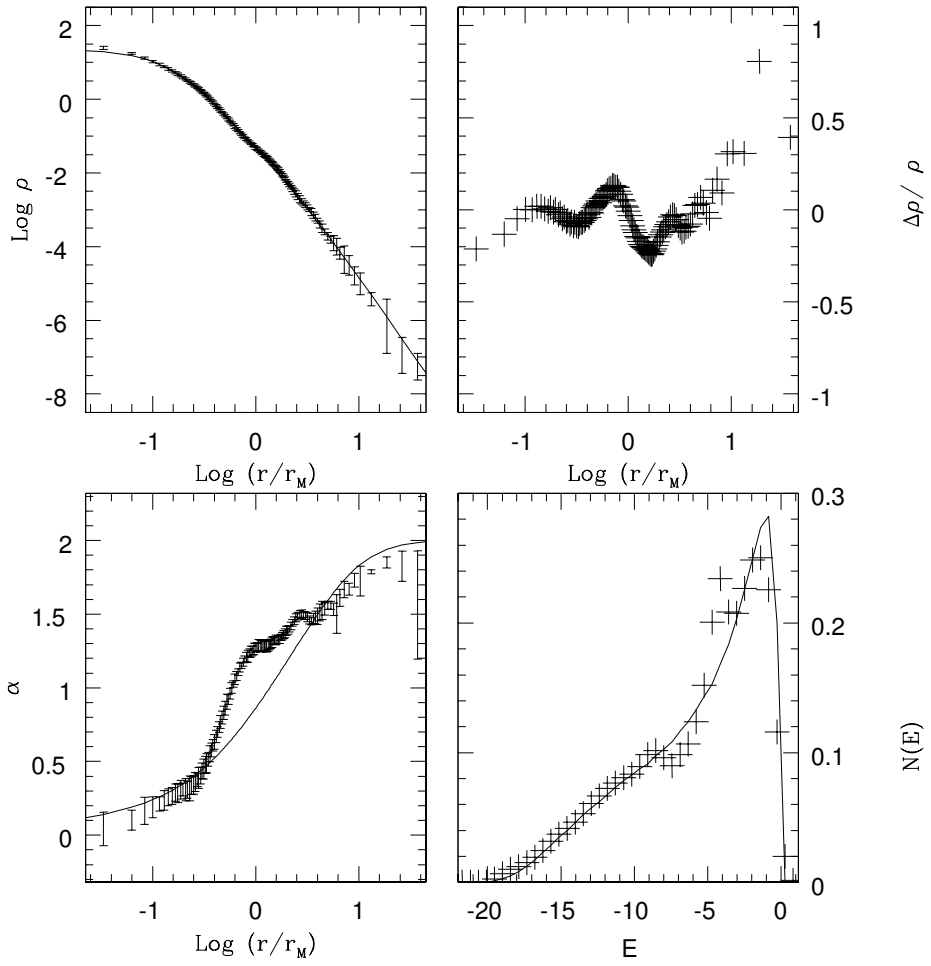

Figure 6.7: Comparison between the $C3.5$ simulation and the best-fit $f^{(\nu)}$ model $(1/2; 6.2)$. The top left panel represents the density as measured from the simulation (error bars) and the best-fit profile (line). The top right panel gives the residuals from the fit. At the bottom left, the anisotropy profile of the simulation (error bars) is compared with the best-fit profile (line); the bottom right frame illustrates the energy density distribution $N(E)$. The density ρ and the single-particle energy E are given in code units.

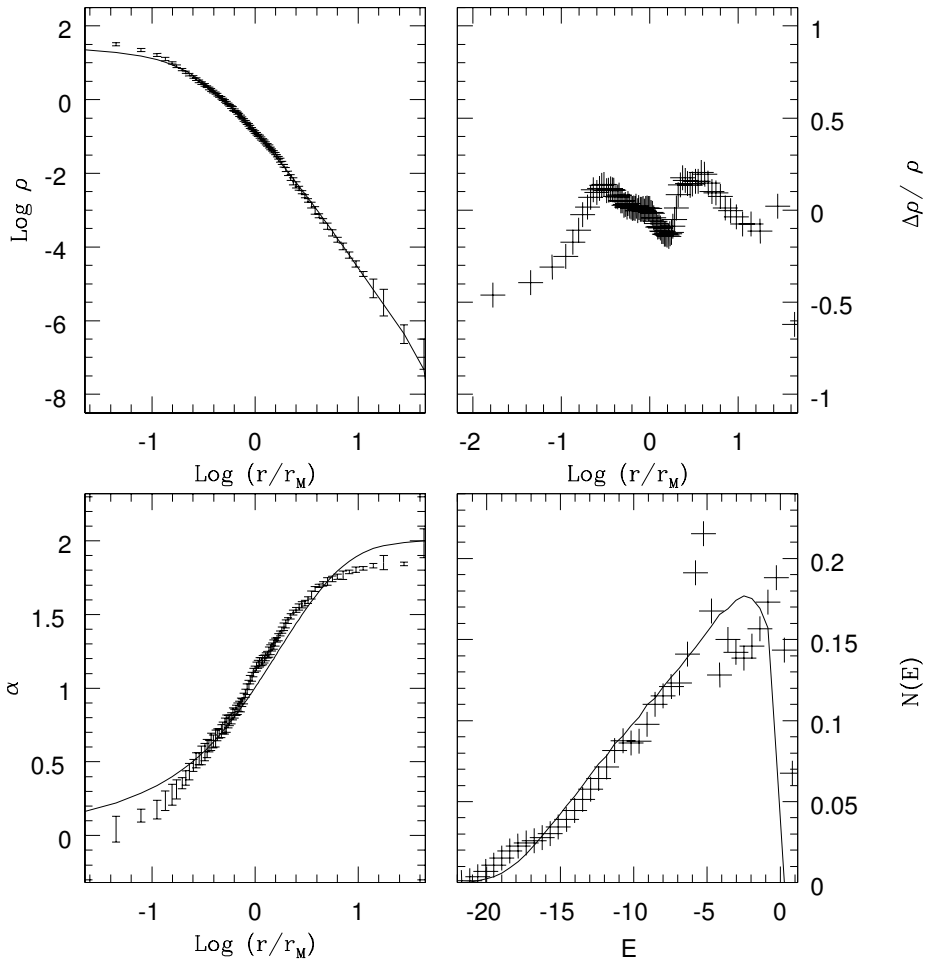

Figure 6.8: Comparison between the $C2.1$ simulation and the best-fit $f^{(\nu)}$ model $(1/2; 4.8)$, shown as in Fig. 6.7.

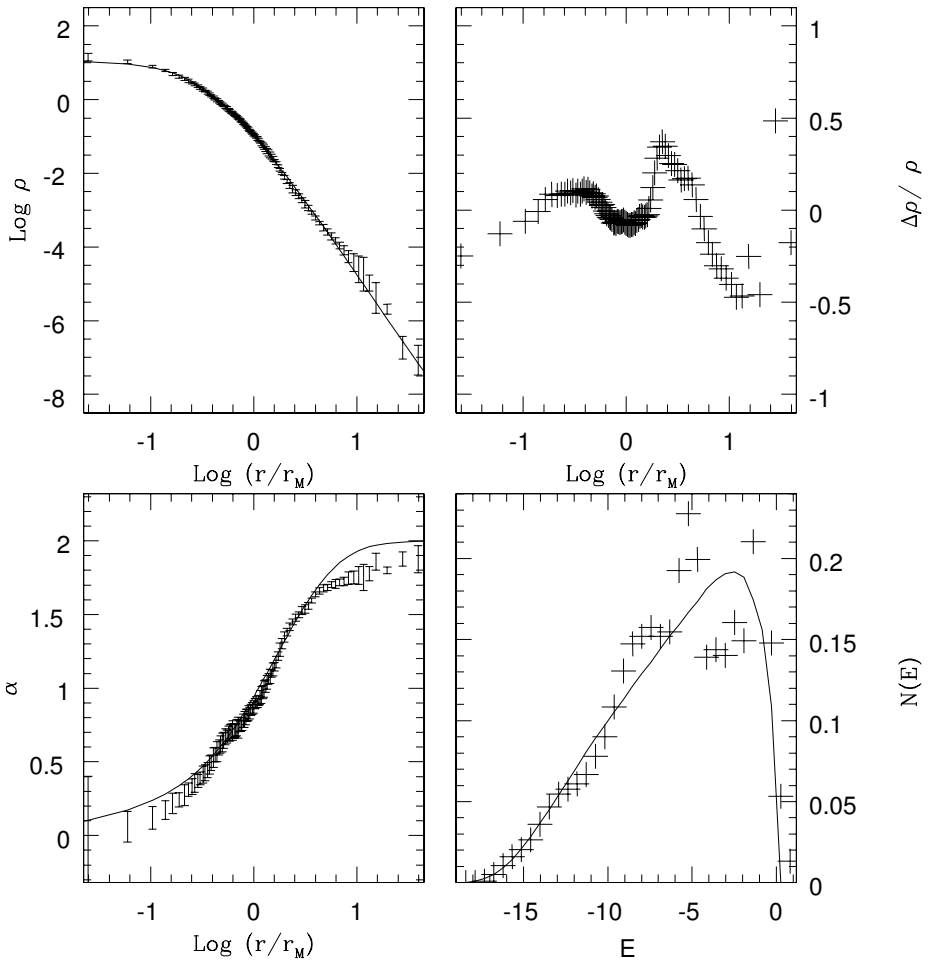

Figure 6.9: Comparison between the $C2.3$ simulation and the best-fit $f^{(\nu)}$ model $(5/8; 5)$, shown as in Fig. 6.7.

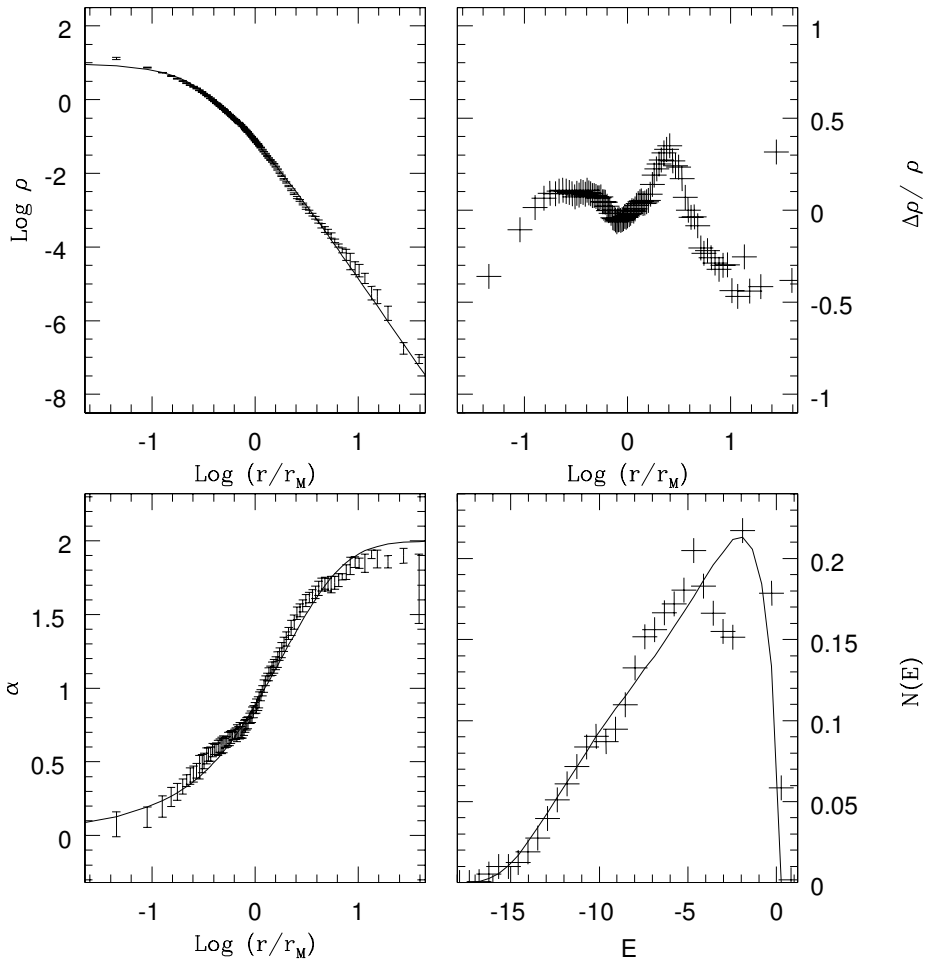

Figure 6.10: Comparison between the $C3.4$ simulation and the best-fit $f^{(\nu)}$ model $(5/8; 5.4)$, shown as in Fig. 6.7.

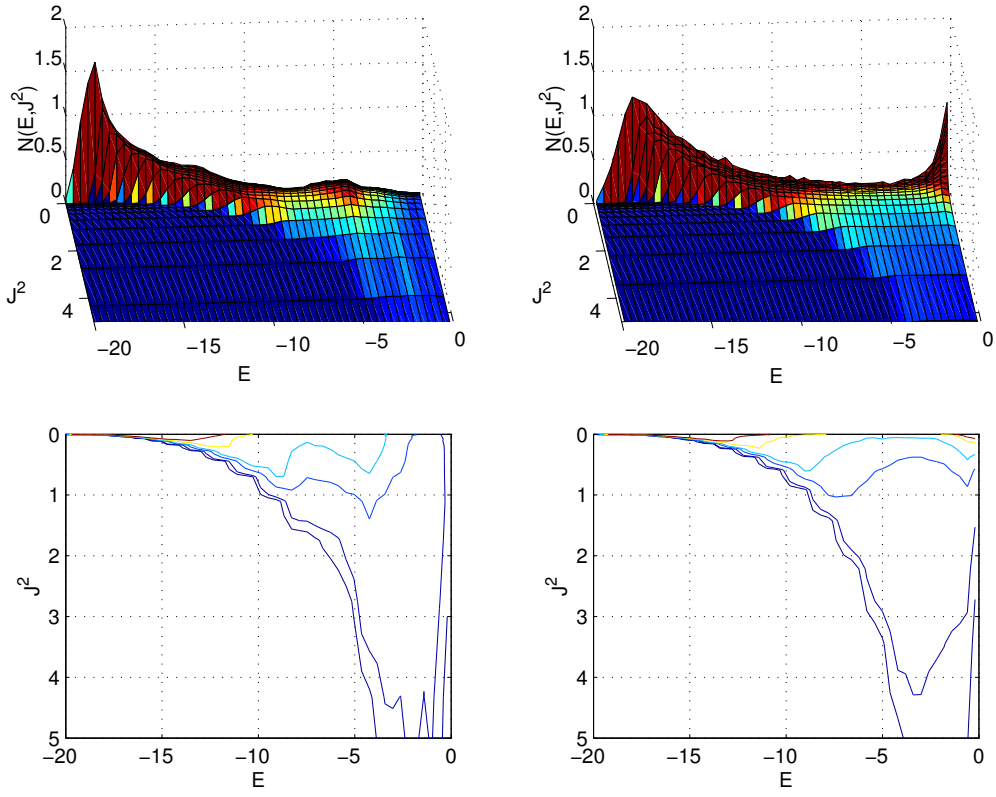

Figure 6.11: Final phase space density $N(E, J^2)$ (left column) for the simulation $C3.5$, compared with that of the best fitting $(1/2; 6.2)$ $f^{(\nu)}$ model (right column).

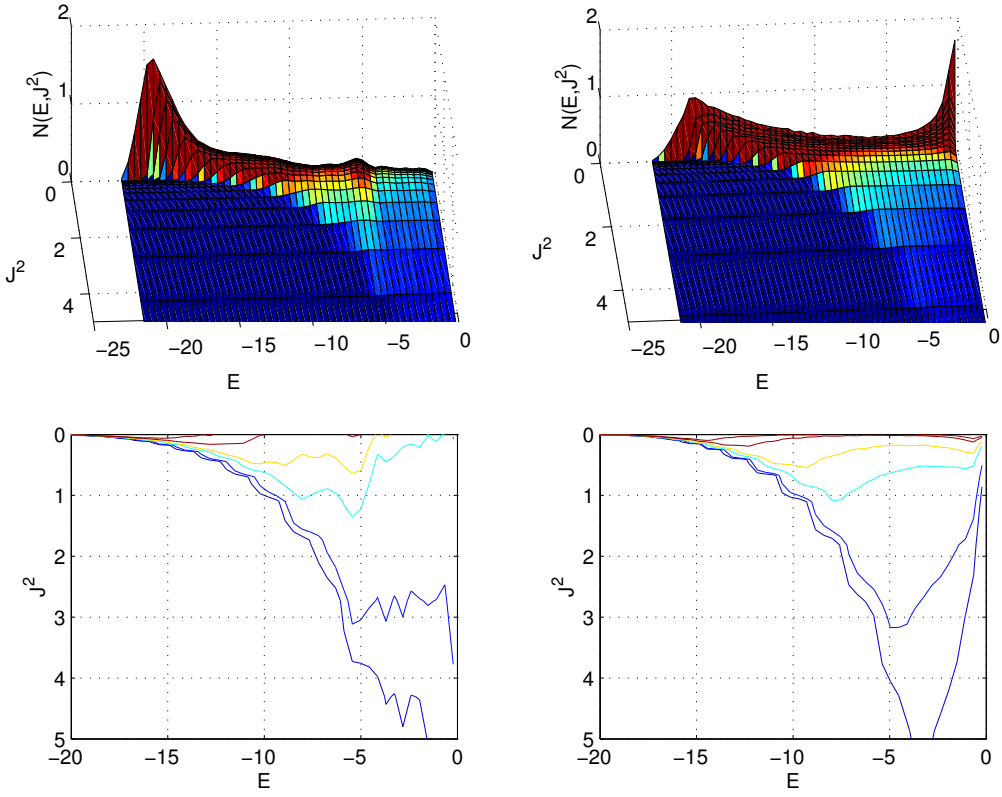

Figure 6.12: Final phase space density $N(E, J^2)$ (left column) for the simulation $C2.1$, compared with that of the best fitting $(1/2; 4.8)$ $f^{(\nu)}$ model (right column).

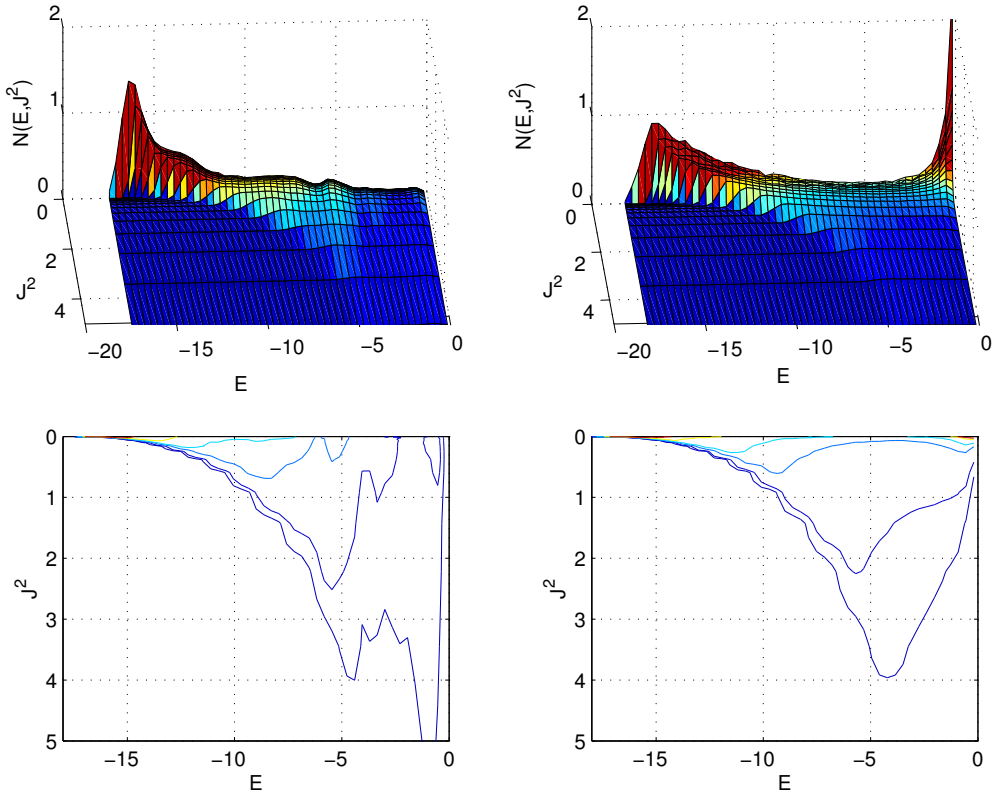

Figure 6.13: Final phase space density $N(E, J^2)$ (left column) for the simulation $C2.3$, compared with that of the best fitting $(5/8; 5.0)$ $f^{(\nu)}$ model (right column).

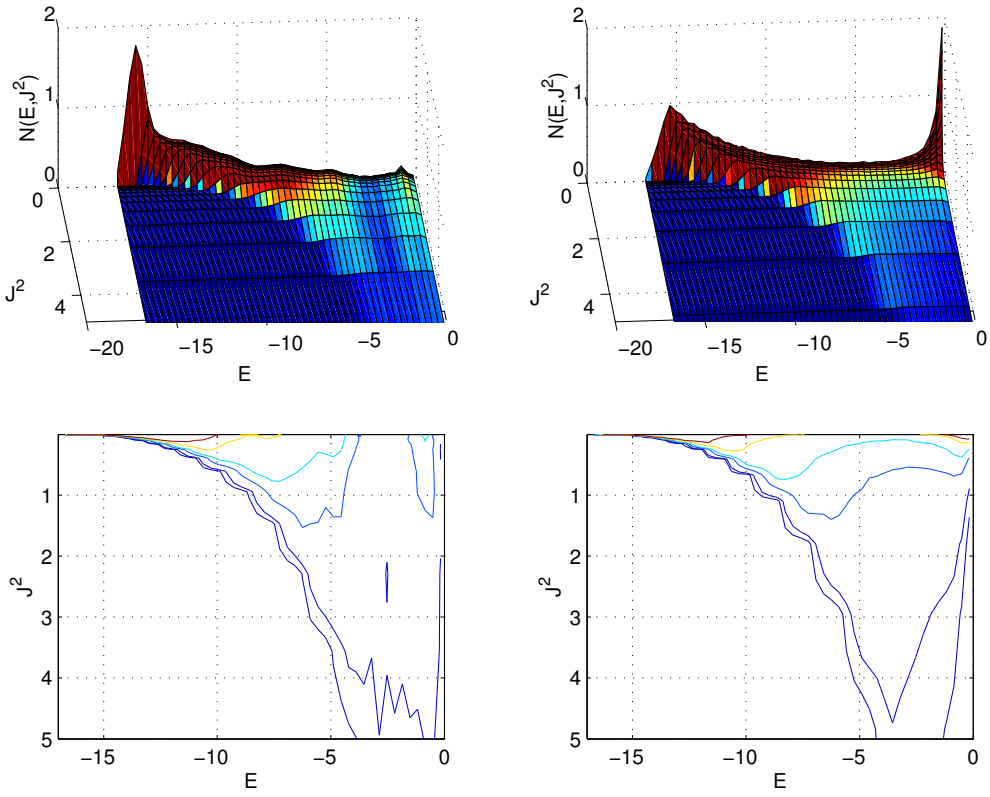

Figure 6.14: Final phase space density $N(E, J^2)$ (left column) for the simulation $C3.4$, compared with that of the best fitting $(5/8; 5.4)$ $f^{(\nu)}$ model (right column).

6.6.5 An additional test to characterize clumpy initial conditions

As an additional test to characterize the detailed effects of clumpiness, we studied the end-products of the $CV5.1$ and $CP5.2^*$ simulations, by comparing them with the $f^{(\nu)}$ models.

Although these two runs start from initial conditions rather different from our standard choice (cf. $C1$-$C3$), being homogeneous either in position ($CV5.1$) or in velocity ($CP5.2^*$) space, we note that they can be fitted very well by our family of models: $(3/4; 5.4)$ for $CV5.1$ and $(1; 6.2)$ for $CP5.2^*$ (with $\langle|\Delta\rho/\rho|\rangle \approx 0.1$). The good match at the level of the anisotropy profile $\alpha(r)$ and of the single-particle energy distribution also confirms, as discussed in the Appendix, that the requirement of clumpiness in phase space is a well posed characterization of the initial conditions. The two runs have the following behavior with respect to the Q-conservation: $\Delta Q = 0.02$ and final value $Q = 1.40$ for $CV5.1$; $\Delta Q = 0.01$ and final value $Q = 1.26$ for $CP5.2^*$.

In passing, we note that the $C4.4^*$ simulation, characterized by very small clumps, leads to a concentrated final density profile that is well reproduced by the $(1; 9.2)$ $f^{(\nu)}$ model (with $\langle|\Delta\rho/\rho|\rangle \approx 0.15$).

6.7 A quantitative measure of clumpiness

In order to characterize the degree of clumpiness present in the initial conditions of our simulations, we may consider, in the 6-dimensional phase space, the ratio $cl = \langle\rho^{(6)}_{\rm local}\rangle/\langle\rho^{(6)}\rangle$ of the mean local density around particles to the mean density.

We estimate the mean 6-dimensional density in phase space $\langle\rho^{(6)}\rangle$ by dividing the number of particles N by the typical total volume occupied. Since the large-scale structure in phase space is that of a sphere both in position and velocity space separately, we compute the total volume as the product of these two volumes. Each volume is calculated by assuming that the radius of each sphere is equal to the mean distance between two randomly chosen particles in the relevant space (position and velocity respectively); for example, for a homogeneous density distribution inside a sphere of unit radius, the radius determined from the adopted procedure would be ≈ 1.03.

The local density $\rho^{(6)}_{\rm local}$ (required for calculating the average used in the definition of cl) is computed by considering one particle and by counting the number of neighboring particles $N_{\rm local}$ within a six-dimensional small sphere of fixed radius r_s (and thus by assuming an equally weighted norm in the phase space for positions and velocities). The scale r_s is chosen in such a

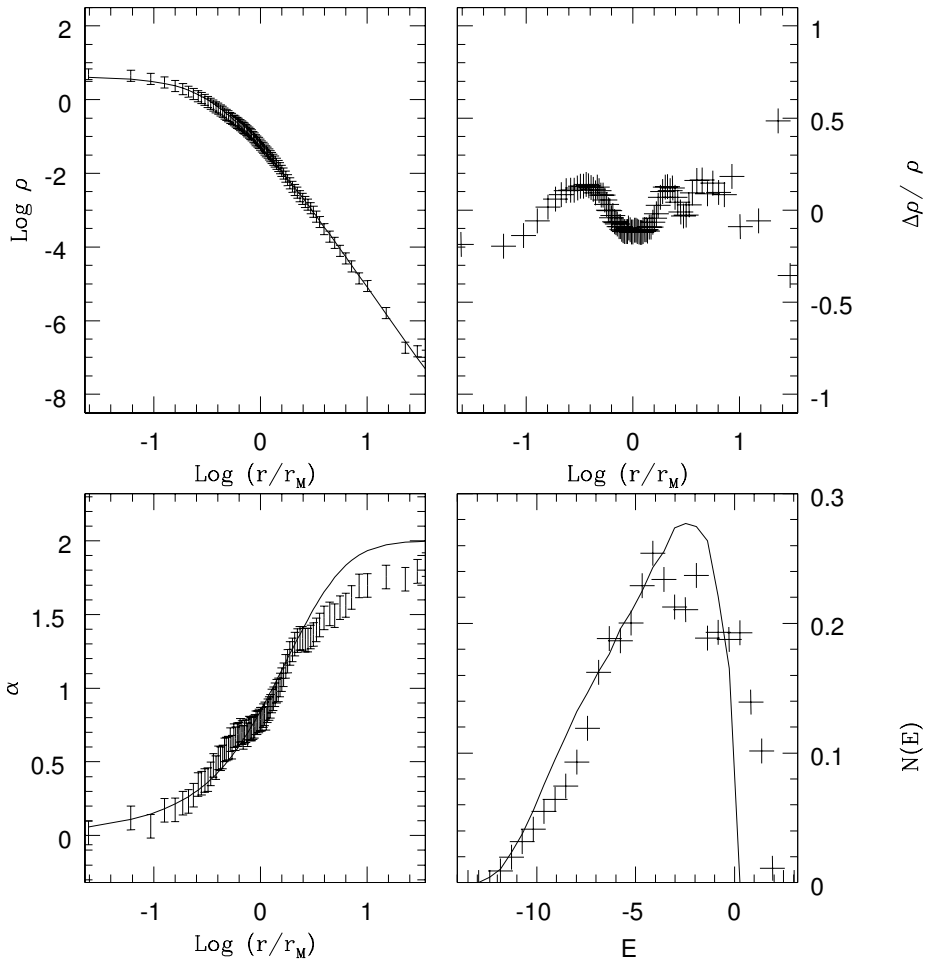

Figure 6.15: Comparison between the $CV5.1$ simulation and the best-fit $f^{(\nu)}$ model $(3/4; 5.4)$, shown as in Fig. 6.7.

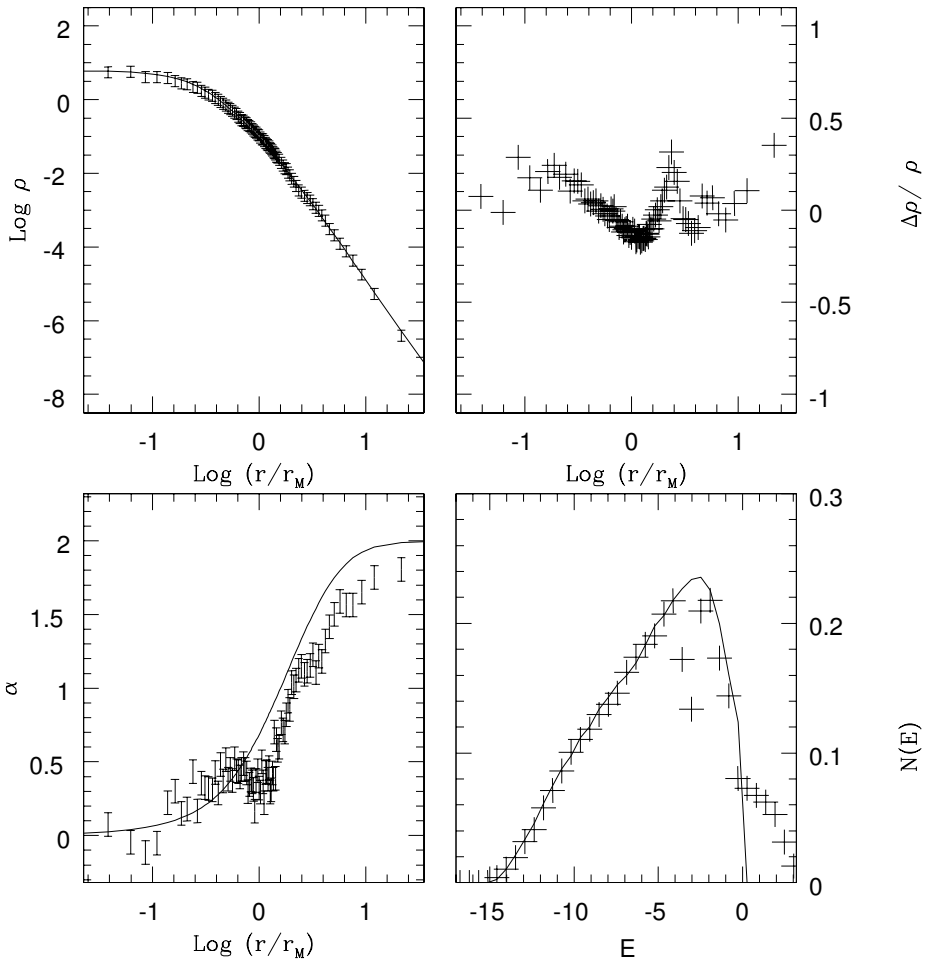

Figure 6.16: Comparison between the $CP5.2^*$ simulation and the best-fit $f^{(\nu)}$ model (1; 6.2), shown as in Fig. 6.7.

way that, on average, a small fixed fraction of the total number of particles is enclosed. We set this fraction to be $\xi = \langle N_{\rm local}\rangle/N \approx 1/250$. This choice ensures that we have, on average, a high filling factor within the small sphere, so that the effects of biases in the local density estimation arising from the coincidence of the center of the local sphere with the coordinates of a particle are unimportant (for a discussion on the construction of unbiased estimators for the local density, see also Casertano & Hut 1985).

The adopted scale r_s also acts as a cut-off scale to the clumpiness estimator cl, which is obviously insensitive to fluctuations at scales smaller than r_s. The dependence of the clumpiness estimator on ξ is illustrated in Fig. 6.17. Eventually, diagnostic tools such as $cl(\xi)$, as a measure of the initial spectrum of inhomogeneities in phase space, will help us establish a bridge toward initial conditions representative of the cosmological context (see also comments at the end of Sect. 6.3.1).

For our homogeneous initial conditions (simulations of type U) the value of the clumpiness estimator is $0.65 \lesssim cl \lesssim 1$, depending on the scale considered ($cl = 0.72$ for $\xi = 1/250$). Note that the value of cl can fall below unity, because of boundary effects. In contrast, for the cold clumpy initial conditions of type $C1$, $C2$, and $C3$ (with 10 and 20 clumps, and spatial filling factor $N_C \times R_C^3/R^3 \approx 1.25$), at $\xi = 1/250$ cl takes on values above 30, with typical values around 50 and peaks up to 100. For simulation $C4.4$ (with "small" clumps, and spatial filling factor $N_C \times R_C^3/R^3 = 0.027$), cl increases to 300. Conversely, cl decreases if the number of clumps is increased (down to $cl = 15$ for simulation $C4.3$ with 80 clumps and to $cl \approx 4.5$ for simulation $C4.5$ with 400 clumps).

With the numbers quoted above, we see that, at fixed numbers of particles, the clumpiness estimator cl varies with the number of clumps N_C used.

6.7.1 Clumpiness and mixing

As already anticipated in Sect. 6.4.3 and 6.4.4, for an efficient angular momentum mixing it is sufficient that clumpiness be present either in position or in velocity space. In fact, a simulation starting from uniform conditions in terms of positions but with clumpy structure in velocity space is bound to develop, after a few dynamical times, a significant clumpiness in position space (see Fig. 6.18), so that the single-particle angular momenta are well mixed at the end of the simulation (much as in the left panel of Fig. 6.3). This result confirms that our choice for quantifying the clumpiness of a given configuration by looking at the six-dimensional phase space is indeed reasonable.

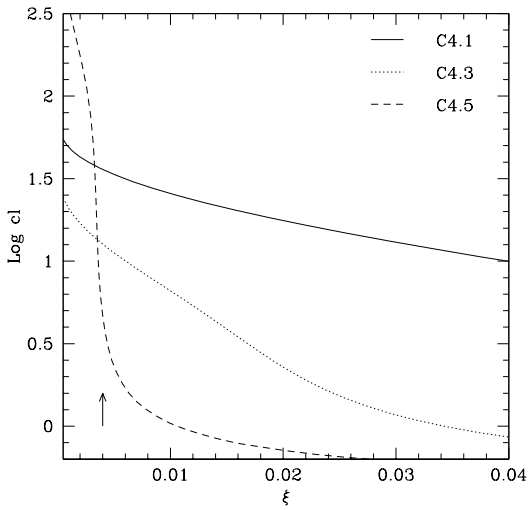

Figure 6.17: Clumpiness estimator cl as a function of $\xi = \langle N_{\rm local}\rangle/N$, for the initial conditions of simulations $C4.1$ (10 clumps), $C4.3$ (80 clumps), and $C4.5$ (400 clumps). The spatial filling factor is kept approximately constant ($N_C \times R_C^3/R^3 = 1.1 - 1.3$). The arrow indicates the scale $\xi = 1/250$ to which we refer most of our estimates.

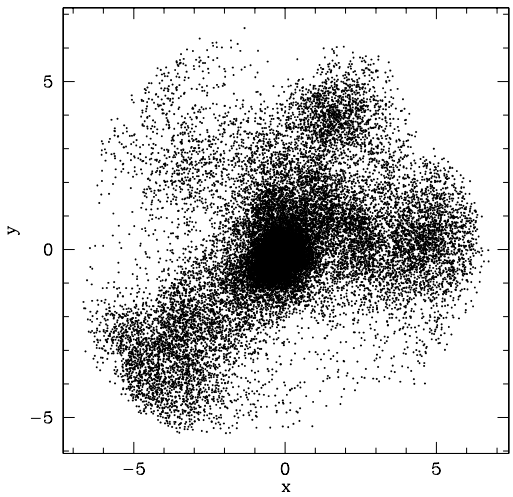

Figure 6.18: Spatial configuration at time $t = 4$ (i.e., after a few dynamical times, in the post-collapse phase) for the simulation $CV5.1$. Note the presence of clumps in position space.

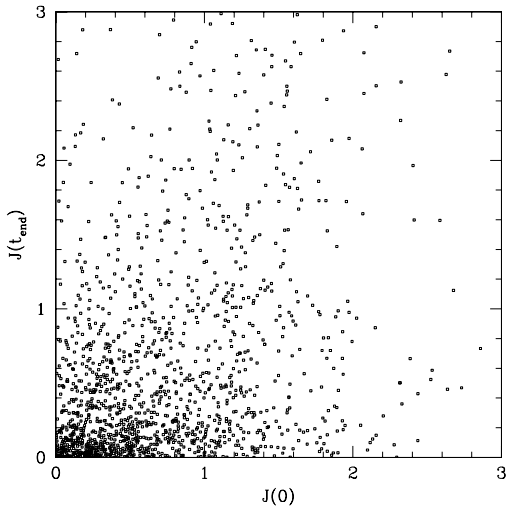

Figure 6.19: Scatter plot (final vs. initial values) for the single-particle specific angular momentum for the $CV5.1$ simulation. Units for J are pc^2/yr, see Sect. 6.2. A similar figure holds for the simulation $CP5.2^*$.

6.7.2 Separate fits to density and anisotropy profiles by means of simple analytic functions

Simple analytic descriptions of density profiles and, separately, of anisotropy profiles are often used in stellar dynamics, without a specific physical scenario of galaxy formation. For the density profile we may refer to:

$$\rho(r) = \frac{(3-\gamma)M}{4\pi} \frac{r_0}{r^\gamma (r+r_0)^{4-\gamma}}, \tag{6.3}$$

where $0 \leq \gamma < 3$ is a free parameter, and M and r_0 are a mass and length scale respectively (Dehnen 1993). As discussed in Paper I, it is no surprise to find that the case $\gamma = 2$ (Jaffe 1983) captures the general properties of the density profile obtained by the simulations at the 20% level. Curiously, when we fit the density distribution of some simulations by means of Equation (6.3), the best fitting index γ is very low, $\gamma \approx 0.1$ (see Fig. 6.20).

Similarly, for the anisotropy profile one might resort to the analytic distribution

$$\alpha(r) = 2\frac{r^2}{r^2 + r_\alpha^2}, \tag{6.4}$$

with r_α being a free scale (Merritt 1985). As shown in Fig. 6.20, the typical shape of the anisotropy profile reached at the end of the simulations is different.

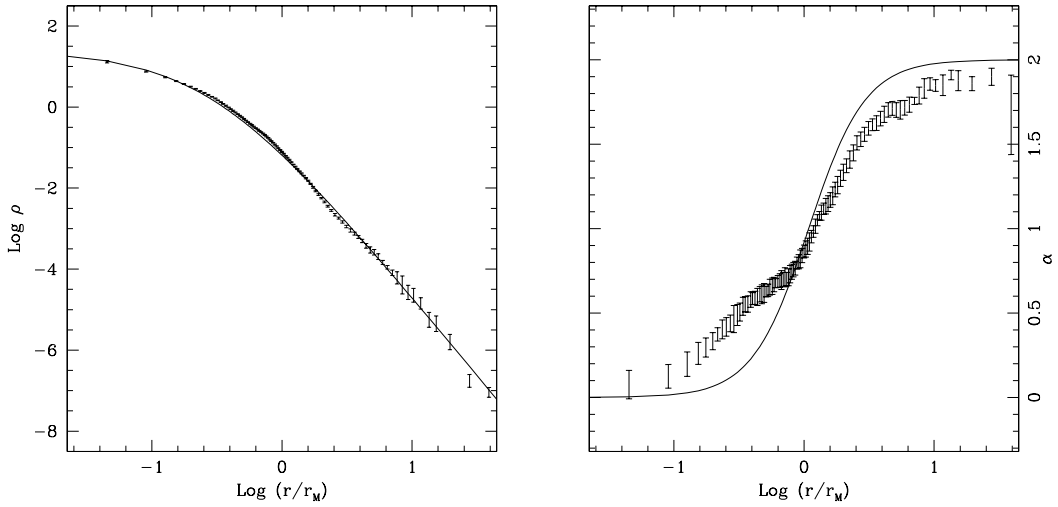

Figure 6.20: Density profile (left), fitted using Equation (6.3) with $\gamma = 0.11$, and anisotropy profile (right), fitted with Equation (6.4), for the simulation $C3.4$. Compare to the fit with the (5/8;5.4) $f^{(\nu)}$ model in Fig. 6.10.

6.8 Conclusions

In this Chapter we presented the results of an extensive set of numerical simulations starting from clumpy cold initial conditions. The collapse of a gravitational N-body system starting from cold initial conditions leads after a few dynamical times (i.e. $\approx 10^8$ years for a typical elliptical galaxy) to an equilibrium state with a dense isotropic core and a low concentration anisotropic halo which we showed here to be represented in quantitative detail by the $f^{(\nu)}$ models. The density profile from the simulations is matched over nine orders of magnitude with a relative error of 10%; in addition, the fit to the anisotropy profile is excellent (mean error of 5%) and the models correctly reproduce the phase space distributions in energy and angular momentum ($N(E)$ and $N(E, J^2)$).

From the numerical simulations we have been able to measure directly the conservation of Q, one key assumption that leads to the construction of the distribution function of the $f^{(\nu)}$ models (Stiavelli & Bertin 1987). Generally this conservation is of the order 20% for low values of ν (i.e. $\nu \approx 1/2$). Interestingly also the best fitting models of the end products of the simulations tend to have $\nu \approx 1/2$, with a very limited dispersion (see Table 6.4. These two observations, in addition to the observational evidence that also $\nu \approx 1/2$ is preferred for fitting the photometric and kinematic profile of *NGC3379* give a strong empirical support to the claim that the f^{ν} models with $\nu = 1/2$

are a one parameter equilibrium sequence, that for violently collapsed gravitational systems plays a role similar to that played by the King models for truncated stellar systems relaxed due to collisional effects.

Table 6.1: Initial conditions for the simulations. From the first column simulation identifier, the number of particles N, the number of clumps N_C, the initial virial ratio u, the initial values of the shape parameters ϵ_0 and η_0, and the initial concentration $C_{\rho 0}$. For the exact definitions and for the general characteristics of the groups, see Sect. 6.3.2. Four simulations, marked by a *, have been carried out with *GyrFalcOn* (Dehnen 2000).

	N	N_C	u	ϵ_0	η_0	$C_{\rho 0}$
$C1.1$	10^5	10	0.275	0.83	0.70	3.0
$C1.2$	10^5	10	0.25	0.83	0.70	3.0
$C1.3$	10^5	10	0.225	0.83	0.70	3.0
$C1.4$	10^5	10	0.20	0.83	0.70	3.0
$C1.5$	10^5	10	0.175	0.83	0.70	3.0
$C1.6$	10^5	10	0.15	0.83	0.70	3.0
$C1.7$	10^5	10	0.125	0.83	0.70	3.0
$C1.8$	10^5	10	0.1	0.83	0.70	3.0
$C1.9$	10^5	10	0.075	0.83	0.70	3.0
$C1.10$	10^5	10	0.05	0.83	0.70	3.0
$C2.1$	$8 \cdot 10^5$	20	0.23	0.93	0.73	2.8
$C2.2$	$8 \cdot 10^5$	20	0.17	0.93	0.73	2.8
$C2.3$	$8 \cdot 10^5$	20	0.12	0.93	0.73	2.8
$C2.4$	$8 \cdot 10^5$	20	0.06	0.93	0.73	2.8
$C3.1$	$8 \cdot 10^5$	20	0.08	0.95	0.91	2.2
$C3.2$	$8 \cdot 10^5$	20	0.18	0.86	0.80	2.6
$C3.3$	$8 \cdot 10^5$	20	0.15	0.84	0.70	3.1
$C3.4$	$8 \cdot 10^5$	20	0.23	0.88	0.73	2.0
$C3.5$	$8 \cdot 10^5$	20	0.15	0.95	0.88	3.7
$C3.6$	$8 \cdot 10^5$	10	0.15	0.86	0.80	3.7
$C4.1$	10^5	10	0.15	0.87	0.80	2.8
$C4.1^*$	10^5	10	0.15	0.87	0.80	2.8
$C4.1_h$	10^5	10	0.15	0.87	0.80	2.8
$C4.2$	10^5	20	0.25	0.75	0.63	1.5
$C4.3$	10^5	80	0.14	0.90	0.77	1.9
$C4.3^*$	10^5	80	0.14	0.90	0.77	1.9
$C4.4^*$	10^5	80^+	0.15	0.85	0.78	2.0
$C4.5$	10^5	400	0.23	0.99	0.95	0.8
$C4.5_h$	10^5	400	0.23	0.99	0.95	0.8
$CV5.1$	10^5	10	0.23	1.00	1.00	1.0
$CP5.2^*$	10^5	40	0.15	0.81	0.78	0.7
$U6.1$	$8 \cdot 10^5$	N/A	0.10	1.00	1.00	1.0
$U6.2$	$8 \cdot 10^5$	N/A	0.19	1.00	1.00	1.0
$U6.3$	$8 \cdot 10^5$	N/A	0.29	1.00	1.00	1.0
$U6.4$	$8 \cdot 10^5$	N/A	0.39	1.00	1.00	1.0
$S4.2$	10^5	N/A	0.25	1.00	0.99	1.5
$S4.3$	10^5	N/A	0.15	1.00	1.00	1.9

Table 6.3: Final configurations for the simulations of collisionless collapse listed in Table 6.1. The column entries are described in Sect. 6.4. Note that the anisotropy profile in homogeneous simulations can be non-monotonic; this is indicated by †. All simulations of type $C1$ and $C2$ start from identical initial conditions within each series, except for a constant scaling of velocities. The quantity ΔQ is referred to $\nu = 5/8$ in simulation $CV5.1$, to $\nu = 1$ in simulation $U6.1$ and to $\nu = 3/4$ in simulation $U6.2$; this is indicated by $^{\#}$.

	ΔM	ΔQ	C_ρ	κ	r_α/r_M	ϵ	η
$C1.1$	0.00	0.13	570	1.61	1.02	0.91	0.73
$C1.2$	0.002	0.17	600	1.60	0.94	0.91	0.74
$C1.3$	0.01	0.20	680	1.59	0.94	0.90	0.76
$C1.4$	0.01	0.24	790	1.57	0.88	0.95	0.79
$C1.5$	0.02	0.30	720	1.52	0.88	0.96	0.81
$C1.6$	0.03	0.38	820	1.50	0.93	0.99	0.80
$C1.7$	0.04	0.44	760	1.47	0.92	0.97	0.78
$C1.8$	0.05	0.52	850	1.53	0.87	0.96	0.79
$C1.9$	0.06	0.66	1130	1.67	0.75	0.97	0.75
$C1.10$	0.08	0.72	1090	1.74	0.79	0.94	0.69
$C2.1$	0.01	0.13	110	1.52	1.49	0.87	0.78
$C2.2$	0.02	0.25	160	1.62	1.24	0.88	0.78
$C2.3$	0.03	0.4	270	1.70	0.83	0.81	0.69
$C2.4$	0.07	0.5	520	1.76	0.74	0.81	0.63
$C3.1$	0.003	0.47	1690	1.99	0.44	0.90	0.73
$C3.2$	0.001	0.26	1250	1.85	0.55	0.93	0.70
$C3.3$	0.04	0.57	430	1.60	1.34	0.92	0.71
$C3.4$	0.02	0.23	500	1.65	1.15	0.93	0.81
$C3.5$	0.005	0.24	950	1.73	0.57	0.96	0.72
$C3.6$	0.005	0.27	690	1.79	0.75	0.80	0.77
$C4.1$	0.005	0.27	440	1.77	0.83	0.80	0.73
$C4.1^*$	0.01	0.27	360	1.68	0.97	0.89	0.74
$C4.1_h$	0.00	0.18	240	1.86	0.51	0.86	0.83
$C4.2$	0.12	0.10	160	1.40	1.65	0.90	0.78
$C4.3$	0.10	$<$0.01	70	1.60	1.53	0.84	0.74
$C4.3^*$	0.07	0.15	70	1.50	1.56	0.86	077
$C4.4^*$	0.04	0.4	4000	1.15	5.30	0.98	0.96
$C4.5$	0.125	0.02	20	1.20	1.74	0.96	0.95
$C4.5_h$	0.10	0.05	15	1.16	1.58	0.99	0.97
$CV5.1$	0.12	$0.02^{\#}$	90	1.55	1.50	0.91	0.75
$CP5.2^*$	0.10	0.01	590	1.33	2.20	0.83	0.76
$U6.1$	0.33	$0.29^{\#}$	8	1.10	$1.60^{\dagger}$	1.00	1.00
$U6.2$	0.20	$0.01^{\#}$	6	1.10	$1.56^{\dagger}$	1.00	1.00
$U6.3$	0.06	0.14	9	1.11	$1.50^{\dagger}$	1.00	1.00
$U6.4$	0.00	0.09	8	1.11	$1.60^{\dagger}$	1.00	1.00
$S4.2$	0.00	0.09	506	2.13	0.29	0.99	0.98
$S4.3$	0.10	0.26	50	1.50	0.97	0.98	0.98

Table 6.4: Best fit $f^{(\nu)}$ models for the set of high resolution runs (series $C2$ and $C3$). The various columns give: run identifier, model identifier, mean value of the absolute relative deviations from the density of the simulations, mean value of the absolute deviations in the pressure anisotropy profile, mean value of the absolute relative deviations in the energy distribution, and final value of Q.

	$f^{(\nu)}$	$\langle\lvert\Delta\rho/\rho\rvert\rangle$	$\langle\lvert\Delta\alpha\rvert\rangle$	$\langle\lvert\Delta E/E\rvert\rangle$	Q
$C2.1$	(1/2;4.8)	0.11	0.07	0.23	1.24
$C2.2$	(1/2;4.8)	0.11	0.06	0.22	1.33
$C2.3$	(5/8;5.0)	0.12	0.06	0.21	1.35
$C2.4$	(7/8,5.6)	0.14	0.08	0.23	1.33
$C3.1$	(3/8;5.6)	0.10	0.22	0.18	1.33
$C3.2$	(3/8;5.4)	0.11	0.19	0.22	1.26
$C3.3$	(1/2;5.2)	0.17	0.16	0.20	1.64
$C3.4$	(5/8;5.4)	0.12	0.05	0.18	1.40
$C3.5$	(1/2;6.2)	0.09	0.20	0.15	1.35
$C3.6$	(3/8;5.2)	0.13	0.05	0.20	1.35

Chapter 7

Conclusions and future perspectives

[1] In this Thesis we have concentrated on nearly spherical, one-component stellar systems. As is well known, in spite of these restrictions, the equations of stellar dynamics allow almost complete freedom in the construction of self-consistent dynamical models, with the only requirement that they should be supported by a positive definite (but otherwise arbitrary) function of E and J, as a distribution function in phase space. Therefore, the full range of self-consistent one-component spherical stellar dynamical models is enormous. Most likely, the majority of these models have little to do with the systems that have been realized in nature. The main idea at the basis of the present work is to combine clues from N-body simulations and from statistical arguments so as to pinpoint, among the enormous variety of in principle acceptable dynamical models, those few that, because of their physical justification, have a chance of matching the properties of interesting classes of numerical simulations and of observed stellar systems.

Some interesting clues had been noted earlier. With the aim of summarizing the main properties of incomplete violent relaxation during collisionless collapse, it was discovered (Stiavelli & Bertin 1987) that, by arguing that a third quantity Q (in addition to total energy and number of stars) should be included among the relevant constraints in the extremization of the Boltzmann entropy, the most probable and thus physically justified distribution function $f^{(\nu)}$ leads to models that are in *general qualitative* correspondence with the products of collisionless collapse found in numerical simulations and with the observed luminosity profiles of bright elliptical galaxies.

In this Thesis we have demonstrated that the $f^{(\nu)}$ models are able to

[1] These considerations have been published in Trenti et al. (2005)

match in *surprising quantitative detail* the results of our numerical simulations. At the same time, the $f^{(\nu)}$ models exhibit projected density profiles that are well represented by the $R^{1/n}$ law (generally with $n \approx 4$; the residuals from the fit are within 0.1 magnitudes in a radial range of from 0.1 to 10 effective radii; see also Chapter 5). Therefore, we have demonstrated that the $f^{(\nu)}$ models, as well as the end products of the collapse simulations, are relevant to the description of the stellar distribution of elliptical galaxies. This correspondence is even more remarkable if we recall that, from the results established in the last decades, dark matter should play a dominant role in the structure of galaxies, while our approach neglects, so far, some important ingredients among which is the presence of a massive, possibly diffuse dark halo.

Independently of stellar dynamical modeling, our simulations have shown that clumpy initial configurations allow an efficient re-distribution of the angular momenta of the individual particles during collapse: such efficient phase space mixing is precisely the main condition required for a successful application of the statistical arguments that lead to the construction of the $f^{(\nu)}$ family of distribution functions. In the past (e.g., see van Albada 1982; May & van Albada 1984; Merritt & Aguilar 1985; Londrillo et al. 1991) it has been noted that cold collapses, within a wide range of initial density profiles, generate quasi-equilibrium systems with approximate $R^{1/4}$ profiles. Here we confirm that the best match to approximate $R^{1/4}$ profiles is obtained from initiallly clumpy configurations. It thus appears that collapses starting from artificially uniform and spherically symmetric initial conditions retain too much memory of the initial conditions and are unable to evolve into a universal density distribution. Therefore, it is interesting to find that precisely those initial conditions that look more plausible and realistic from the physical point of view lead to end products able to match the stellar distribution of observed systems in detail. We may then conclude that collisionless collapse from clumpy initial conditions followed by violent relaxation is indeed a formation mechanism relevant to elliptical galaxies.

If we now take the point of view of stellar dynamical modeling and examine the foundation of the $f^{(\nu)}$ family of models, we note that many collapse simulations show Q-conservation at the 20% level or better (e.g., $C1.1$, $C2.1$ and $C3.4$). But it is even more surprising to find that the end products can be fitted so well by the $f^{(\nu)}$ models. Such good fits make it clear that the assumption of Q conservation narrows down the very wide range of self-consistent dynamical models to precisely those few systems whose properties match both observed systems and the end products of collisionless collapse. One must conclude that the value of the Q-conservation assumption goes beyond mere "physical plausibility" and "mathematical convenience": it does

serve as a sound physical basis for the construction of dynamical models of partially relaxed stellar systems.

We should emphasize that such detailed *quantitative* correspondence with observed systems and with the end products of collisionless collapse comes as a complete surprise, because the two parameters that can be varied within the $f^{(\nu)}$ family of models (i.e., ν and Ψ) leave very little freedom with respect to density and anisotropy profiles (see Chapter 5). Especially noteworthy are not only the match of the density profile over nine orders of magnitude but also the excellent agreement of the velocity anisotropy profiles between the $f^{(\nu)}$ models and several end products of collapse from clumpy initial conditions (see Figs. 6.7-6.10 and Table 6.4).

Yet one cannot claim that the $f^{(\nu)}$ models give a fully satisfactory description of the phase space structure of systems produced via incomplete violent relaxation. In fact, the associated $N(E, J^2)$ distribution is characterized by singular behavior near the origin in the (E, J^2) plane, which is not present in the end-states of the simulations. In spite of this discrepancy between models and end-products of the simulations, the integrated properties (e.g., $N(E)$, $\alpha(r)$ and $\rho(r)$) are very well reproduced. This confirms the fact that a variety of different distributions in phase space can lead to the same integrated properties. In this respect it appears that, if we refer to the extreme outer parts of the system (with $r \gg r_M$, and $E \to 0$) the previously studied f_∞ models (Bertin & Stiavelli 1984), with their regular distribution function $f(E, J^2) \approx |E|^{3/2}$ at low values of $|E|$, might still have an advantage over the $f^{(\nu)}$ models.

Another interesting (although partly known) result of the present work is that the velocity distributions of the end products of the collapse simulations and of the best fitting models possess, in many cases, a rather strong radial anisotropy. In some of the collapse simulations we see clear signs that the radial-orbit instability has been active (as indicated by the correlation between final ellipticity η and anisotropy content $2K_r/K_T$; cf. Fig. 6.2), resulting in end products that are close to the threshold for the onset of the radial-orbit instability. In general, systems that are unstable with respect to the radial-orbit instability should evolve into marginally stable systems (see also the study of the unstable $(1; 3.2)$ $f^{(\nu)}$ model in Sect. 4.2). In view of the good correspondence between the results of the formation processes studied in this paper and important observed properties of elliptical galaxies, we may argue that ellipticals are also likely to lie close to the threshold of radial-orbit instability. This would happen if elliptical galaxies, during their formation process, indeed went through a collisionless phase characterized by strong radial motions (such as collapse or head-on mergers). We plan to better quantify this connection by extending the study to two-component

models and collapses, also starting from a power spectrum of perturbations representative of cosmological initial conditions.

The last remark brings us naturally to one final comment. We recall that, since collisionless dynamics is scale-free, the results obtained here can also be interpreted as relevant to the description of the collapse of dark matter halos. Clearly, since we do not include the effects related to the general Hubble expansion and we do not initialize our clumpy conditions in terms of the power spectrum of perturbations appropriate for a given cosmological epoch, a direct comparison between our set of numerical experiments and the profiles of dark matter halos obtained in ΛCDM simulations (Navarro et al. 1997; Moore et al. 1998) would not be justified. Still, our experiments can be considered as one example of final equilibrium realizations of a dark halo, when initial conditions are varied outside the prescriptions consistent with the currently accepted cosmological framework (see also Lemson 1995). If we now go back to our interpretation in terms of the $f^{(\nu)}$ models, it is noteworthy to point out that, although the density profile of the $f^{(\nu)}$ models falls off as $1/r^4$ at large radii, in the inner parts that might correspond to the regions inside the virial radius (for a definition see Navarro et al. 1997), the density goes approximately as $1/r^{3.2}$ (see Sect. 5.3.1), which is very close to the reported $1/r^3$ value for cosmological simulations (Navarro et al. 1997; Moore et al. 1998). Since the outskirts of dark matter halos are "still collapsing", and thus their dynamical conditions are different from those under which we derived the $f^{(\nu)}$ models, this agreement appears surprisingly good and suggests further investigations.

Bibliography

Abramowitz, M. & Stegun, I. 1965, Handbook of Mathematical Functions (Dover, New York)

Aguilar, L. A. & Merritt, D. 1990, ApJ, 354, 33

Allen, A. J., Palmer, P. L., & Papaloizou, J. 1990, MNRAS, 242, 576

Antonov, V. 1962, Vestnik Leningr. Univ., 19, 96

Arad, I. & Johansson, P. 2005, submitted to MNRAS

Ascasibar, Y. & Binney, J. 2004, MNRAS, 684

Barnes, J. 1985, in IAU Symp. 113: Dynamics of Star Clusters, 297–299

Barnes, J. & Hut, P. 1986, Nature, 324, 446

Barnes, J., Hut, P., & Goodman, J. 1986, ApJ, 300, 112

Bekenstein, J. D. 2004, Phys. Rev. D, 70, 083509

Bendinelli, O., Ciotti, L., & Parmeggiani, G. 1993, A&A, 279, 668

Berman, R. H. & Mark, J. W.-K. 1977, ApJ, 216, 257

Berntsen, J., T., E., & Genz, A. 1991, ACM Tran.Mat.Soft., 17, 437

Bertin, G. 2000, Dynamics of galaxies (Dynamics of galaxies / Giuseppe Bertin. New York : Cambridge University Press)

Bertin, G., Ciotti, L., & Del Principe, M. 2002, A&A, 386, 149

Bertin, G., Liseikina, T., & Pegoraro. 2003, A&A, 405, 73

Bertin, G., Pegoraro, F., Rubini, F., & Vesperini, E. 1994, ApJ, 434, 94

Bertin, G., Saglia, R. P., & Stiavelli, M. 1992, ApJ, 384, 423

Bertin, G. & Stiavelli, M. 1984, A&A, 137, 26

Bertin, G. & Stiavelli, M. 1989, ApJ, 338, 723

Bertin, G. & Stiavelli, M. 1993, Reports on Progress in Physics, 56, 493

Bertin, G. & Trenti, M. 2003, Ap.J., 584, 729

Binney, J. & Tremaine, S. 1987, Galactic dynamics (Princeton, NJ, Princeton University Press, 1987, 747 p.)

Binney, J. J. & Evans, N. W. 2001, MNRAS, 327, L27

Boily, C. M., Athanassoula, E., & Kroupa, P. 2002, MNRAS, 332, 971

Bonnor, W. B. 1956, MNRAS, 116, 351

Bunker, A. J., Stanway, E. R., Ellis, R. S., & McMahon, R. G. 2004, MNRAS, 355, 374

Capaccioli, M., Held, E. V., Lorenz, H., & Vietri, M. 1990, AJ, 99, 1813

Carollo, C. M., de Zeeuw, P. T., & van der Marel, R. P. 1995, MNRAS, 276, 1131

Casertano, S. & Hut, P. 1985, ApJ, 298, 80

Chandrasekhar, S. 1942, Physical Sciences Data

Chandrasekhar, S. 1943, ApJ, 97, 255

Chandrasekhar, S. & Woltjer, L. 1958, Proc. Natl. Acad. Sci. US, 44, 285

Chavanis, P. H. 2002, A&A, 386, 732

Cimatti, A., Daddi, E., Renzini, A., et al. 2004, Nature, 430, 184

Ciotti, L. 2000, Lecture Notes on Stellar Dynamics (Scuola Normale Superiore, Pisa Italy, 2000, 160 pp.)

Ciotti, L. & Bertin, G. 1999, A&A, 352, 447

Ciotti, L. & Binney, J. 2004, MNRAS, 351, 258

Cuperman, S., Harten, A., & Lecar, M. 1971, Ap. Space Sci,, 13, 425

de Vaucouleurs, G. 1948, Annales d'Astrophysique, 11, 247

de Vaucouleurs, G. 1953, MNRAS, 113, 134

de Vaucouleurs, G. & Capaccioli, M. 1979, ApJS, 40, 699

de Zeeuw, P. T., Bureau, M., Emsellem, E., et al. 2002, MNRAS, 329, 513

Dehnen, W. 1993, MNRAS, 265, 250

Dehnen, W. 2000, ApJL, 536, L39

Dehnen, W. 2001, MNRAS, 324, 273

Dehnen, W. 2002, J. Comp. Phys., 179, 27

Djorgovski, S. & Davis, M. 1987, Ap.J., 313, 59

Djorgovski, S. & Meylan, G. 1994, A.J., 108, 1292

Dodelson, S. 2003, Modern cosmology (Modern cosmology / Scott Dodelson. Amsterdam (Netherlands): Academic Press, 2003, 440 pp.)

Dressler, A., Lynden-Bell, D., Burstein, D., et al. 1987, Ap.J., 313, 42

Efstathiou, G., Davis, M., White, S. D. M., & Frenk, C. S. 1985, ApJS, 57, 241

Faber, S. M. & Jackson, R. E. 1976, Ap.J., 204, 668

Fontana, A., Pozzetti, L., Donnarumma, I., et al. 2004, A&A, 424, 23

Fridman, A. M. & Poliachenko, V. L. 1984, Physics of gravitating systems (New York: Springer, 1984)

Gerhard, O. 1991, MNRAS, 250, 812

Gerhard, O. 1993, MNRAS, 265, 213

Gerhard, O., Kronawitter, A., Saglia, R. P., & Bender, R. 2001, AJ, 121, 1936

Ghigna, S., Moore, B., Governato, F., et al. 2000, ApJ, 544, 616

González-García, A. C. & van Albada, T. S. 2003, MNRAS, 342, L36

Goodman, J. 1988, ApJ, 329, 612

Gorenflo, L. & Vessella, S. 1991, Abel Integral Equations (Berlin: Springer-Verlag, 1991; p.195)

Griest, K. 1988, Physical Review D, 38, 2357

Hao, J. G. & Akhoury, R. 2005, ArXiv Astrophysics e-prints

Heggie, D. & Hut, P. 2003, The Gravitational Million-Body Problem: A Multidisciplinary Approach to Star Cluster Dynamics (Cambridge University Press, 2003, 372 pp.)

Heggie, D. C. & Mathieu, R. D. 1986, Lecture Notes in Physics, Berlin Springer Verlag, 267, 233

Henon, M. 1959, Annales d'Astrophysique, 22, 126

Henon, M. 1973, A&A, 24, 229

Hernquist, L. 1987, ApJS, 64, 715

Hernquist, L. 1990, ApJ, 356, 359

Hernquist, L. & Ostriker, J. P. 1992, ApJ, 386, 375

Hjorth, J. & Madsen, J. 1995, ApJ, 445, 55

Hopkins, P., Bahcall, N., & Bode, P. 2005, ApJL, 618, 1

Hubble, E. 1926, Ap.J., 64, 321

Hut, P., Heggie, D., & Trenti, M. 2005, In preparation

Hut, P. & Makino, J. 2004, The Art of Computational Science (http://www.artcompsci.org/)

Jaffe, W. 1983, MNRAS, 202, 995

Jaffe, W. 1987, in IAU Symp. 127: Structure and Dynamics of Elliptical Galaxies, ed P.T. de Zeeuw, Reidel, Dordrecht, The Netherlands, 511–512

Jungman, G., Kamionkowski, M., Kosowsky, A., & Spergel, D. N. 1996, Physical Review D, 54, 1332

Kandrup, H. E. & Sideris, I. V. 2003, ApJ, 585, 244

Kandrup, H. E. & Sygnet, J. F. 1985, ApJ, 298, 27

Katz, J. 1978, MNRAS, 183, 765

Katz, J. 1979, MNRAS, 189, 817

Katz, J. 1980, MNRAS, 190, 497

Katz, N. 1991, ApJ, 368, 325

Kazantzidis, S., Mayer, L., Mastropietro, C., et al. 2004, ApJ, 608, 663

King, I. R. 1966, AJ, 71, 64

Klypin, A., Kravtsov, A. V., Valenzuela, O., & Prada, F. 1999, ApJ, 522, 82

Kolb, E. W. & Turner, M. S. 1990, The early universe (Frontiers in Physics, Reading, MA: Addison-Wesley, 1988, 1990)

Koopmans, L. V. E., Treu, T., Fassnacht, C. D., Blandford, R. D., & Surpi, G. 2003, ApJ, 599, 70

Kustaanheimo, P. & Stiefel, E. 1965, J. Reine Angew. Math., 218, 204

Lanzoni, B., Ciotti, L., Cappi, A., Tormen, G., & Zamorani, G. 2004, ApJ, 600, 640

Lemson, G. 1995, PhD thesis, Groningen University

Lombardi, M. & Bertin, G. 2001, A&A, 375, 1091

Londrillo, P., Messina, A., & Stiavelli, M. 1991, MNRAS, 250, 54

Londrillo, P., Nipoti, C., & Ciotti, L. 2003, Societa Astronomica Italiana Memorie Supplement, 1, 18

Lopez, R. E., Dodelson, S., Heckler, A., & Turner, M. S. 1999, Physical Review Letters, 82, 3952

Lynden-Bell, D. 1967, MNRAS, 131, 101

Lynden-Bell, D. & Eggleton, P. P. 1980, MNRAS, 191, 483

Lynden-Bell, D. & Wood, R. 1968, MNRAS, 138, 495

Ma, C. & Boylan-Kolchin, M. 2004, Physical Review Letters, 93, 021301

Magliocchetti, M., Pucacco, G., & Vesperini, E. 1998, MNRAS, 301, 25

Makino, J., Fukushige, T., Koga, M., & Namura, K. 2003, PASJ, 55, 1163

Mangeney, A., Califano, F., Cavazzoni, C., & Travnicek, C. 2002, J. Comp. Phys., 179, 495

May, A. & van Albada, T. S. 1984, MNRAS, 209, 15

McGlynn, T. A. 1984, ApJ, 281, 13

Merrall, T. E. C. & Henriksen, R. N. 2003, ApJ, 595, 43

Merritt, D. 1985, AJ, 90, 1027

Merritt, D. & Aguilar, L. A. 1985, MNRAS, 217, 787

Merritt, D., Tremaine, S., & Johnstone, D. 1989, MNRAS, 236, 829

Meza, A., Navarro, J. F., Steinmetz, M., & Eke, V. R. 2003, ApJ, 590, 619

Meza, A. & Zamorano, N. 1997, ApJ, 490, 136

Milgrom, M. 1983, ApJ, 270, 371

Milgrom, M. & Sanders, R. H. 2003, ApJL, 599, L25

Moore, B., Governato, F., Quinn, T., Stadel, J., & Lake, G. 1998, ApJL, 499, L5

Mould, J. R., Huchra, J. P., Freedman, W. L., et al. 2000, ApJ, 529, 786

Nakamura, T. K. 2000, ApJ, 531, 739

Navarro, J. F., Frenk, C. S., & White, S. D. M. 1996, Ap.J., 462, 563

Navarro, J. F., Frenk, C. S., & White, S. D. M. 1997, ApJ, 490, 493

Nipoti, C., Londrillo, P., & Ciotti, L. 2003, MNRAS, 342, 501

Osipkov, L. P. 1979, Soviet Astronomy Letters, 5, 42

Padmanabhan, T. 1989, ApJS, 71, 751

Palmer, P. 1993, Stability of collisionless stellar systems (Kluwer Academic Publishers)

Palmer, P. L. & Papaloizou, J. 1987, MNRAS, 224, 1043

Palmer, P. L. & Papaloizou, J. 1988, MNRAS, 231, 935

Palmer, P. L., Papaloizou, J., & Allen, A. J. 1990, MNRAS, 246, 415

Pellegrini, S. 1999, A&A, 351, 487

Percival, W. J., Baugh, C. M., Bland-Hawthorn, J., et al. 2001, MNRAS, 327, 1297

Plummer, H. C. 1915, MNRAS, 76, 107

Polyachenko, V. & Shukhman, I. 1981, Soviet Astron., 25, 533

Polyachenko, V. L. 1992, Soviet Astronomy, 36, 482

Press, W. H., Teukolsky, S., Vetterling, W., & Flannery, B. 1986, Numerical recipes (Cambridge University Press, 1986)

Romanowsky, A. J., Douglas, N. G., Arnaboldi, M., et al. 2003, Science, 301, 1696

Romeo, A. B., Horellou, C., & Bergh, J. 2004, MNRAS, 354, 1208

Roy, F. & Perez, J. 2004, MNRAS, 348, 62

Ruhl, J. E., Ade, P. A. R., Bock, J. J., et al. 2003, ApJ, 599, 786

Saglia, R. P., Bertin, G., & Stiavelli, M. 1992, ApJ, 384, 433

Saha, P. 1991, MNRAS, 248, 494

Saha, P. 1992, MNRAS, 254, 132

Sandage, A. & Bedke, J. 1994, The Carnegie atlas of galaxies (Washington, DC: Carnegie Institution of Washington with The Flintridge Foundation, —c1994)

Sanders, R. H. & McGaugh, S. S. 2002, ARAA, 40, 263

Schneider, D. P., Fan, X., Hall, P. B., et al. 2003, AJ, 126, 2579

Sellwood, J. A. 1981, A&A, 99, 362

Sersic, J. L. 1968, Atlas de galaxias australes (Cordoba, Argentina: Observatorio Astronomico, 1968)

Shu, F. H. 1978, ApJ, 225, 83

Shu, F. H. 1987, ApJ, 316, 502

Simon, J. D., Bolatto, A. D., Leroy, A., & Blitz, L. 2003, ApJ, 596, 957

Spergel, D. N., Verde, L., Peiris, H. V., et al. 2003, ApJS, 148, 175

Spitzer, L. 1987, Dynamical Evolution of Globular Clusters (Princeton: Princeton Univ. Press)

Spitzer, L. J. & Hart, M. H. 1971, ApJ, 164, 399

Stiavelli, M. & Bertin, G. 1987, MNRAS, 229, 61

Stiavelli, M., Fall, S. M., & Panagia, N. 2004, American Astronomical Society Meeting Abstracts, 205,

Stiavelli, M. & Sparke, L. S. 1991, ApJ, 382, 466

Succi, S. 2003, An Introduction to Computational Physics II (Scuola Normale Superiore, Pisa Italy, 2003, 107 pp.)

Sygnet, J. F., des Forets, G., Lachieze-Rey, M., & Pellat, R. 1984, ApJ, 276, 737

Taruya, A. & Sakagami, M. 2002, Physica A, 307, 185

Teuben, P. 1995, ASP Conf. Ser. 77, 398

Theis, C. 1998, A&A, 330, 1180

Tremaine, S. 1986, in Structure and Dynamics of Elliptical Galaxies, T. de Zeeuw, Dordrecht: Reidel, 367

Tremaine, S., Henon, M., & Lynden-Bell, D. 1986, MNRAS, 219, 285

Trenti, M. & Bertin, G. 2005, A&A, 429, 161

Trenti, M., Bertin, G., & van Albada, T. S. 2005, A&A, 433, 57

Treu, T., Ellis, R. S., Liao, T. X., & van Dokkum, P. G. 2005, ApJL, 622, L5

Treu, T., Stiavelli, M., Walker, A. R., et al. 1998, A&A, 340, L10

Tully, R. B. & Fisher, J. R. 1977, A&A, 54, 661

Udry, S. 1993, A&A, 268, 35

van Albada, T. 1982, MNRAS, 201, 939

van Albada, T. S. & van Gorkom, J. H. 1977, A&A, 54, 121

Vesperini, E. 1997, MNRAS, 287, 915

Villumsen, J. V. 1982, MNRAS, 199, 493

Voglis, N. 1994, MNRAS, 267, 379

Warren, M. S., Quinn, P. J., Salmon, J. K., & Zurek, W. H. 1992, ApJ, 399, 405

Weinberg, M. D. 1989, MNRAS, 239, 549

Weinberg, M. D. 1991, ApJ, 368, 66

Weinberg, M. D. 1994, ApJ, 421, 481

White, S. D. M., Navarro, J. F., Evrard, A. E., & Frenk, C. S. 1993, Nature, 366, 429

Williams, L., Austin, C., Barnes, E., Babul, A., & Dalcanton, J. 2005, Proceedings of Science; astro-ph/0412442